CERN-THESIS-2005-086

An Experimental Study on the Long-term Stability of Particle Motion in Hadron Storage Rings

Dissertation
zur Erlangung des Doktorgrades
des Fachbereichs Physik
der Universität Hamburg

vorgelegt von
Wolfram Fischer
aus Torgau

Hamburg
1995

Gutachter der Dissertation:	Prof. Dr. P. Schmüser Dr. F. Willeke
Gutachter der Disputation:	Prof. Dr. P. Schmüser Prof. Dr. Dr. h.c. G.-A. Voss
Datum der Disputation:	24.11.1995
Sprecher des Fachbereichs Physik und Vorsitzender des Promotionsausschusses:	Prof. Dr. B. Kramer

Kurzfassung

Die Kombination von nichtlinearen magnetischen Feldern und Q-Wert-Modulation kann zu chaotischer Teilchenbewegung führen und damit die dynamische Apertur von Hadronen-Speicherringen begrenzen. Dieser Effekt ist von besonderem Interesse für Hochenergie-Speicherringe mit supraleitenden Magneten bei Injektionsenergie, da hier magnetische Feldfehler und die Strahlgröße ihre größten Werte annehmen.

Ziel eines Experiments am CERN SPS war es, die relevanten Effekte für die Stabilität der Bewegung einzelner Teilchen zu finden. Experimentelle Ergebnisse werden mit numerischen Simulationen der Teilchendynamik über viele Umläufe verglichen, um zu testen, bis zu welcher Genauigkeit die dynamische Apertur unter gut bekannten Bedingungen vorausberechnet werden kann. Um das phenomänologische Verständnis der Teilchenbewegung im Phasenraum zu verbessern, wurden die Verlustmechanismen im Detail studiert.

In einem komplementären Experiment am HERA-Protonenring bei Injektionsenergie wurde die dynamische Apertur unter Bedingungen gemessen, die ähnlich denen im normalen Betrieb sind. Die numerischen Simulationen für diese Messungen wurden mit einem sehr detaillierten Modell der nichtlinearen magnetischen Felder ausgeführt, die für jeden Magneten gemessen worden sind.

Für das LHC werden Ergebnisse numerischer Simulationen präsentiert, die den Effekt verschiedener Q-Wert-Rippel auf die dynamische Apertur für zwei verschiedene Mengen von zufällig ausgewählten nichtlinearen Feldfehlern zeigen.

Abstract

Nonlinear magnetic fields in conjunction with tune modulation may lead to chaotic particle motion and thereby limit the dynamic aperture in hadron storage rings. This is of particular interest for high energy storage rings with superconducting magnets at injection energy where magnetic field errors and the beam size have their maximum values.

At the CERN SPS a dynamic aperture experiment was performed with the aim of finding the relevant effects for the stability of single particle motion in hadron storage rings. Experimental results are compared to long-term particle tracking to test to which extent computer programs can predict the dynamic aperture under well known conditions. In addition, detailed investigations of the loss mechanisms were pursued to improve the phenomenological understanding of the intricate details of particle motion in phase space.

In a complementary experiment at the HERA proton ring at injection energy the dynamic aperture was measured under normal operating conditions. The computer simulations for these measurements included a very detailed model of the nonlinear fields which were measured for each individual magnet.

Simulation results for the LHC are shown that estimate the effect of tune ripple of different strength on the dynamic aperture for different sets of random nonlinear field errors.

Contents

List of Commonly Used Symbols

A	normal form transformation, acceptance
$\vec{A}$	vector potential of the magnetic field
a	detuning coefficient
α	accelerator alpha function
$\vec{B}$	magnetic field
b	detuning coefficient
β	accelerator beta function, relativistic beta
c	detuning coefficient
E	energy
ϵ	emittance
η	momentum deviation $\Delta p/p$
f	frequency
H	Hamiltonian
I	action variable
i	imaginary unit $\sqrt{-1}$
k	kick strength
L	machine circumference
M	one turn map
N	normal form
p	momentum
Q	tune
R	average machine radius
s	path length
T	Taylor series representation of a one turn map
t	time
Θ, θ	azimuth
WP1	working point $(Q_x, Q_z) = (26.637, 26, 533)$, close to an 8^{th} order resonance
WP2	working point $(Q_x, Q_z) = (26.605, 26, 538)$, close to a 5^{th} order resonance
x	horizontal coordinate
x'	horizontal angle
y	either horizontal or vertical coordinate
y'	either horizontal or vertical angle
z	vertical coordinate
z'	vertical angle

Chapter 1

Introduction

1.1 Motivation

The bending and focusing fields for the highest energy machines can only be obtained with superconducting magnets. In these magnets the strong fields required do not allow to use pole faces of any material, instead the coil geometry has to produce the desired field type. Due to technical and economical limitations this can be achieved only approximately resulting in nonlinear fields errors [1] relevant up to an order as high as 10. Moreover, in superconducting magnets there are time dependent persistent currents [2] particularly important at low excitation, i.e. injection energy, leading to additional magnetic field distortions.

Another effect present in accelerators is tune modulation which arises for example from power supply ripple. The conjunction of both effects, nonlinear magnetic fields and tune ripple, can lead to particle losses and limit the dynamic aperture.

The search for Higgs and supersymmetric particles is one of the key goals of new accelerators like the Large Hadron Collider (LHC), the 7 TeV on 7 TeV proton-proton collider planned in the LEP tunnel at CERN. If a Higgs exists in the accessible mass range its identification and separation from the formidable hadronic background will be based on easily identifiable decays that are very rare. Hence, a high luminosity is needed and this requires a sufficient dynamic aperture from injection up to top energy. The prediction of the dynamic aperture is therefore a demanding task in the process of designing such machines since it is too expensive to include large safety margins.

Dedicated experiments at existing hadron strorage rings have been performed to test the ability of existing element-by-element tracking programs like SIXTRACK [3] to successfully predict the dynamic aperture. As a first step experiments at the CERN Super Proton Synchrotron (SPS) were done using additional strong nonlinearities and tune modulation and in a second experiment at the DESY HERA proton ring a superconducting machine was tested under normal operating conditions.

A better phenomenological and theoretical description of the loss mechanisms in hadron storage rings is also desirable. Both, experiments and simulations, can be used to test existing theoretical concepts and to improve the understanding of nonlinear dynamics in accelerators.

1.2 Outline

Chapter 2 is a short introduction into the theory of nonlinear Hamiltonian systems. Starting from the general Hamiltonian for particle motion in hadron storage rings the four dimensional case is treated and a perturbative method is presented. The influence of sextupoles on the detuning and the creation of resonances is discussed and the effect of harmonic tune modulation is shown for a single isolated resonance. Map methods are mentioned and the concept of dynamic aperture is discussed.

Chapter 3 is devoted to the simulation of particle motion in accelerators. After reviewing the modeling of elements in the tracking code SIXTRACK the approximations made in this process are evaluated. A tracking strategy is presented and the methods for the postprocessing of tracking data are shown that will be used in the following chapters. The last section deals with the computing times needed for tracking studies.

Chapter 4 presents the SPS dynamic aperture experiment. After a short review of the history of this experiment the instrumentation and experimental conditions are described in detail. Experimental results and computer simulations are shown for both the scraper and the wire scanner experiment. In particular, the measured and computed dynamic apertures are compared for various conditions and a phenomenological description of the observed loss mechanisms is given.

In Chapter 5 results of the dynamic aperture experiment at the HERA proton ring at injection energy are presented. Experimental conditions are given in detail and the measured and computed dynamic apertures are compared. In this case the tracking model was particularly complex.

Chapter 6 gives an outlook on the effect of tune ripple on the stability of particle motion in the LHC. Different modulation depth and multipole error sets are tested.

Finally, the results are summarized in a separate chapter.

Appendix A gives some formulae for kicked particle distributions in hadron storage rings that have been used for the calibration of the SPS instrumentation. In Appendix B all experimental cases of the SPS dynamic aperture experiment from November 1993 until December 1994 are listed.

Chapter 2

Nonlinear Hamiltonian Systems

The single particle motion in hadron accelerators can be treated in the Hamiltonian formalism since synchrotron radiation has a negligible impact on the particle dynamics even for high energy machines like the LHC. Besides guiding and focusing fields nonlinearities are present in these machines either for correction purposes or due to unavoidable field errors.

Another effect that can not be avoided in accelerators is tune ripple which comes for instance from power supplies. Nonlinearities in conjunction with tune ripple may lead to chaotic motion and thereby limit the dynamic aperture. This has been the motivation for various studies of either theoretical [4–9] or experimental nature (see references [10, 11] for an overview).

The starting point in this chapter is the general six-dimensional Hamiltonian for single particle motion in accelerators. The magnetic field expansion and its connection to the vector potential is given. The Hamiltonian is simplified to four dimensions and transformed to action-angle variables. After reviewing perturbation theory the case of sextupole-induced nonlinearities is treated. The Hamiltonian in the single-resonance approximation is studied briefly with and without tune modulation. Maps and normal forms are mentioned and finally the concept of dynamic aperture is discussed. Emphasis is put on formulae for the four-dimensional case which will be applied to the experimental and simulation results in the following chapters.

2.1 The General Hamiltonian

The particle motion in accelerators can be conveniently described in a ortho-normal coordinate system (x, z, s) relative to a design orbit. Here, the coordinate s is the path length on the design orbit, x the "horizontal" and z the "vertical" coordinate[1]. In the following y is used when the expression applies to both x and z. One can introduce new small and

[1] The definition of "horizontal" and "vertical" is somewhat arbitrary since the dynamics is governed by a local Hamiltonian and it may be appropriate, for instance in a tilted magnet, to choose coordinates that are different from the global "horizontal" and "vertical" ones [12, 13].

oscillating coordinates in the longitudinal direction

$$\sigma = s - v_0 t \tag{2.1}$$

and

$$p_\sigma = \frac{1}{\beta_0} \cdot \frac{\Delta E}{E_0}, \tag{2.2}$$

where v_0 and E_0 are the velocity and energy of on-momentum particles respectively and $\beta_0 = v_0/c$ the relativistic beta function for these particles. Then the Hamiltonian in SI units can be written as [14]

$$\begin{aligned} H(x,z,\sigma,p_x,p_z,p_\sigma;s) = p_\sigma - (1+\eta)\cdot[1 + K_x(s)\cdot x + K_z(s)\cdot z] \times \\ \times \left\{ 1 - \frac{\left(p_x - \frac{e}{p_0}A_x(s)\right)^2 + \left(p_z - \frac{e}{p_0}A_z(s)\right)^2}{(1+\eta)^2} \right\}^{1/2} - \\ - [1 + K_x(s)\cdot x + K_z(s)\cdot z]\cdot \frac{e}{p_0} A_s(s), \end{aligned} \tag{2.3}$$

$\eta = \Delta p/p$ being the momentum deviation and $\vec{A} = (A_x, A_z, A_s)$ the vector potential. It has been assumed that the closed design orbit is either bent in the $x-s$ plane (with bending radius $1/K_x$) or in the $z-s$ plane (with bending radius $1/K_z$) thus excluding torsion and it follows that $K_x \cdot K_z = 0$. The equations of motions read

$$x' = \frac{\partial H}{\partial p_x}, \quad p_x' = -\frac{\partial H}{\partial x}, \tag{2.4}$$

$$z' = \frac{\partial H}{\partial p_z}, \quad p_z' = -\frac{\partial H}{\partial z}, \tag{2.5}$$

$$\sigma' = \frac{\partial H}{\partial p_\sigma}, \quad p_\sigma' = -\frac{\partial H}{\partial \sigma}, \tag{2.6}$$

where the prime denotes the derivative with respect to s. With $\vec{v} = (x, z, \sigma, p_x, p_z, p_\sigma)$ equations (2.4-2.6) can be also expressed as

$$\frac{\mathrm{d}}{\mathrm{d}s}\vec{v} = \underline{S}\,\frac{\partial H}{\partial \vec{v}} \tag{2.7}$$

where $\underline{S}$ is the symplectic form

$$\underline{S} = \begin{pmatrix} \underline{0}_3 & \underline{E}_3 \\ -\underline{E}_3 & \underline{0}_3 \end{pmatrix}, \; \underline{0}_3 = \begin{pmatrix} 0 & 0 & 0 \\ 0 & 0 & 0 \\ 0 & 0 & 0 \end{pmatrix}, \; \underline{E}_3 = \begin{pmatrix} 1 & 0 & 0 \\ 0 & 1 & 0 \\ 0 & 0 & 1 \end{pmatrix}. \tag{2.8}$$

The structure of the equations of motion (2.7) is equivalent to the condition that the Jacobian

$$\underline{J}(s, s_0) = \frac{\partial \vec{v}(s)}{\partial \vec{v}(s_0)} \tag{2.9}$$

is symplectic:

$$\underline{J}^T \underline{S} \underline{J} = \underline{S}. \tag{2.10}$$

With

$$\det(\underline{J}^T \underline{S} \underline{J}) = \det(\underline{J}^T) \det(\underline{S}) \det(\underline{J}) = \det(\underline{J})^2 \det(\underline{S}) = \det(\underline{S}) \tag{2.11}$$

it follows that $\det(\underline{J}) = \pm 1$. Through $\det(\underline{J}(s_0, s_0)) = 1$ the determinant $\det(\underline{J})$ is restricted to $+1$ and the phase space volume

$$\int \prod_{n=1}^{6} \mathrm{d}v_n(s) = \int \prod_{n=1}^{6} \mathrm{d}v_n(s_0) \det(\underline{J}(s, s_0)) = \int \prod_{n=1}^{6} \mathrm{d}v_n(s_0), \tag{2.12}$$

is constant (Liouville's theorem).

2.2 Vector Potential and Magnetic Field Expansion

In the chosen curvilinear coordinate system the magnetic field $\vec{B} = \nabla \times \vec{A}$ can be computed from the vector potential $\vec{A}$ as [14]

$$B_x = \frac{1}{(1 + K_x \cdot x + K_z \cdot z)} \cdot \left\{ \frac{\partial}{\partial z} \left[(1 + K_x \cdot x + K_z \cdot z) A_s \right] - \frac{\partial}{\partial s} A_z \right\}, \tag{2.13}$$

$$B_z = \frac{1}{(1 + K_x \cdot x + K_z \cdot z)} \cdot \left\{ \frac{\partial}{\partial s} A_x - \frac{\partial}{\partial x} \left[(1 + K_x \cdot x + K_z \cdot z) A_s \right] \right\}, \tag{2.14}$$

$$B_s = \frac{\partial}{\partial x} A_z - \frac{\partial}{\partial z} A_x. \tag{2.15}$$

If there are only transverse magnetic field components, e.g. no solenoid fields, one has $A_x = A_z = 0$ and the vector potential component A_s can be expanded in a power series as

$$-\frac{e}{p_0} A_s(s) = \frac{1}{2} [1 + K_x(s) \cdot x + K_z(s) \cdot z] + \sum_{\substack{mn \\ m,n \geq 1 \\ m+n \geq 2}}^{\infty} \mathfrak{a}_{mn}(s) x^m z^n \tag{2.16}$$

where the contribution of the dipole fields has been separated from the rest. From the Maxwell equation $\nabla \vec{B} = 0$ it follows that

$$(m+1)(m+2)\mathfrak{a}_{m+2,n} + (n+1)(n+2)\mathfrak{a}_{n,m+2} = 0. \tag{2.17}$$

The magnetic field $\vec{B}$ can be expanded in Cartesian coordinates (x, z) as [15]

$$(B_z + iB_x) = B_{main} \sum_{n=1}^{\infty} \frac{1}{r_0^{n-1}} (b_n - ia_n)(x + iz)^{n-1}, \tag{2.18}$$

which is equivalent to an expansion in polar coordinates (r, Θ)

$$B_\Theta(r, \Theta) = B_{main} \sum_{n=1}^{\infty} \left(\frac{r}{r_0}\right)^{n-1} (b_n \cos n\Theta + a_n \sin n\Theta), \tag{2.19}$$

$$B_r(r, \Theta) = B_{main} \sum_{n=1}^{\infty} \left(\frac{r}{r_0}\right)^{n-1} (-a_n \cos n\Theta + b_n \sin n\Theta), \tag{2.20}$$

where the $r-\Theta$ plane coincides with the $x-z$ plane and $B_{main} = K_x \frac{P_0}{e}$ is the magnitude of the main dipole field. The b_n are called "normal" and the a_n "skew" multipole coefficients respectively. The subscript "1" denotes a dipole, "2" a quadrupole etc. r_0 is a reference radius at which the coefficients b_n, a_n are determined in measurements. The coefficients $\mathfrak{a}_{mn}$ are now given as [16]

$$\mathfrak{a}_{mn} = (-1)^{n/2} \frac{(m+n-1)!}{m!n!} b_{m+n} r_0^{-(m+n)}, \text{ for } n \text{ even ("normal" multipoles),} \tag{2.21}$$

$$\mathfrak{a}_{mn} = (-1)^{(n+1)/2} \frac{(m+n-1)!}{m!n!} a_{m+n} r_0^{-(m+n)}, \text{ for } n \text{ odd ("skew" multipoles).} \tag{2.22}$$

2.3 The Hamiltonian in Four Dimensions

Some simplifications make the Hamiltonian (2.3) more tractable for an analysis:

1. Only transverse motion is considered. $\Rightarrow H$ is independent of σ and p_σ.
2. Only on-momentum particles are considered. $\Rightarrow \eta = 0$.
3. Only transverse magnetic fields are considered (e.g. no solenoids). $\Rightarrow A_x = A_z = 0$.
4. In the second term in (2.3) the square root is expanded and only terms up to second order in (x, z, p_x, p_z) are kept.

$$\Rightarrow \sqrt{1 - p_x^2 - p_z^2} \approx 1 - \frac{1}{2}p_x^2 - \frac{1}{2}p_z^2$$

5. The curvatures K_x, K_z are assumed to be small and the cross-terms of these quantities with higher order coefficients $\mathfrak{a}_{mn}$ are disregarded.

In this case the relations

$$p_x = \frac{\mathrm{d}}{\mathrm{d}s}x \equiv x', \quad p_z = \frac{\mathrm{d}}{\mathrm{d}s}z \equiv z', \tag{2.23}$$

hold [14] and the Hamiltonian (2.3) becomes

$$H(x,z,x',z';s) = \frac{1}{2}x'^2 + \frac{1}{2}z'^2 + k_x(s)x^2 - k_z(s)z^2 + \sum_{\substack{mn \\ m,n\geq 1 \\ m+n\geq 2}}^{\infty} \mathfrak{a}_{mn}(s)x^m z^n \tag{2.24}$$

with $k_x = K_x^2 + \mathfrak{a}_{20}$ and $k_z = -(K_z^2 + \mathfrak{a}_{02})$. The k_y are a measure for the focusing strength. The coefficient $\mathfrak{a}_{11}$ in the last sum in (2.24) leads to linear coupling and the other coefficients to nonlinearities.

2.4 Linear Solution

The equations of motion for the linear uncoupled part of the Hamiltonian (2.24)

$$H_0(x,z,x',z';s) = \frac{1}{2}x'^2 + \frac{1}{2}z'^2 + k_x(s)x^2 - k_z(s)z^2 \tag{2.25}$$

have the solution [17,18]

$$\begin{aligned} y &= \sqrt{2I_y\beta_y}\cdot\cos(\phi_y(s)+\phi_{y0}), \\ y' &= -\sqrt{\frac{2I_y}{\beta_y(s)}}\Big(\alpha_y(s)\cos(\phi_y(s)+\phi_{y0}) + \sin(\phi_y(s)+\phi_{y0})\Big) \end{aligned} \tag{2.26}$$

where the I_y and ϕ_{y0} are the constants of motion and $\alpha_y(s) = -\beta_y'(s)/2$. The functions $\beta_y(s)$ are periodic with the machine length L and satisfy the nonlinear ordinary differential equation

$$\frac{1}{2}\beta_y(s)\beta_y''(s) - \frac{1}{4}\beta_y'(s)^2 + k_y(s)\beta_y(s)^2 = 1 \tag{2.27}$$

involving the focusing strength k_y. The phase functions $\phi_y(s)$ can also be derived from $\beta_y(s)$ as

$$\phi_y(s) = \int_{s_0}^{s} \frac{\mathrm{d}t}{\beta_y(t)} \tag{2.28}$$

and the quantities

$$Q_{y0} = \frac{1}{2\pi}\phi_y(s_0+L) \tag{2.29}$$

are called the linear tunes. Instead of the actions, often the Courant-Snyder invariants

$$\epsilon_y = 2\ I_y = \frac{1}{\beta_y}\left(y^2 + (\alpha_y y + \beta_y y')^2\right), \tag{2.30}$$

are used.

2.5 The Hamiltonian in Action-Angle Variables

By means of the mixed variable generating function [9]

$$F_1(x,z,\phi_x,\phi_z;s)=\frac{x^2}{2\beta_x}\left(\tan(\phi_x+\phi_{x0})+\alpha_x\right)+\frac{z^2}{2\beta_z}\left(\tan(\phi_z+\phi_{z0})+\alpha_z\right), \tag{2.31}$$

the Hamiltonian (2.24) can be expressed in terms of the constants of motion for the linear case. With a change of the independent variable from s to the azimuth $\theta=2\pi s/L$ one has

$$\begin{aligned} H(I_x,I_z,\phi_x,\phi_z;\theta) &= Q_{x0}I_x+Q_{z0}I_z+ \\ &+R\sum_{mnkl}\binom{m}{\frac{m-k}{2}}\binom{n}{\frac{n-l}{2}}\mathfrak{a}_{mn}(\theta)\left(\frac{\beta_x}{2}\right)^{\frac{m}{2}}\left(\frac{\beta_z}{2}\right)^{\frac{n}{2}}\times \\ &\times I_x^{\frac{m}{2}}I_z^{\frac{n}{2}}\exp\Big\{i\left(k(\phi_x+\phi_{x0})+l(\phi_z+\phi_{z0})\right)\Big\} \end{aligned} \tag{2.32}$$

with

$$k=-m,-m+2,...,m-2,m \quad \text{and} \quad l=-n,-n+2,...,n-2,n, \tag{2.33}$$

$R=L/2\pi$ is the average machine radius. Separating the phase advance into an average and a fluctuating part by

$$\phi_y(\theta)=\tilde{\phi}_y(\theta)+\theta Q_{y0} \tag{2.34}$$

one can now define the following functions

$$h_{mnkl}(\theta)=R\binom{m}{\frac{m-k}{2}}\binom{n}{\frac{n-l}{2}}\mathfrak{a}_{mn}(\theta)\left(\frac{\beta_x}{2}\right)^{\frac{m}{2}}\left(\frac{\beta_z}{2}\right)^{\frac{n}{2}}\exp\left\{i\left(k\tilde{\phi}_x(\theta)+l\tilde{\phi}_z(\theta)\right)\right\}. \tag{2.35}$$

Since these functions are periodic in θ, they can be decomposed in a Fourier series as

$$h_{mnkl}(\theta)=\sum_{p=-\infty}^{+\infty}h^p_{mnkl}\mathrm{e}^{-ip\theta} \tag{2.36}$$

with

$$h^p_{mnkl}=\frac{1}{2\pi}\int_0^{2\pi}h_{mnkl}(\theta)\mathrm{e}^{ip\theta}\mathrm{d}\theta. \tag{2.37}$$

Now Eq. (2.32) becomes

$$\begin{aligned} H(I_x,I_z,\phi_x,\phi_z;\theta) &= Q_{x0}I_x+Q_{z0}I_z+ \\ &+\sum_{mnklp}h^p_{mnkl}(\theta)I_x^{\frac{m}{2}}I_z^{\frac{n}{2}}\mathrm{e}^{i(k\phi_{x0}+l\phi_{z0}+(kQ_{x0}+lQ_{z0}-p)\theta)}. \end{aligned} \tag{2.38}$$

2.6 Canonical Perturbation Theory

For nearly integrable systems, i.e.

$$H(I_x, I_z, \phi_x, \phi_z; \theta) = H_0(I_x, I_z) + H_1(I_x, I_z, \phi_{x0}, \phi_z; \theta) \tag{2.39}$$

where H_1 is small, one can look for integrable solutions by expanding in the small parameter H_1. For the Hamiltonian (2.38) one has accordingly

$$H_0(I_x, I_z) = Q_{x0} I_x + Q_{z0} I_z \tag{2.40}$$

and

$$H_1(I_x, I_z, \phi_x, \phi_z; \theta) = \sum_{mnklp} h^p_{mnkl}(\theta) I_x^{\frac{m}{2}} I_z^{\frac{n}{2}} \mathrm{e}^{i(k\phi_{x0} + l\phi_{z0} + (kQ_{x0} + lQ_{z0} - p)\theta)}, \tag{2.41}$$

and one aims at changing to new coordinates $(\bar{I}_x, \bar{I}_z, \bar{\phi}_x, \bar{\phi}_z)$ for which the perturbation $\bar{H}_1$ in the new Hamiltonian

$$\bar{H}(\bar{I}_x, \bar{I}_z, \bar{\phi}_x, \bar{\phi}_z; \theta) = \bar{H}_0(\bar{I}_x, \bar{I}_z) + \bar{H}_1(\bar{I}_x, \bar{I}_z, \bar{\phi}_x, \bar{\phi}_z; \theta) \tag{2.42}$$

is of the order H_1^2. Through further transformations the perturbation in the new coordinates can be pushed to higher orders.

In (2.38) and in the transformed Hamiltonians three different types of terms can be identified:

1. Terms that are only dependent on the actions (I_x, I_z). These are $H_0(I_x, I_z)$ but also terms in $H_1(I_x, I_z, \phi_x, \phi_z; \theta)$ with $k = l = p = 0$. This part of the Hamiltonian determines the action-dependent tune.

2. Phase-dependent terms that vary slowly with θ, i.e. $k\phi_x + l\phi_z - p\theta \approx 0$. These terms are related to resonances. Perturbation theory breaks down at resonances because small denominators occur. Therefore, if present, these terms must be treated separately.

3. Phase dependent terms that vary rapidly with θ. Neglecting these terms is equivalent to restrict perturbation theory to first order [19].

A possible way to proceed with perturbation theory is as follows [16, 19]. With a mixed-variable generating function

$$F_2(\bar{I}_x, \bar{I}_z, \phi_x, \phi_z; \theta) = \bar{I}_x \phi_x + \bar{I}_z \phi_z + \mathfrak{F}(\bar{I}_x, \bar{I}_z, \phi_x, \phi_z; \theta) \tag{2.43}$$

the canonical transformation reads

$$I_y = \bar{I}_y + \frac{\partial \mathfrak{F}}{\partial \phi_y}, \ \bar{\phi}_y = \phi_y + \frac{\partial \mathfrak{F}}{\partial \bar{I}_y}, \ \bar{H} = H + \frac{\partial \mathfrak{F}}{\partial \theta}. \tag{2.44}$$

(2.43) is chosen because the perturbation is assumed to be small and the transformation should be close to the identity transformation. Furthermore one can choose for $\mathfrak{F}$ and the new perturbation $\bar{H}_1$ a form similar to the one of H_1:

$$\mathfrak{F}(\bar{I}_x,\bar{I}_z,\phi_x,\phi_z;\theta)=\sum_{mnklp}\mathfrak{f}^p_{mnkl}(\theta)\bar{I}_x^{\frac{m}{2}}\bar{I}_z^{\frac{n}{2}}\mathrm{e}^{i(k\phi_{x0}+l\phi_{z0}+(kQ_{x0}+lQ_{z0}-p)\theta)} \tag{2.45}$$

and

$$\bar{H}_1(\bar{I}_x,\bar{I}_z,\phi_x,\phi_z;\theta)=\sum_{mnklp}\bar{h}^p_{mnkl}(\theta)\bar{I}_x^{\frac{m}{2}}\bar{I}_z^{\frac{n}{2}}\mathrm{e}^{i(k\phi_{x0}+l\phi_{z0}+(kQ_{x0}+lQ_{z0}-p)\theta)}. \tag{2.46}$$

Substitution in (2.42) and (2.44) gives

$$\begin{aligned}\mathfrak{f}^p_{mnkl}=&\frac{\bar{h}^p_{mnkl}-h^p_{mnkl}}{i(kQ_{x0}+lQ_{z0}-p)}+\\&+i\sum_{\substack{m'n'k'l'p'\\m''n''k''l''}}\left[\frac{\frac{n'k''}{2}\left(\bar{h}^{p-p'}_{m''n''k''l''}\mathfrak{f}^{p'}_{m'n'k'l'}-h^{p-p'}_{m'n'k'l'}\mathfrak{f}^{p'}_{m''n''k''l''}\right)}{i(kQ_{x0}+lQ_{z0})}\right]+\\&+i\sum_{\substack{m'n'k'l'p'\\m''n''k''l''}}\left[\frac{\frac{m'l''}{2}\left(\bar{h}^{p-p'}_{m''n''k''l''}\mathfrak{f}^{p'}_{m'n'k'l'}-h^{p-p'}_{m'n'k'l'}\mathfrak{f}^{p'}_{m''n''k''l''}\right)}{i(kQ_{x0}+lQ_{z0})}\right]+\\&+\ldots\end{aligned} \tag{2.47}$$

In the first sum (expansion of I_x,ϕ_x)

$$\begin{aligned}m&=m'+m''-2,\\n&=n'+n'',\\k&=k'+k'',\\l&=l'+l'',\end{aligned} \tag{2.48}$$

holds and in the second sum (expansion of I_z,ϕ_z)

$$\begin{aligned}m&=m'+m'',\\n&=n'+n''-2,\\k&=k'+k'',\\l&=l'+l''.\end{aligned} \tag{2.49}$$

Eq. (2.47) can be solved for $\mathfrak{f}^p_{mnkl}$ and $\bar{h}^p_{mnkl}$ by iteration[2] starting with

$$\mathfrak{f}^{p(0)}_{mnkl}=0. \tag{2.50}$$

[2] The convergence of the iteration can be considerably improved by taking the amplitude dependece of the tune in the denominators in Eq. (2.47) into account as it is done in Ref. [20].

Explicit results up to third order are given in [16].

As mentioned above perturbation theory breaks down at resonances. From (2.47) this is obvious since small denominators lead to divergences.

2.7 Nonlinearities Introduced by Sextupoles

Sextupoles are the main source of nonlinearities in the SPS dynamic aperture experiment as well as in the HERA proton ring at injection energy. Amplitude-dependent tunes, nonlinear coupling and resonance driving are introduced by sextupoles. In this case $b_3 \neq 0$ for certain θ and (2.38) becomes

$$\begin{aligned} H(I_x, I_z, \phi_x, \phi_z; \theta) = Q_{x0} I_x + Q_{z0} I_x + \\ + \sum_{\substack{p=-\infty \\ k=-3,-1,1,3}}^{+\infty} h^p_{30k0}(\theta) I_x^{\frac{3}{2}} \mathrm{e}^{i(k\phi_{x0} + (kQ_{x0} - p)\theta)} + \\ + \sum_{\substack{p=-\infty \\ k=-1,1 \\ l=-2,0,2}}^{+\infty} h^p_{12kl}(\theta) I_x^{\frac{1}{2}} I_z^{\frac{2}{2}} \mathrm{e}^{i(k\phi_{x0} + l\phi_{z0} + (kQ_{x0} + lQ_{z0} - p)\theta)}. \end{aligned} \tag{2.51}$$

Second order perturbation theory and the omission of the phase dependent-terms leads to a Hamiltonian of the form

$$H(\bar{I}_x, \bar{I}_z) = Q_{x0} \bar{I}_x + Q_{z0} \bar{I}_z + a \bar{I}_x^2 + 2b \bar{I}_x \bar{I}_z + c \bar{I}_z^2 \tag{2.52}$$

where a, b and c are the so-called detuning coefficients. The new actions $\bar{I}_y$ can be related to the old ones by

$$\bar{I}_{x,z} = \frac{1}{2\pi} \int_0^{2\pi} \mathrm{d}\phi_{x,z} \; I_{x,z}(\phi_{x,z}, \phi_{z,x} = const). \tag{2.53}$$

2.7.1 Detuning

In first order perturbation theory (considering only b_3) there is no tune change with action. This reflects the fact that there are no terms with $k = l = p = 0$ in (2.51). In second order perturbation theory such terms appear and lead to detuning which looks like that due to octupoles in first order. In Ref. [21] the amplitude-dependent tunes were computed using

a Lie algebraic method. The horizontal and vertical tune shifts were found to be

$$\begin{aligned}\Delta Q_x(I_x, I_z) &= 2a \cdot I_x + 2b \cdot I_z \\ &= \frac{1}{16\pi} \int_0^{2\pi} \mathrm{d}\theta \int_0^{2\pi} \mathrm{d}\theta' \, \frac{b_3(\theta) b_3(\theta')}{r_0^4} \times \\ &\quad \times \Big[\left(-3\beta_x^{3/2}(\theta)\beta_x^{3/2}(\theta') I_x + 4\beta_x^{1/2}(\theta)\beta_x^{3/2}(\theta')\beta_z(\theta) I_z\right) T^{1,0}(\theta,\theta') - \\ &\quad - \beta_x^{3/2}(\theta)\beta_x^{3/2}(\theta') I_x T^{3,0}(\theta,\theta') + \\ &\quad + 2\beta_x^{1/2}(\theta)\beta_x^{1/2}(\theta')\beta_z(\theta)\beta_z(\theta') \left(T^{1,-2}(\theta,\theta') - T^{1,2}(\theta,\theta')\right) \Big]\end{aligned} \tag{2.54}$$

and

$$\begin{aligned}\Delta Q_z(I_x, I_z) &= 2b \cdot I_x + 2c \cdot I_z \\ &= \frac{1}{16\pi} \int_0^{2\pi} \mathrm{d}\theta \int_0^{2\pi} \mathrm{d}\theta' \, \frac{b_3(\theta) b_3(\theta')}{r_0^4} \times \\ &\quad \times \Big[4\left(\beta_x^{1/2}(\theta)\beta_x^{3/2}(\theta')\beta_z(\theta) I_x - \beta_x^{1/2}(\theta)\beta_x^{1/2}(\theta')\beta_z(\theta)\beta_z(\theta') I_z\right) T^{1,0}(\theta,\theta') - \\ &\quad - \beta_x^{1/2}(\theta)\beta_x^{1/2}(\theta')\beta_z(\theta)\beta_z(\theta') \left(2I_x + I_z\right) T^{1,2}(\theta,\theta') - \\ &\quad - \beta_x^{1/2}(\theta)\beta_x^{1/2}(\theta')\beta_z(\theta)\beta_z(\theta') \left(2I_x - I_z\right) T^{1,-2}(\theta,\theta') \Big]\end{aligned} \tag{2.55}$$

with

$$T^{kl}(\theta,\theta') = \frac{\cos\left(k\phi_x^+(\theta,\theta') + l\phi_z^+(\theta,\theta') - \pi(Q_{x0} + Q_{z0})\right)}{\sin\left(\pi(kQ_{x0} + lQ_{z0})\right)} \tag{2.56}$$

and

$$\phi_y^+(\theta,\theta') = \begin{cases} \phi_y(\theta) - \phi_y(\theta') & \text{if } \theta \geq \theta', \\ \phi_y(\theta') - \phi_y(\theta) & \text{if } \theta < \theta'. \end{cases} \tag{2.57}$$

For equations (2.54-2.57) only the linear machine functions and the sextupole configuration must be known. In second order perturbation theory the tune change is linear with the actions, quadratic with the sextupole strength and cubic with the beta functions.

2.7.2 Resonances

The first sum in (2.51) shows that the resonances $3Q_x = p$ and $Q_x = p$ can be driven by sextupoles. The latter is called a subresonance and can be excited already by a dipole, i.e. an element of lower order. The second sum in (2.51) may drive the resonances $Q_x \pm 2Q_z = p$ and $Q_x = p$.

However, formulae (2.48) and (2.49) indicate that for second order perturbation theory also resonances of order 2,4 and 6 can be driven. In higher order perturbation theory all resonances can be excited, except those that are forbidden by symmetry, e.g. $3Q_z = p$.

2.8 Single Resonance Hamiltonian

Since perturbation theory breaks down at resonances they need to be studied separately [8,22]. Close to a resonance

$$kQ_x + lQ_z \approx p \tag{2.58}$$

the Hamiltonian in action-angle variables can be approximated as follows. In the sum of (2.38) only the term for which (2.58) holds is retained and the phases in the exponential function of (2.35) are added to those in the kept term leading to

$$H(I_x, I_z, \phi_x, \phi_z, \theta) = I_x Q_{x,0} + I_z Q_{z,0} + g(I_x, I_z) + h(I_x, I_z)\cos(k\phi_x + l\phi_z - p\theta). \tag{2.59}$$

Here the functions $g(I_x, I_z)$ and $h(I_x, I_z)$ are the detuning and the driving term respectively. In the case of a weak resonance one has $g \gg h$ so that the amplitude-dependent tunes are

$$Q_y(I_x, I_z) = Q_{y0} + \frac{\partial g}{\partial I_y}(I_x, I_z). \tag{2.60}$$

Given the right sign of the detuning, the resonance condition

$$kQ_x(I_{xr}, I_{zr}) + lQ_z(I_{xr}, I_{zr}) = p \tag{2.61}$$

is satisfied for a set of actions (I_{xr}, I_{zr}).

As a first step new coordinates are introduced by a canonical transformation leading to a pseudo one-dimensional system. Using the generating function

$$F_2(\bar{I}_x, \bar{I}_z, \phi_x, \phi_z; \theta) = (k\phi_x + l\phi_z - p\theta)\bar{I}_x + \phi_z \bar{I}_z \tag{2.62}$$

the old and new coordinates are related via

$$I_x = k\bar{I}_x,\ \ I_z = l\bar{I}_x + \bar{I}_z,\ \ \bar{\phi}_x = k\phi_x + l\phi_z - p\theta,\ \ \bar{\phi}_z = \phi_z, \tag{2.63}$$

and the transformed Hamiltonian becomes

$$\bar{H}(\bar{I}_x, \bar{I}_z, \bar{\phi}_x) = (kQ_{x0} + lQ_{z0} - p)\bar{I}_x + \bar{g}(\bar{I}_x, \bar{I}_z) + \bar{h}(\bar{I}_x, \bar{I}_z)\cos(\bar{\phi}_x). \tag{2.64}$$

The new action $\bar{I}_z$ is an invariant of motion and therefore the motion in the $\bar{I}_z - \bar{\phi}_z$ plane can be disregarded.

As a second step the remaining action is expanded around the resonance value:

$$\hat{I}_x = \bar{I}_x - \bar{I}_{xr},\ \ \hat{\phi}_x = \bar{\phi}_x, \tag{2.65}$$

and taking into account a further approximation one arrives at

$$\hat{H}(\hat{I}_x, \hat{\phi}_x) = \frac{1}{2}\frac{\partial^2 \bar{g}}{\partial \bar{I}_x^2}(\bar{I}_{xr}, \bar{I}_{zr})\hat{I}_x^2 + \bar{h}(\bar{I}_{xr}, \bar{I}_{zr})\cos\hat{\phi}_x. \tag{2.66}$$

The Hamiltonian (2.66) describes a nonlinear pendulum (see for example [23]) with the total separatrix width given by

$$\Delta\hat{I}_{x,tot} = 2\hat{I}_{x,max} = 4\sqrt{\left|\frac{\bar{h}(\bar{I}_{xr},\bar{I}_{zr})}{\frac{\partial^2\bar{g}}{\partial\bar{I}_x^2}(\bar{I}_{xr},\bar{I}_{zr})}\right|}. \tag{2.67}$$

The island tune, with which particles with small deviations from the resonant values oscillate around a stable fix point, is [24]

$$Q_{I,x} = \frac{f_I}{f_{rev}} = \sqrt{\left|\bar{h}(\bar{I}_{xr},\bar{I}_{zr})\frac{\partial^2\bar{g}}{\partial\bar{I}_x^2}(\bar{I}_{xr},\bar{I}_{zr})\right|}. \tag{2.68}$$

Transforming back to the original actions I_x, I_z one has for the island widths

$$\Delta I_{x,tot} = k\Delta\hat{I}_{x,tot} = 4k\sqrt{\left|\frac{h(I_{xr},I_{zr})}{k^2\frac{\partial^2 g}{\partial I_x^2} + 2kl\frac{\partial^2 g}{\partial I_x\partial I_z} + l^2\frac{\partial^2 g}{\partial I_z^2}}\right|} \tag{2.69}$$

and

$$\Delta I_{z,tot} = l\Delta\hat{I}_{x,tot} = 4l\sqrt{\left|\frac{h(I_{xr},I_{zr})}{k^2\frac{\partial^2 g}{\partial I_x^2} + 2kl\frac{\partial^2 g}{\partial I_x\partial I_z} + l^2\frac{\partial^2 g}{\partial I_z^2}}\right|}. \tag{2.70}$$

and for the island tune

$$Q_I = \sqrt{\left|\left(k^2\frac{\partial^2 g}{\partial I_x^2} + 2kl\frac{\partial^2 g}{\partial I_x\partial I_z} + l^2\frac{\partial^2 g}{\partial I_z^2}\right)h(I_{xr},I_{zr})\right|}. \tag{2.71}$$

Since this the same for x and z the subscript on Q_I has been dropped.

2.9 Single Resonance with Tune Modulation

For the introduction of tune modulation one can start from (2.59) and add a modulation in the argument of the cosine so as to modulate the phase. Introducing the modulation tune $Q_m = f_m/f_{rev}$ and the modulation depths q_x and q_z the Hamiltonian reads

$$\begin{aligned} H(I_x,I_z,\phi_x,\phi_z,\theta) = {} & I_xQ_{x,0} + I_zQ_{z,0} + g(I_x,I_z) + \\ & + h(I_x,I_z)\cos\left[k\left(\phi_x + \frac{q_x}{Q_m}\sin(Q_m\theta+\alpha)\right) + \right. \\ & \left. + l\left(\phi_z + \frac{q_z}{Q_m}\sin(Q_m\theta+\alpha)\right) - p\theta\right]. \end{aligned} \tag{2.72}$$

Here it has been assumed that there is only one ripple frequency for both planes but the ripple depth is allowed to be different. This would be the case for a modulating quadrupole

where the horizontal and vertical beta functions are different. The case of more than one ripple frequency is described in Ref. [9] and qualitatively treated in Sec. 4.3. Replacing a continuously distributed modulation by a limited number of discrete modulating elements has been justified in [25].

The cosine in (2.72) can be expanded in a series via the Jacobi-Anger identity using Bessel functions [8,24]:

$$\cos\left[k\left(\phi_x + \frac{q_x}{Q_m}\sin(Q_m\theta+\alpha)\right) + l\left(\phi_z + \frac{q_z}{Q_m}\sin(Q_m\theta+\alpha)\right) - p\theta\right]$$
$$= \sum_{j_1,j_2=-\infty}^{+\infty} J_{j_1}\left(\frac{kq_x}{Q_m}\right) J_{j_2}\left(\frac{lq_z}{Q_m}\right)\cos\left(k\phi_x + l\phi_z + (j_1+j_2)(Q_m\theta+\alpha) - p\theta\right). \quad (2.73)$$

The resonance condition now reads

$$kQ_x(I^j_{xr}, I^j_{zr}) + lQ_z(I^j_{xr}, I^j_{zr}) + jQ_m = p \quad (2.74)$$

with $j = j_1 + j_2$. For each primary resonance at (I_{xr}, I_{zr}) a number of new resonances (sidebands) has been created. For each of these new resonances one can again compute island widths and the island tunes in analogy with (2.69-2.71) by replacing

$$h(I_{xr}, I_{zr}) \quad \text{by} \quad \sum_{\substack{j_1,j_2=-\infty \\ j_1+j_2=j}}^{+\infty} h(I^j_{xr}, I^j_{zr}) J_{j_1}\left(\frac{kq_x}{Q_m}\right) J_{j_2}\left(\frac{lq_z}{Q_m}\right). \quad (2.75)$$

To compute the distance between two sidebands for the case $I^j_{zr} = I_{zr}$, i.e. one of the actions is fixed, one can insert

$$Q_x(I^j_{xr}, I^j_{zr}) = Q_{x0} + \frac{\partial g}{\partial I_x}(I^j_{xr}, I_{zr}) \approx Q_{x0} + \frac{\partial g}{\partial I_x}(I_{xr}, I_{zr}) + \frac{\partial^2 g}{\partial I_x^2}(I_{xr}, I_{zr}) j\delta I_x \quad (2.76)$$

and

$$Q_z(I^j_{xr}, I^j_{zr}) = Q_{z0} + \frac{\partial g}{\partial I_z}(I^j_{xr}, I_{zr}) \approx Q_{z0} + \frac{\partial g}{\partial I_z}(I_{xr}, I_{zr}) + \frac{\partial^2 g}{\partial I_x \partial I_z}(I_{xr}, I_{zr}) j\delta I_x \quad (2.77)$$

into (2.74) and, using the condition (2.58), one obtains

$$\delta I_x = \frac{Q_m}{k\frac{\partial^2 g}{\partial I_x^2}(I_{xr}, I_{zr}) + l\frac{\partial^2 g}{\partial I_x \partial I_z}(I_{xr}, I_{zr})}. \quad (2.78)$$

If I_{xr} is fixed instead, the distance to the next sideband in the I_z direction is

$$\delta I_z = \frac{Q_m}{k\frac{\partial^2 g}{\partial I_x \partial I_z}(I_{xr}, I_{zr}) + l\frac{\partial^2 g}{\partial I_z^2}(I_{xr}, I_{zr})}. \quad (2.79)$$

Chirikov [4] used the overlap of sidebands, i.e. the condition $\delta I < \Delta I$, as a criterion for the onset of global chaos since particles can then be transported over wide amplitude regions in phase space. The overlap condition can be easily understood in two phase space dimensions but is more complicated in four dimensions.

2.10 Maps and Normal Forms

Particle dynamics can also be formulated in a "Hamiltonian free" context [8,12,13,26,27] based on the one-turn transfer map. The one-turn map M transforms the phase space coordinates $\vec{v}^i = (x^i, z^i, \sigma^i, p_x^i, p_z^i, p_\sigma^i) \equiv (\vec{x}^i, \vec{p}^i)$ at a certain location into the phase space coordinates $\vec{v}^f = (x^f, z^f, \sigma^f, p_x^f, p_z^f, p_\sigma^f) \equiv (\vec{x}^f, \vec{p}^f)$ after one turn:

$$\vec{v}^f = M(\vec{v}^i). \tag{2.80}$$

The map is in general nonlinear and may be expanded in a Taylor series as

$$v_j^f = T_{jk}^1 v_k^i + T_{jk_1k_2}^2 v_{k_1}^i v_{k_2}^i + ... \tag{2.81}$$

where the highest order of T^j is the order of the Taylor series expansion. It is possible to extract the map T in (2.81) from a tracking model (see for example [3]) using the "DA"-package [28] for automatic differentiation. The one-turn map can be as complex as the tracking model and the order n of the power series expansion is only limited by the available computer memory. For a conservative system the map M must be symplectic and the Taylor expansion (2.81) agrees with the symplectic map up to the expansion order n.

Lie algebra can be used for the analysis of the map M and its representation T [26, 29, 30]. If f and g are functions of some canonical phase space variables $(\vec{x}, \vec{p})$, one can introduce a Lie operator $: f :$ defined by

$$: f : \equiv [f, g] \equiv \frac{\partial f}{\partial \vec{x}} \frac{\partial g}{\partial \vec{p}} - \frac{\partial f}{\partial \vec{p}} \frac{\partial g}{\partial \vec{x}}, \tag{2.82}$$

and a Lie transformation by

$$\mathrm{e}^{:f:} \equiv \sum_{n=0}^{\infty} \frac{1}{n!} : f :^n, \tag{2.83}$$

where a power of $: f :$ has to be understood as the successive application of the operator. After transforming the coordinate system to the closed orbit as origin and changing to action-angle variables by

$$x_k = \sqrt{2I_k} \cos \phi_k, \;\; p_k = -\sqrt{2I_k} \sin \phi_k, \tag{2.84}$$

the map M can be transformed into a so called "normal form" N up to order $n-1$ using a nonlinear transformation A [27,31]:

$$M = A^{-1} N A \tag{2.85}$$

with the normal form

$$N = \exp\left\{ : -\vec{\mu} \cdot \vec{I} + D(\vec{I}) : \right\}. \tag{2.86}$$

In the transformed system the actions I_k are pseudo-invariants (up to the chosen order) and $A^{-1}[\vec{\mu}\cdot\vec{I}+D(\vec{I})]$ is the formal Pseudo-Hamiltonian in which $\vec{\mu}\cdot\vec{I}$ denotes the linear and $D(\vec{I})$ the nonlinear part, $\vec{\mu}=2\pi\vec{Q}$ are the phase advances. The transformation A is

$$A = A_n A_{n-1} ... A_3 A_2 A_1 = e^{:f_n:} e^{:f_{n-1}:} ... e^{:f_3:} A_2 A_1, \tag{2.87}$$

where A_2 and A_1 are the transformation to the closed orbit and action-angle variables respectively and the functions f_i are homogeneous polynomials of degree i in the x_k and p_k. From the Pseudo-Hamiltonian global quantities like tunes and detuning, chromaticity, driving terms and nonlinear invariants can be extracted.

The normal from transformation uses perturbation methods and breaks down at important resonances (see Sec. 2.6). However, resonances can be excluded from the normal form procedure and, when all resonances are excluded, one has

$$\tilde{M} = A_2 A_1 M A_2^{-1} A_1^{-1} \tag{2.88}$$

with

$$\tilde{M} = e^{:h_2:} e^{:h_3:} ... e^{:h_n:}, \tag{2.89}$$

which is a Dragt-Finn factorization [29]. The functions h_i are, like the functions f_i, homogeneous polynomials of degree i in the x_k and p_k.

The normal form process too can be done numerically (see for example [32]) so that map extraction and analysis can lead to power series expressions for extractable quantities with numerical coefficients. The analysis works with complex models, fully six-dimensional and with additional parameters like corrector strengths, that also would appear in the power series expansion. This has been used to do a higher order tune shift correction [33].

2.11 Dynamic Aperture

The motion in nonlinear systems can be classified as either regular or chaotic. In contradiction to the regular case, the individual motion of chaotic particles is not predictable even though it can be still described by the set of equations (2.4-2.6). An even infinitely small difference in the starting conditions of two chaotic particles leads to an exponentially growing difference of the phase space distance in time.

In two phase space dimensions bounded regular trajectories contain the particle motion. Therefore, the dynamic aperture can be defined as the regular trajectory at the largest bounded amplitude. However, in four or more phase space dimensions regular trajectories can not contain the motion and even particles starting from very small oscillation amplitudes may be lost if they are chaotic. In addition, phase space regions of regular and chaotic motion are often not well separated. There may exist a transition region where regular and chaotic motion alternates.

Moreover, in a real accelerator there may be no regular particle motion at all due to the interference of nonlinear forces with ripple, noise and scattering effects. For practical purposes one can define the dynamic aperture only considering a time interval of interest [34].

Different practical considerations may lead to different definitions for the dynamic aperture. For injection it could be the maximum betatron amplitude below which particles will survive the injection process, in a machine experiment it could be the maximum betatron amplitude above which no particles will survive a certain time.

In this work the term "dynamic aperture" will be used for betatron amplitudes, quoted in mm. The corresponding emittance will be denoted as "acceptance", given in mm·mrad.

Chapter 3

Basics of Particle Tracking

Despite many years of research there are still no reliable analytic tools available to predict the average loss time of chaotic particles and thereby the dynamic aperture. Hence particle tracking, which aims at simulating the single particle motion as realistically as possible, is the only trustworthy approach.

Accelerators consist of elements (drifts, dipoles, quadrupoles etc.) for which the s-dependent Hamiltonian (2.3) can be assumed to be constant. Using appropriate approximations the equations of motion can be integrated analytically for those elements (see Sec. 3.1) leading to formulae that connect the phase space variables at the entrance of an element to those at the exit. Element-by-element tracking codes evaluate successively such formulae in order to simulate the particle motion. In long-term tracking studies this is done for a large number of turns and it is important that the symplectic condition (2.10) is fulfilled to avoid the introduction of artificial dissipative effects [35].

Formulae connecting initial and final phase space variables of an element can be also viewed as a map. The maps of successive elements can be concatenated and doing that for all elements of an accelerator the one-turn map is obtained (Sec. 2.10). The evaluation of this one turn map has been proposed for particle tracking [36,37]. However, the complete polynomial map expansion of a realistic machine would be of very high order and needs to be truncated for practical reasons. In general the truncation violates the symplectic condition and the map must be symplectified [38]. Extensive tests have been performed [39, 40] that show that the preparation of such symplectic one-turn maps describing the long-term particle behavior correctly is a complex problem. This is the reason why only element-by-element tracking was used in this study.

In this chapter the modeling of elements is described and the approximations involved in this process are evaluated. After some general considerations about the tracking strategy postprocessing methods are presented and computing times are discussed.

3.1 Modeling of Elements

For the modeling of elements we will follow closely [14, 41–43] since these papers are the theoretical framework for the tracking code SIXTRACK which was used for the simulations in this work. One starts from the Hamiltonian (2.3) in Sec. 2.1

$$\begin{aligned} H(x,z,\sigma,p_x,p_z,p_\sigma;s) = p_\sigma - (1+\eta)\cdot[1+K_x(s)\cdot x + K_z(s)\cdot z]\times \\ \times\left\{1-\frac{\left(p_x-\frac{e}{p_0}A_x(s)\right)^2+\left(p_z-\frac{e}{p_0}A_z(s)\right)^2}{(1+\eta)^2}\right\}^{1/2} - \\ -[1+K_x(s)\cdot x + K_z(s)\cdot z]\cdot\frac{e}{p_0}A_s(s) \end{aligned} \tag{3.1}$$

and integrates the equations of motion (2.4) piecewise for the element under consideration.

In order to make computations tractable the square root in the second term in (3.1) is expanded in a power series

$$\left\{1-\frac{\left(p_x-\frac{e}{p_0}A_x\right)^2+\left(p_z-\frac{e}{p_0}A_z\right)^2}{(1+\eta)^2}\right\}^{1/2} \approx 1-\frac{(p_x-\frac{e}{p_0}A_x)^2}{2\cdot(1+\eta)^2}-\frac{(p_z-\frac{e}{p_0}A_z)^2}{2\cdot(1+\eta)^2} \tag{3.2}$$

and only terms up to quadratic in $(x, z, (p_x - \frac{e}{p_0}A_x), (p_z - \frac{e}{p_0}A_z), \eta)$ are kept (compare Sec. 2.3). To proceed further, the vector potential $\vec{A}$ must be given for each element. Some examples can be found in Tab. 3.1 [14].

Again (compare Sec. 2.3) the curvatures K_x, K_z are assumed to be small and their crossterms with $g, \lambda, \ldots$ in the third term in (3.1) are neglected. Similar to the weak focusing of the dipoles these terms would lead to a "weak" chromaticity change due to quadrupoles etc. Now the equations of motion (2.4) can be integrated. A quadrupole may serve as an example for the thick-lens and thin-lens model respectively.

Thick-lens model

The equations of motion (2.4) read [14]

$$x' = \frac{p_x}{[1+f(p_\sigma)]}, \quad p_x' = -gx, \tag{3.3}$$

$$z' = \frac{p_z}{[1+f(p_\sigma)]}, \quad p_z' = -gz, \tag{3.4}$$

$$\sigma' = 1 - \frac{\mathrm{d}f}{\mathrm{d}p_\sigma}(p_\sigma) - \frac{1}{2}[(x')^2+(z')^2]\frac{\mathrm{d}f}{\mathrm{d}p_\sigma}(p_\sigma), \quad p_\sigma' = 0, \tag{3.5}$$

Table 3.1: The vector potential for various elements.

element type	vector potential normalized with $\frac{e}{p_0}$			definitions
	$\frac{e}{p_0}A_x$	$\frac{e}{p_0}A_z$	$\frac{e}{p_0}A_s$	
horizontal dipole			$-\frac{1}{2}[1+K_x x]$	$K_x = \frac{e}{p_0}B_z$
normal quadrupole			$\frac{1}{2}g(z^2-x^2)$	$g = \frac{e}{p_0}\left(\frac{\partial B_z}{\partial x}\right)_{x=z=0} = 2\mathfrak{a}_{20} = -2\mathfrak{a}_{02}$
normal sextupole			$-\frac{\lambda}{6}(x^3-3xz^2)$	$\lambda = \frac{e}{p_0}\left(\frac{\partial^2 B_z}{\partial x^2}\right)_{x=z=0} = 6\mathfrak{a}_{30} = -2\mathfrak{a}_{12}$
cavity			$-\frac{1}{\beta_0^2}\frac{L}{2\pi h}\frac{eV(s)}{E_0}\cos\left[h\frac{2\pi}{L}\sigma+\Phi\right]$	h harmonic number V voltage Φ phase
solenoid	$-Sz$	$-Sx$		$S = \frac{1}{2}\frac{e}{p_0}B_s(0,0,s)$

where η has been replaced by the function

$$f(p_\sigma) \equiv \eta = \frac{1}{\beta_0}\sqrt{(1+\beta_0^2 p_\sigma)^2 - \left(\frac{m_0c^2}{E_0}\right)^2} - 1 \tag{3.6}$$

to emphasize its dependence on p_σ. Its derivative with respect to p_σ is

$$\frac{\mathrm{d}f}{\mathrm{d}p_\sigma}(p_\sigma) = \frac{\beta_0\ (1+\beta_0 p_\sigma)}{\sqrt{(1+\beta_0 p_\sigma)^2 - \left(\frac{m_0c^2}{E_0}\right)}} \equiv \frac{v_0}{v}. \tag{3.7}$$

Introducing

$$\bar{g} = \frac{g}{1+f(p_\sigma)} \tag{3.8}$$

the integration over the quadrupole length Δs gives for the transverse coordinates

$$\begin{pmatrix} x^f \\ x'^f \\ z^f \\ z'^f \end{pmatrix} = \underline{M} \begin{pmatrix} x^i \\ x'^i \\ z^i \\ z'^i \end{pmatrix} \tag{3.9}$$

with

$$\underline{M} \;= (M_{mn}) = \begin{pmatrix} \cos(\sqrt{|\bar{g}|}\Delta s) & \frac{1}{\sqrt{|\bar{g}|}}\sin(\sqrt{|\bar{g}|}\Delta s) & 0 & 0 \\ -\sqrt{|\bar{g}|}\sin(\sqrt{|\bar{g}|}\Delta s) & \cos(\sqrt{|\bar{g}|}\Delta s) & 0 & 0 \\ 0 & 0 & \cosh(\sqrt{|\bar{g}|}\Delta s) & \frac{1}{\sqrt{|\bar{g}|}}\sinh(\sqrt{|\bar{g}|}\Delta s) \\ 0 & 0 & \sqrt{|\bar{g}|}\sinh(\sqrt{|\bar{g}|}\Delta s) & \cosh(\sqrt{|\bar{g}|}\Delta s) \end{pmatrix} \tag{3.10}$$

for $\bar{g} > 0$. For the case $\bar{g} < 0$ the trigonometric functions have to be replaced by the corresponding hyperbolic functions and vice versa. The solution for the longitudinal coordinates reads [43]

$$\begin{aligned} \sigma^f &= \sigma^i + \Delta s\ (1 - \frac{\mathrm{d}f}{\mathrm{d}p_\sigma}(p_\sigma)) \\ &\quad - \frac{9}{4}\frac{\mathrm{d}f}{\mathrm{d}p_\sigma}(p_\sigma)\left\{(x^i)^2\left[\Delta s - M_{11}\ M_{12}\right] - (z^i)^2\left[\Delta s - M_{33}\ M_{34}\right]\right\} \\ &\quad - \frac{1}{4}\frac{\mathrm{d}f}{\mathrm{d}p_\sigma}(p_\sigma)\left\{(x'^i)^2\left[\Delta s - M_{11}\ M_{12}\right] + (z'^i)^2\left[\Delta s - M_{33}\ M_{43}\right]\right\} \\ &\quad - \frac{1}{2}\frac{\mathrm{d}f}{\mathrm{d}p_\sigma}(p_\sigma)\left\{(x^i x'^i)M_{12}\ M_{21} + (z^i z'^i)M_{34}\ M_{43}\right\} \\ p^f_\sigma &= p^i_\sigma. \end{aligned} \tag{3.11}$$

and (3.9-3.11) fulfill the symplectic condition (2.10) [43].

Thin-lens model

In the thin-lens approximation the momentum variables experience a sudden change (which is usually referred to as a "kick") at a certain longitudinal position s_0 whereas the transverse position coordinates are retained. The quadrupole is modeled as

$$g(s) = g(s_0)\ \Delta s\ \delta(s - s_0), \tag{3.12}$$

δ being the delta function. The equations of motion take the form

$$x' = \frac{p_x}{[1 + f(p_\sigma)]}, \quad p'_x = -gx\Delta s\delta(s - s_0), \tag{3.13}$$

$$z' = \frac{p_z}{[1 + f(p_\sigma)]}, \quad p'_z = -gz\Delta s\delta(s - s_0), \tag{3.14}$$

$$\sigma' = 1 - \frac{\mathrm{d}f}{\mathrm{d}p_\sigma}(p_\sigma) - \frac{1}{2}[(x')^2 + (z')^2]\frac{\mathrm{d}f}{\mathrm{d}p_\sigma}(p_\sigma), \quad p'_\sigma = 0, \tag{3.15}$$

and have the solution

$$x^f = x^i, \quad p^f_x = p^i_x - g(s_0)\Delta s x^i, \tag{3.16}$$

$$z^f = z^i, \quad p_z^f = p_z^i - g(s_0)\Delta s z^i, \tag{3.17}$$

$$\sigma^f = \sigma^i, \quad p_\sigma^f = p_\sigma^i. \tag{3.18}$$

The computing time for the evaluation of (3.16-3.18) is considerably less than for (3.9-3.11) and in Ref. [14] it is shown that the symplectic condition is preserved.

In the current SIXTRACK version [3] dipoles and quadrupoles can be modeled as either thick or thin lenses. All higher-order elements like sextupoles, octupoles etc. are treated in the thin-lens approximation.

3.2 Approximations and Numerical Errors

This section presents an evaluation of the approximations made in the last section.

Gravitational forces
In Eq. (3.1) gravitational forces are not considered. HERA-p at injection energy shall serve as an example why this is justified.

(a) Gravitational force on a proton:
$F_{grav} = m_p g_{grav} = 1.67 \cdot 10^{-27}\text{kg} \times 9.81\text{m/s}^2 = 1.64 \cdot 10^{-26}$ N

(b) Magnetic force on a vertically displaced proton in a quadrupole:
$F_{magn} = e v_p \left(\frac{\partial B_x}{\partial z}\right) z = v_p p_0 g_{quad} z = 40 \cdot 10^9 \cdot 1.6 \cdot 10^{-19}$ VAs $\times$ 0.034 m^{-2} $\times$ z
$= 2.43 \cdot 10^{-10}$N/m $\times$ z

Even when taking into account that the quadrupoles in HERA-p fill only 6.6% of the machine length, the magnetic forces are many orders of magnitude greater than the gravitational ones for a tiny vertical displacement z. Note that the magnetic fields are only known up to a precision of about 10^{-5}.

Taylor expansion of the square root in (3.1)
The approximation (3.2) causes an error Δ which is

$$\Delta = \left| \left\{ 1 - \frac{\left(p_x - \frac{e}{p_0}A_x\right)^2 + \left(p_z - \frac{e}{p_0}A_z\right)^2}{(1+\eta)^2} \right\}^{1/2} - 1 + \frac{(p_x - \frac{e}{p_0}A_x)^2}{2\cdot(1+\eta)^2} + \frac{(p_z - \frac{e}{p_0}A_z)^2}{2\cdot(1+\eta)^2} \right| . \tag{3.19}$$

Disregarding longitudinal magnetic fields and restricting to on-momentum particles the error (3.19) reduces to

$$\Delta = \left| \sqrt{1 - (x')^2 - (z')^2} - 1 + \frac{(x')^2}{2} + \frac{(z')^2}{2} \right| . \tag{3.20}$$

The error becomes larger with increasing y' and from the emittance

$$\epsilon_y = \frac{1}{\beta_y} \left(y^2 + (\alpha_y y + \beta_y y')^2 \right), \tag{3.21}$$

one obtains y_{max} at locations with $\alpha = 0$ under the condition $y = 0$. It follows that

$$y_{max}^2 = \frac{\epsilon_{max}}{\beta_{y,min}}. \tag{3.22}$$

Assuming round beams ($\epsilon_x \approx \epsilon_z$) one has:

1. SPS at 120 GeV: $\epsilon_{max} \approx 4 \cdot 10^{-6}$ m, $\beta_{min} \approx 20$m, $\Rightarrow \Delta_{max} \lessapprox 2 \cdot 10^{-7}$
2. HERA at 40 GeV: $\epsilon_{max} \approx 2 \cdot 10^{-6}$ m, $\beta_{min} \approx 10$m, $\Rightarrow \Delta_{max} \lessapprox 2 \cdot 10^{-7}$
3. LHC at 450 GeV: $\epsilon_{max} \approx 4 \cdot 10^{-7}$ m, $\beta_{min} \approx 10$m $\Rightarrow \Delta_{max} \lessapprox 4 \cdot 10^{-8}$

These values have to be compared with 1 since the Taylor expansion was made around this value.

Due to the approximation (3.2) drift spaces, dipoles and quadrupoles become linear elements if only the transverse phase space coordinates are considered (coasting beam). The change of the transverse coordinates can then be described by matrices like (3.10). Going to higher orders in the approximation (3.2) or in the 6-dimensional case all elements are nonlinear.

Disregarding cross-terms of K_x, K_z with higher order multipoles

These terms are only present in magnets that combine bending with another function. Among the three machines considered in this study the HERA proton ring is the only one to have quadrupole, sextupole and decapole correction coils in the main dipoles.

For a comparison the coefficients for x^3 are given (see Tab. 3.1 and Eq. (3.1)).

(a) Sextupole for chromaticity compensation at injection energy: $|\frac{\lambda}{6}| \approx 10$ m^{-3} (corresponding to $b_3 \approx 5 \cdot 10^{-4}$ in the correction coils) $\Rightarrow |\frac{\lambda}{6}|\ x^3 \approx 10$ m^{-3} x^3

(b) Horizontal bending: $|K_x| = 0.0017$m^{-1}, tuning quadrupole strength: $|g| \lessapprox 0.005$ m^{-2} $\Rightarrow |\frac{1}{4} K_x\ g|\ x^3 \lessapprox 2.1 \cdot 10^{-6}$ m^{-3} x^3.

The sextupoles strength introduced by the bending in the tuning quadrupoles is about 10^{-7} of the correction sextupole strength which is much smaller than the measurement precision of the correction sextupole strength.

Fringe fields

At the end of magnets Maxwells equations impose nonzero components A_x, A_z . These fringe fields can be important in small rings or at locations with very large beta functions [44, 45] and there are codes that can handle these fields [46, 47]. For large machines like the SPS, HERA or the LHC the effect of fringe fields is assumed to be small and they are neglected in tracking simulations.

Thin-lens approximation

The thin lens approximation has the advantage to be symplectic in any expansion order of (3.2). But to model a long element to a high precision many thin lenses may be necessary [48]. Often one kick is sufficient and one can gain in computing speed compared to a thick lens model (see for example Ref. [14] where a thick- and a thin-lens model of the LHC is compared).

Rounding errors
In references [49–51] the dependence of the rounding error Δ_{num} of the particle position in phase space as a function of the turn number N was studied. Three methods were employed: Observing the nonconservation of constants of motion in the linear case, the comparison between results computed with different accuracies and tracking a particle for some turn number in the forward direction, inverting its direction and tracking it back for the same turn number to its starting position. The results can be summarized as follows:

- For a linear machine: $\Delta_{num} \sim N$.
- For a nonlinear machine, regular trajectory: $\Delta_{num} \sim N^2$.
- For a nonlinear machine, chaotic trajectory: $\Delta_{num} \sim e^N$.

In all cases the error mainly occurs in the phase. For the betatron amplitude a_x in Ref. [51] a dependence of the form

$$a_x(N) = a_{x0}(1 - \alpha N) \tag{3.23}$$

was found for a realistic model of the HERA proton ring where α was of the order of 10^{-13}. Formula (3.23) describes a damping of amplitudes which results from violating the symplectic condition due to rounding errors. With turn numbers up to 10^7, as considered in this study, the amplitude error due to (3.23) is small enough to be disregarded.

In tracking programs approximations are unavoidable. Their effect on the long-term stability of particle motion is not easy to estimate and one motivation for the SPS dynamic aperture experiment was to test the ability of existing tracking programs to reproduce the dynamic aperture and other complicated features of the particle motion in phase space.

3.3 Tracking Recipe

From the experience gained in systematic tracking studies some recommendations can be derived [52, 53]:

- The linear machine functions should be well understood since the nonlinear behavior depends on them (see for example Eq. (2.35)). Other basic parameters like closed orbit, linear coupling, chromaticity and physical apertures should be known accurately as well and whenever possible measured quantities should be compared with the model or included in the model.
- One of the most important properties of a nonlinear oscillator system is the amplitude dependent tune. The model should reproduce this feature with a good precision.
- Due to the possible complicated structure of the phase space different regions should be tested by varying the start amplitudes. However, it is not necessary to vary the start phase since usually some 1000 turns are sufficient to sample the whole phase range and the tracking data contain this information.

- Control parameters of an accelerator should be either varied systematically (tunes, corrector strength, momentum variation) or statistically (closed orbit seeds, magnetic error seeds) to scan a realistic range.
- Long-term tracking runs should be preceded by a short-term analysis. In particular, before producing survival plots, the chaotic regions in phase space should be determined (Sec. 3.4).
- The phase space coordinates should be stored turn-by-turn. There are various methods to analyze these data (Sec. 3.4).

3.4 Postprocessing of Tracking Data

Turn-by-turn tracking data hold a large amount of information about the dynamical system under study. This information can be extracted by postprocessing methods which can be often also applied to turn-by-turn experimental data. In this section the methods are described which will be used later.

Poincaré surface of section
Plotting the phase space coordinates after each turn one obtains the Poincaré surfaces of section (Fig. 3.1). The motion in phase space can be directly viewed (Fig. 3.1 (a),(b)) and nonlinear motion, resonance islands and chaos can be found. From phase space plots important contributions to the distortion function $\mathfrak{F}$ (Eq. 2.45) can be identified (by counting the numbers of maxima of a distorted orbit) and resonance parameters like the island width can be extracted. However, it may be difficult to interpret the phase space projections of a 4-dimensional coupled motion onto a (y, y')-plane. In this case it is helpful to fix the phase angle of the other plane to obtain a pseudo one-dimensional system (see for example Ref. [52]).

Tunes
Particle motion can also be described in the frequency domain [54], the tunes (Q_x, Q_z, Q_s) being the most prominent frequencies. Linear coupling, resonances [55], modulation sidebands and chaos [56] are observable in the spectra. The frequencies can be obtained by computing FFT's (Fast Fourier Transforms [57]), the averaged phase advance per turn [3] or other algorithms like NAFF (Numerical Algorithm for the Fundamental Frequency [54]).

Smear
The smear S of a function f can be defined as [58]

$$S(f) \equiv \sqrt{\frac{\langle f^2 \rangle - \langle f \rangle^2}{\langle f \rangle^2}} \quad \text{with} \quad \langle f \rangle \equiv \frac{1}{N} \sum_{n=1}^{N} f_n. \tag{3.24}$$

For the function f a constant of linear motion (e.g. Courant-Snyder invariant) is chosen. If the linear coupling is taken out, the smear is zero for linear machines. A large smear

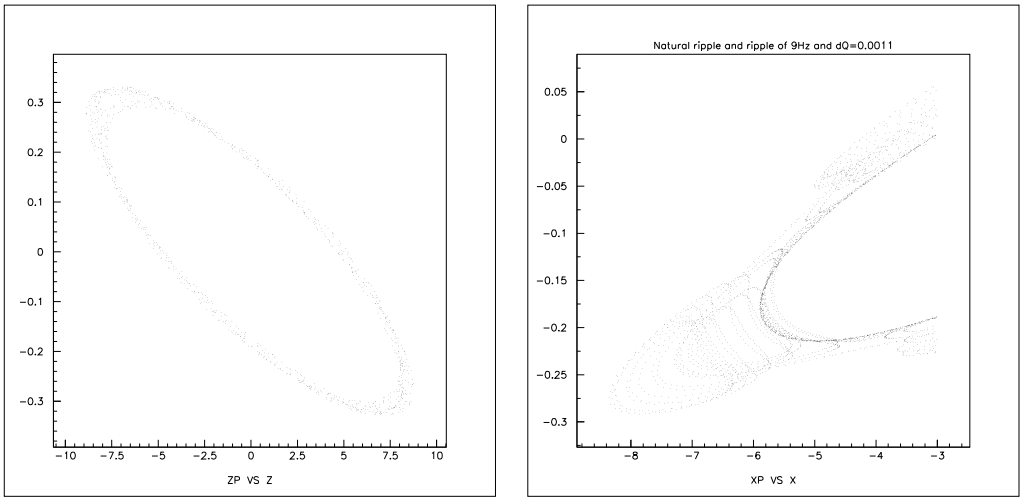

(a) (b)

Figure 3.1: Phase space plots. Part (a) shows the projection of the 4-dimensional phase space coordinates onto the (z, z') plane after each turn for a particle under the influence of nonlinear fields. In part (b) the projection onto the (x, x') plane is depicted for a 5^{th} order resonance island under the influence of slow tune modulation.

indicates strong nonlinearities or resonances. If the smear is small one can plot survival times versus start amplitudes, otherwise the averaged amplitude should be used.

Lyapunov analysis
In a regime where resonances are stabilized (resonance islands) chaoticity is a prerequisite for particles to be lost. Therefore, the determination of the chaotic border gives a lower limit for the dynamic aperture (but see Sec. 2.11). Chaoticity manifests itself in the exponential growth of the distance in phase space of initially close-by particles; for the case of regular motion this distance grows only linearly [51]. Observing this distance is a very sensitive method due to its differential nature (Fig 3.2) and for the chaoticity test turn numbers about a factor 10 smaller than for survival plots are often sufficient.

Survival plots
With long-term tracking studies survival plots have been introduced [51,59] in which the survival time of particles versus amplitude is shown (Fig. 3.3). They are the most direct and most reliable way to determine the dynamic aperture in a simulation. The loss time increases normally exponentially with decreasing amplitudes and tends to infinity when the regular area in phase space is reached.

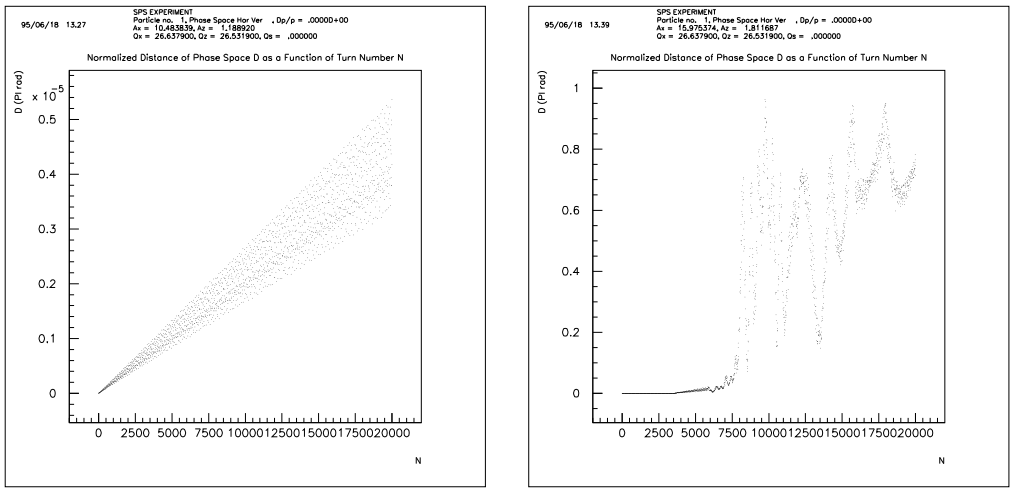

(a) (b)

Figure 3.2: Time evolution of the distance in phase space for a pair of initially close by particles. Part (a) shows a regular, part (b) a chaotic chaotic case. Note the different vertical scales.

Averaging
When tune modulation is switched on, the phase advance can be averaged over one tune modulation period to derive meaningful numbers for the tunes. The particle amplitudes can be averaged as well over that period to study their mean and rms value as a function of time.

3.5 Computing Times

Tracking for large hadron machines can be very time consuming for a number of reasons. Accelerators and storage rings are operated in a regime far away from low order resonances and instabilities of motion may develop over many turns due to small field errors. The chaotic border gives a lower estimate for the dynamic aperture but it is often much too pessimistic and only brute force tracking can give reliable results. To describe a realistic beam various parameters must be scanned (tunes, corrector strength, closed orbit seeds, start amplitudes etc.) and as a result a large number of particles has to be tracked.

To simulate some minutes of real machine time it is necessary to track particles for days or even weeks with todays computer technology (IBM-SP2 RISC station clusters at CERN [61] and DESY). There is still a factor of about 40 to 200 between real and simulation time (Tab.3.2). However, a larger number of particles can be distributed on a farm of CPUs when only single particle effects are considered.

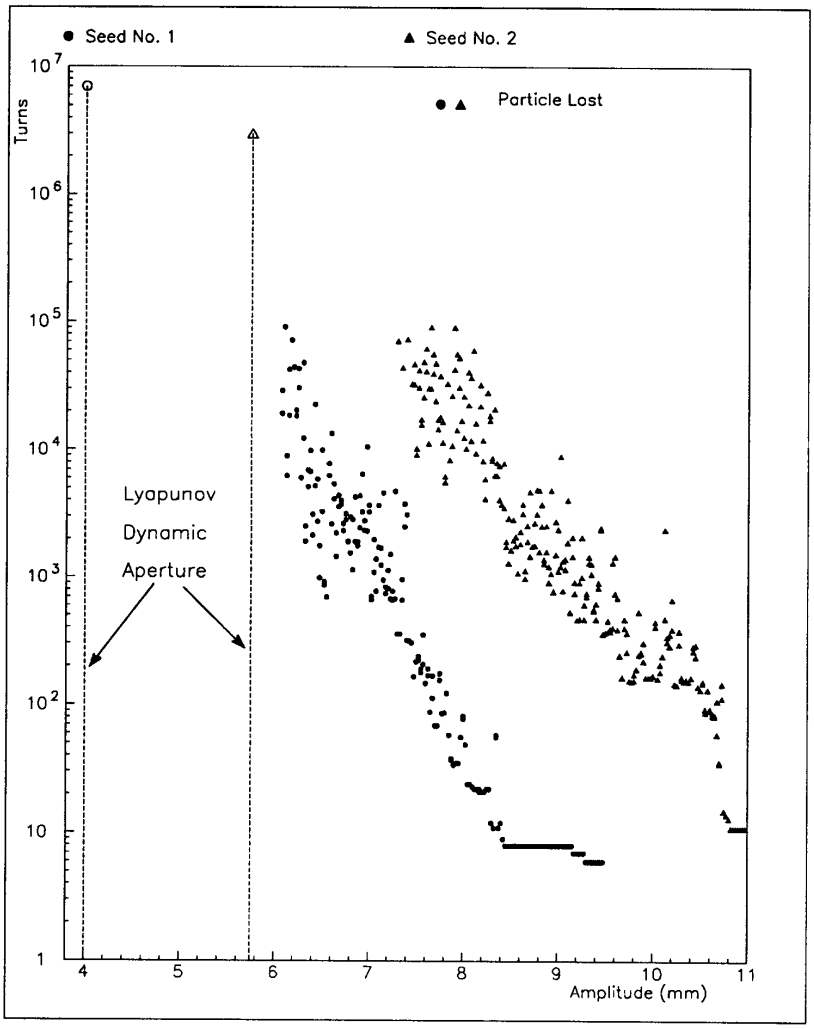

Figure 3.3: Survival plot for the LHC [60]. For two sets of magnetic multipole errors (denoted as "Seed No.1" and "Seed No. 2") the chaotic border and the spread of the amplitude dependent loss times is shown.

Table 3.2: Comparison of real and simulation time. The computation time is given for one particle pair using the vectorized version of SIXTRACK [3] on IBM-SP2.

machine	real time per turn [ms]	computation time per turn [ms]
SPS	0.023	≈ 1
HERA-p	0.021	≈ 14
LHC	0.089	≈ 20

Chapter 4

The Dynamic Aperture Experiment at the SPS

With the planning of a new generation of large hadron colliders like the Superconducting Super Collider, the Large Hadron Collider and the Relativistic Heavy Ion Collider a growing interest developed in transverse nonlinear phenomena that lead to dynamic aperture limitations. Experimental programs were started in the US and in Europe. In the E778 experiment at the Fermilab Tevatron [62–68] detuning and smear measurements were made, island captures with and without tune modulation observed and time dependent beam profiles measured. All experiments were done close to a $\frac{2}{5}$ resonance and the Hamiltonian formalism was used for the description. The beam losses were fitted to a global diffusion model. At the Indiana University Cyclotron Facility low order resonances have been investigated with and without tune modulation and compared with Hamiltonian models [70–73].

Since 1986 dynamic aperture experiments have been performed at the CERN SPS. Four periods can be distinguished and in the next section a short description of the first three of them will be given. More details can be found in Ref. [11]. The following sections of this chapter cover the fourth period in detail. The instrumentation and experimental conditions are described and results of the scraper and the wire scanner experiments are presented. A phenomenological description of the loss mechanism is given.

4.1 Chronological Overview

In 1986 the basic machine set-up for the SPS experiments was fixed (see Sec. 4.2.2). The otherwise very linear machine was made nonlinear by powering 8 strong sextupoles. Two sextupole configurations were investigated: one excited 3^{rd} order resonances and the other one suppressed these resonances and drove only higher order ones. The second configuration has been used in all following experiments since it resembles more a storage ring operated far away from low order resonances. With wire scanner beam profiles the phase space distortions due to the 3^{rd} order resonances could be observed and the short-

term dynamic aperture (in the order of seconds) could be measured. Tracking simulations with $10^2 - 10^3$ turns were able to reproduce the short-term dynamic aperture quite well. It became apparent that a large vertical closed orbit can excite skew resonances and preliminary studies with a tune modulation of some 10^{-3} were done. The first long-term studies (in the order of minutes) were carried out and it was found that RF noise leads to an unacceptable high loss rate. Therefore the RF was switched off in the following long-term studies.

In 1988 the amplitude dependent tunes were measured. They agreed well with those of the tracking model. In long-term studies a slow particle loss was found using the following method: a horizontal scraper was moved in until the lifetime dropped. Retracting the scraper by some millimeters an amplitude region free of particles was created that was filled again by a diffusion-like process. In tracking regular motion was found at the same amplitudes where "diffusion" had been measured. Therefore it was concluded that an important effect was missing in the simulations. One good candidate was tune ripple, arising from power supply ripple, and tracking showed a sizeable reduction of the dynamic aperture for a tune modulation depth of some 10^{-3}. In the same study it was also found that low frequencies (in the range from 10 Hz to 600 Hz) are potentially more harmful for the stability of particle motion than higher ones. Furthermore, it was demonstrated that the effect of tune modulation introduced by a large number of elements can be replaced by a single element in the simulation.

From 1989 to 1991 it was attempted to obtain quantitative and reproducible results from diffusion rate measurements as a function of betatron amplitude, ripple frequency and ripple depth. However, it turned out that a much better control of the machine parameters was necessary to obtain clear results. Therefore, the closed orbit, the linear coupling and the chromaticity were corrected very well. It became clear that the beam had to be considered as a particle distribution in amplitude and momentum and it was found that the amplitude range with measurable diffusion rates (large enough to be measurable but not too fast) was in the order of the beam size. Besides all improvements it was still difficult to obtain quantitative results. Nevertheless some valuable results could be obtained. The natural tune ripple was measured and the detuning introduced by the sextupoles could be partly corrected with octupoles leading to an aperture increase of about 30%. Tracking simulations were done up to $2.6 \cdot 10^7$ turns (10 min storage time in the SPS) and it was found that an aperture reduction of about 10% still occured beyond 1 million turn. One qualitative finding in the experiment was that the loss rates depend strongly on the ripple depth but only weakly on the ripple frequency. Two modulation frequencies applied at the same time were found to be more harmful than a single frequency of the same total modulation depth. Another feature sometimes found in the experiments was a "shoulder" in the time-dependent intensity signal: after retracting the horizontal scraper (in the procedure described above) the intensity stayed constant for a certain time and decreased then linearly with time without a pronounced transition period. Such a behavior seems to be in contradiction with a simple diffusion model [74].

In the last period, from 1992 to 1994, a systematic study of the loss rates as a function

of modulation frequency and depth was done with the refined machine set-up (Sec. 4.3) and the beam was studied with continuous wire scan profiles (Sec. 4.4).

4.2 Preparation of the SPS and the Tracking Model

In this section the instrumentation for the SPS dynamic aperture experiment will be described, in particular the data acquisition system BOSC and the wire scanner system. The experimental conditions are presented as well as the tracking model for the SPS. It is shown that the model reproduces the basic nonlinear properties of the SPS. This is a prerequisite for long-term studies.

4.2.1 Instrumentation for the SPS Experiment

The CERN SPS is a synchrotron with 1100 m mean radius. It can accelerate protons from 14 GeV up to 450 GeV for fixed target experiments. In the following the general instrumentation needed for the aperture experiment (see Fig. 4.1) is described.

Sizeable nonlinearities are introduced by 8 sextupoles (part of the slow extraction system) which are about 10 times stronger than the chromaticity sextupoles located at the focusing quadrupoles. They are grouped in two families and are excited with different polarity (Fig. 4.1) to avoid a change of the chromaticity and the excitation of third order resonances. Analytical calculations using equations (2.54, 2.55) predict that these strong sextupoles lead to a detuning with action 10 times larger than in the normal machine.

A single quadrupole (BA1 in Fig. 4.1) is used for tune modulation. Up to a modulation frequency of about 200 Hz and a modulation depth of $\Delta Q_x = \pm 1.5 \cdot 10^{-3}$, which is more than ten times the natural one, the shape of a sinusoidal input signal is not disturbed and the tune modulation depth is proportional to the input voltage.

A kicker (BA6 in Fig. 4.1) is used to increase the betatron amplitudes of particles in the beam. It was calibrated several times and shows a very linear behavior in the used voltage range (Fig. 4.2).

Pairs of horizontal and vertical scrapers (BA1 in Fig. 4.1) serve as aperture limiters and the losses at these scrapers are detected by a close-by scintillator (45 m downstream). Scraper positions and the loss detector signal are recorded by the BOSC system (see Sec. 4.2.1).

Momentum and tune distributions are measured with a Schottky system [75]. Using the same hardware, a continuous tune measurement system has been set-up to measure the natural tune ripple spectrum spectrum (Fig. 4.9).

The turn-by-turn beam data acquisition system and the flying wire system which are most relevant for the experiment will now be described in some detail.

Data acquisition system BOSC

The turn-by-turn data acquisition system BOSC [76, 77] (the acronym stands for Beam OSCillations) was originally intended to be used in the SPS to measure the intensity and

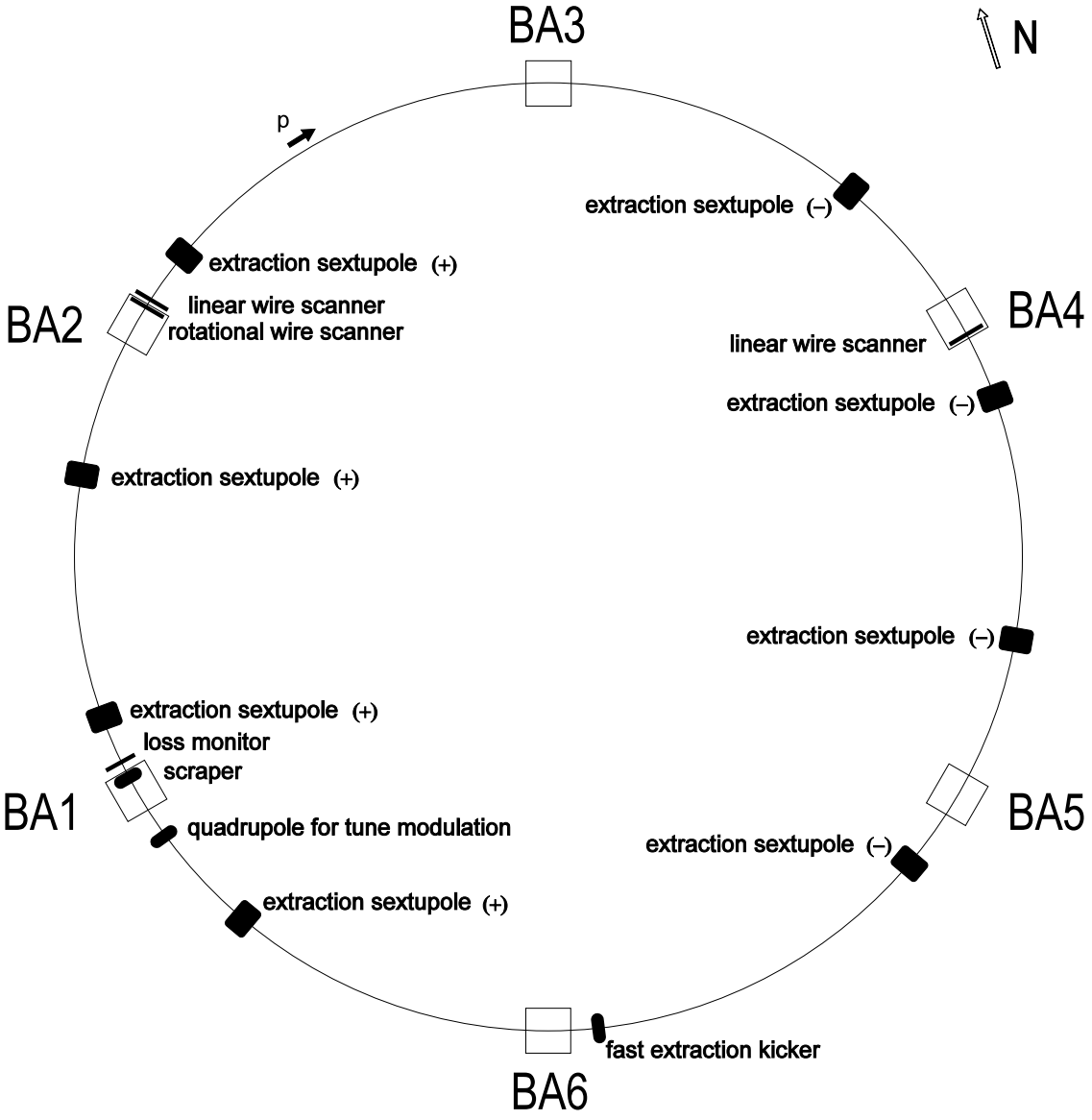

Figure 4.1: Instrumentation at the SPS. The 8 strong sextupoles, the quadrupole for tune modulation and the kicker magnet are shown at their locations in the SPS. The positions of the linear and rotational wire scanners, the scrapers and the loss monitor are given as well. (BA stands for access hall.)

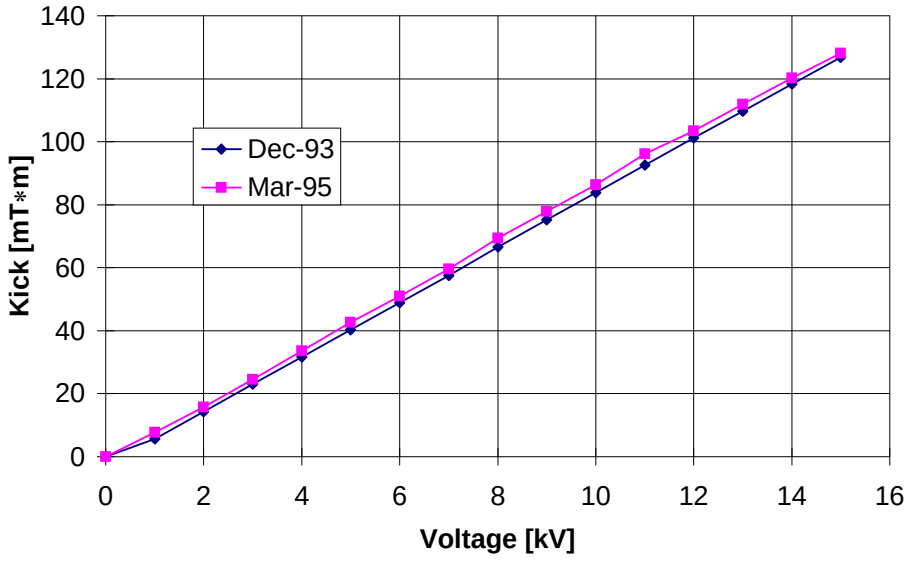

Figure 4.2: Calibration of the kicker in 1993 and 1995.

the position of the individual proton and anti-proton bunches over a full machine cycle. Now a wide range of different signals can be recorded. The system consists of a VME crate with a 68030 CPU card, a timing module, a bunch selector card and 12 ADC cards each with two channels to acquire and store data of up to one million turns. Three such crates on the SPS site and one crate on the LEP site can be addressed by Apollo or HP-UX workstations via Ethernet and Token Ring. Very flexible measurement requests can be sent to the crates in data-structures which are then filled with the requested data and sent back to the workstation for processing. In the crate a complex control software runs under OS9. Several application software programs now exist running either on Apollo or on HP-UX workstations under Xwindows/MOTIF. Apart from its use in the SPS dynamic aperture experiment, with its constantly changing requirements, BOSC also provides the operational tune measurement in the SPS.

Hardware description
The BOSC acquisition system in its final form is housed in a VME crate. It can handle up to 24 analog signals which are taken from homodyne receivers. They are organized in 12 dual channel electronic cards (*dual sampler*) which contain 1 MByte memory for each channel to allow the measurement turn-by-turn over a period of more than 20 s in the SPS. The acquisition bandwidth of 5 MHz is well matched to the bandwidth of the receivers. A logic cell array common to both channels on the ADC card acts as a slave to the crate central processor unit (68030). The system is mainly intended for the measurement of single bunches. The *bunch selector* picks a given bunch which circulates in the machine. The time resolution of this selection is determined by the bandwidth of

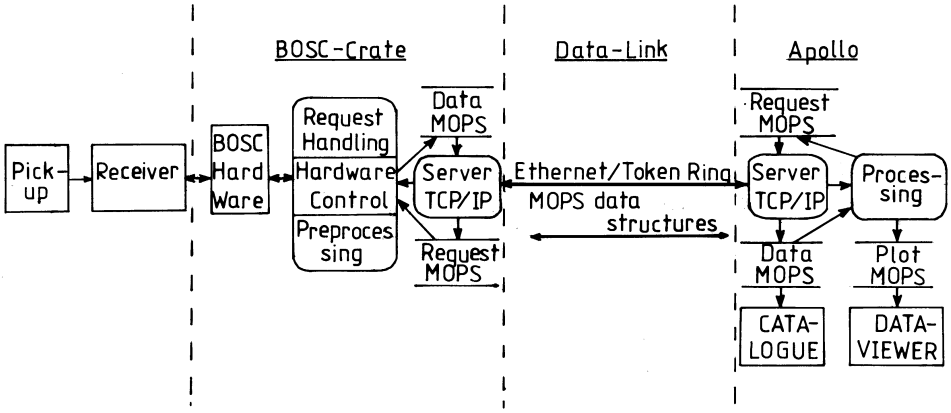

Figure 4.3: Setup of BOSC.

the system and is at present in the order of 200 ns. Special care was taken to isolate the low power analog circuits from the high power digital circuitry. The connection between the two is made in the *VME bridge* module. The information concerning the machine cycle time is fed into the system by a timing module.

At present three units are installed in the SPS and one in LEP:

- The first unit is dedicated to turn by turn position measurements. It is used to determine the machine tunes. A number of channels are connected to 200 MHz receivers. They are well adapted to measure single lepton bunches. However, they are also used to measure the SPS proton beams bunched at 200 MHz. Special low frequency FET amplifiers with a bandwidth reduced to 5 MHz to match the acquisition system are connected to a second set of channels. They allow the measurement of bunched and unbunched beams. The excitor for this measurement can either be a special fast kicker magnet or the deflector plates of the transverse feedback system. The excitation of the latter is controlled by BOSC using the *sequencer* unit.

- A second BOSC unit is devoted to single bunch intensity measurements. The signals are generated by 20 MHz homodyne receivers.

- A third unit acquires much slower signals generated by DC current transformers, collimator movements and scintillators.

- The LEP unit records the intensity and beam position signals of one BPM for one bunch of electrons and positrons respectively.

Control software description
The control software [78], running under OS9 on the 68030 processor, has the following tasks: setting up the communication between the crate and the workstation, setting and

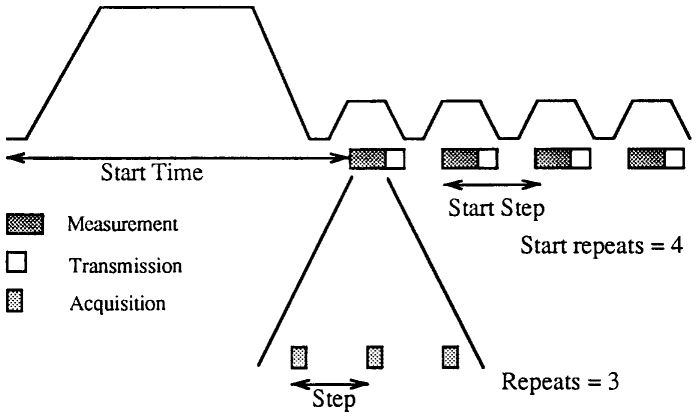

Figure 4.4: Time structure of a BOSC measurement [78]. Shown is the SPS super cycle of 14.4 s. The first ramp is the proton cycle, the four following ramps are for the acceleration of leptons.

changing some hardware parameters, accepting measurement requests from a workstation, starting the data acquisition on the crate and sending the data to the workstation after an acquisition has been made. It is capable of handling several requests simultaneously on the same crate.

The communication is done over Ethernet and Token Ring where sockets under TCP/IP are used. For data transfer in any direction the MOPS data structure [79] is used. A schematic overview of the system consisting of the crate, the workstation and the communication part is given in Fig. 4.3.

It is possible to change some of the parameters controlling the hardware such as base addresses, gains and bunch selector settings. The use of base addresses allows the translation from physical to logical channel addresses, so as to freely choose channels without the need of swapping cables. The receiver gain can be changed from 14 dB to 70 dB in 14 dB steps, each ADC channel gain can be changed from 0 dB to 24 dB in 6 dB steps.

The MOPS data structure which is sent to start the measurement on the crate in one of its objects holds a coded request (1 string and 9 integer numbers) which specifies the measurement parameters: on which BOSC crate to run the measurement, the number of super cycles to be measured, the start time of the measurement in the SPS super cycle, the time between blocks of acquisitions, the number of acquisition blocks, the time between sub-blocks of acquisitions, the number of sub-blocks in one block, the number of turns per sub-block and the channels to be used for the measurement. An example of the usage of some of these parameters can be found in Fig. 4.4. A server program is running on both ends to receive MOPS data structures with measurement requests or acquired data respectively. The data read from the ADC memory and hardware settings like timing information are added to the request MOPS data structure that has been sent from the driving workstation.

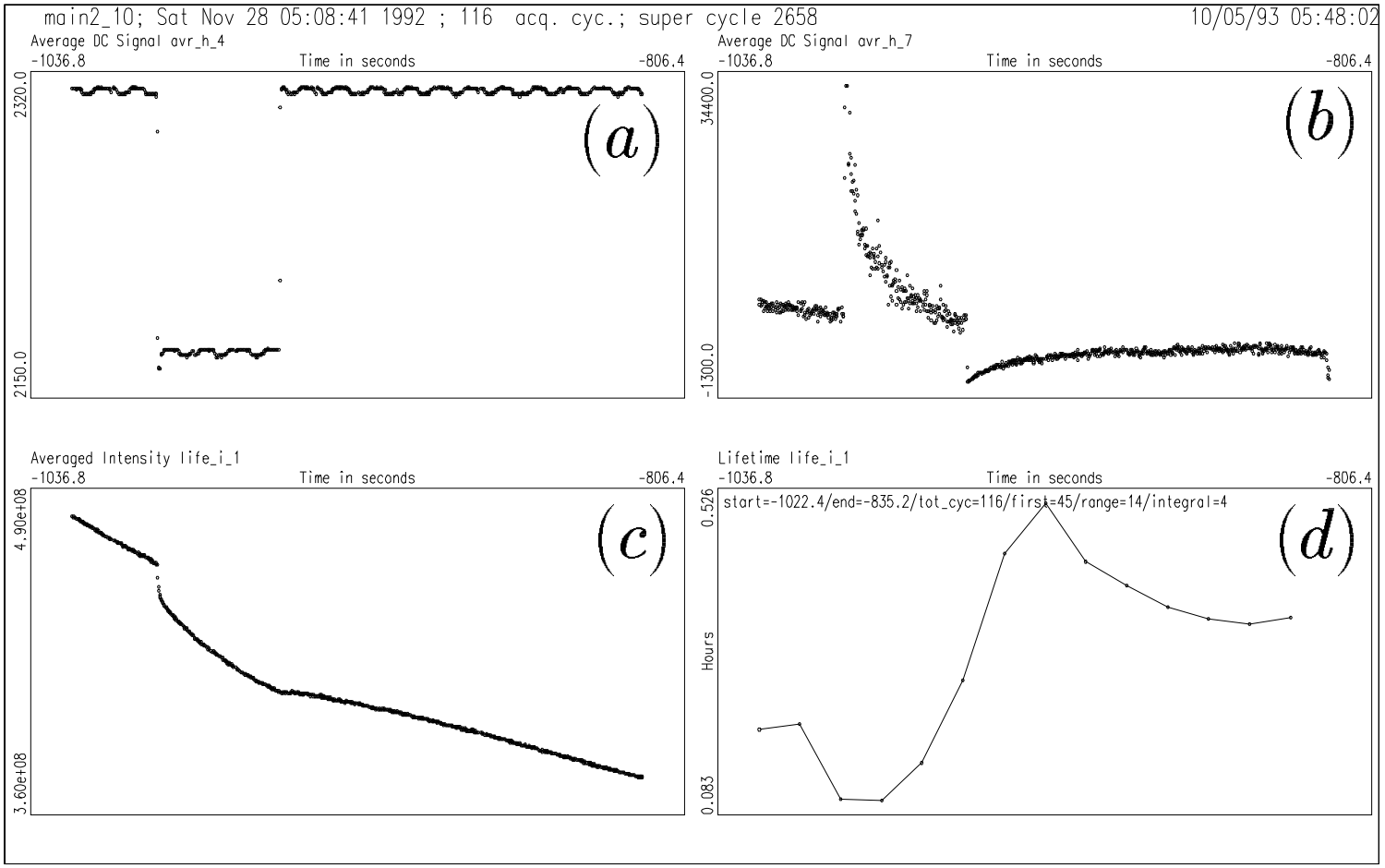

Figure 4.5: Lifetime measurement. The effect of moving a scraper (a) can be seen on the loss monitor (b), the beam intensity (c) and the lifetime (d).

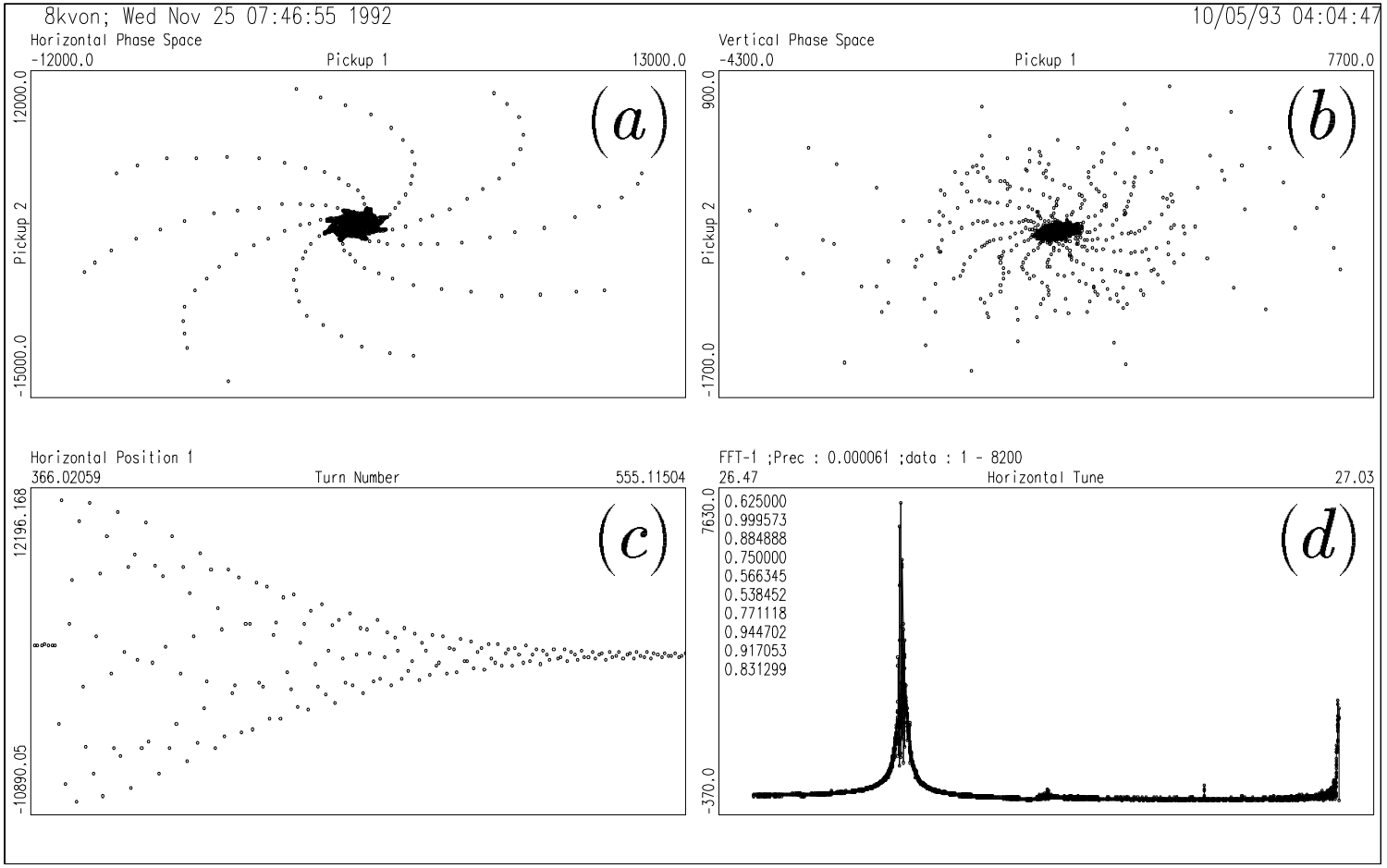

Figure 4.6: Phase space measurement. Motion is depicted close to a horizontal 8^{th} order resonance in the horizontal phase space (a) and the vertical phase space (b). The horizontally kicked and decohered beam can be seen with the position monitor (c) and the horizontal tune spectrum (FFT) is shown in (d).

Application software description
The application software is an interface for starting a measurement, displaying the data acquired, storing data and performing a detailed post-processing analysis. For displaying data the *dataviewer* program [80, 81] is used, the archiving is managed by a catalogue package [82]. BOSC is now used as an operational tool for tune measurements [83] as well as a tool for the dynamic aperture experiments performed at the SPS [84]. Two main types of measurements can be carried out with the latter software:

- Lifetime measurements
- Phase space measurements

In the dynamic aperture experiments effects that influence the particle stability over long periods should be investigated. It was therefore very convenient to utilize BOSC for simultaneous and continuous readings of beam intensity, scraper positions and loss monitor. Different phenomena leading to particle loss can thereby be easily distinguished (see Fig. 4.5).

For a phase space measurement the position signals of one or more pick-ups and the intensity can be recorded. After having applied a kick to the beam the Fast Fourier Transforms from the position signals give the tunes and the line spectra due to resonances. Fig. 4.6 shows how readings of two pick-ups, separated by 90° phase advance (modulo 360°), allows to depict phase space projections. Currently two samples of up to 65000 turns are taken and analyzed online, the repetition rate being 30 s. This allows a precise determination of the tune, but also linear coupling correction, chromaticity compensation and identification of high order resonances.

For phase space measurements there is a tool box which contains four programs. The *fft_mod* program allows to compute the spectra for a selected range of turns. With this facility one can detect changes in the tunes, for instance due to power supply ripple. The *stroboscope* program plots only every n^{th} point in phase space thereby visualizing resonances in the horizontal, vertical and physical phase space projection. The *fake* program has the same functionality as *stroboscope* but uses the information of only one pick-up. In this case the position signal $y(i)$ after i turns is plotted versus the position signal $y(i+n)$ after $i+n$ turns, n being an input parameter. The *smear* program computes the horizontal and vertical decoherence, the decoherence corrected amplitude and the smear [21, 58, 85].

Wire scanners

Since 1984 fast wire scanners have been used in the SPS to measure the transverse emittances [86–88]. A carbon wire of 36 μm thickness, fixed in a turnable fork ("rotational" scanner), passes the beam with a speed of about 6 m/s. These scanners are still available for operation (BA2 Fig. 4.1).

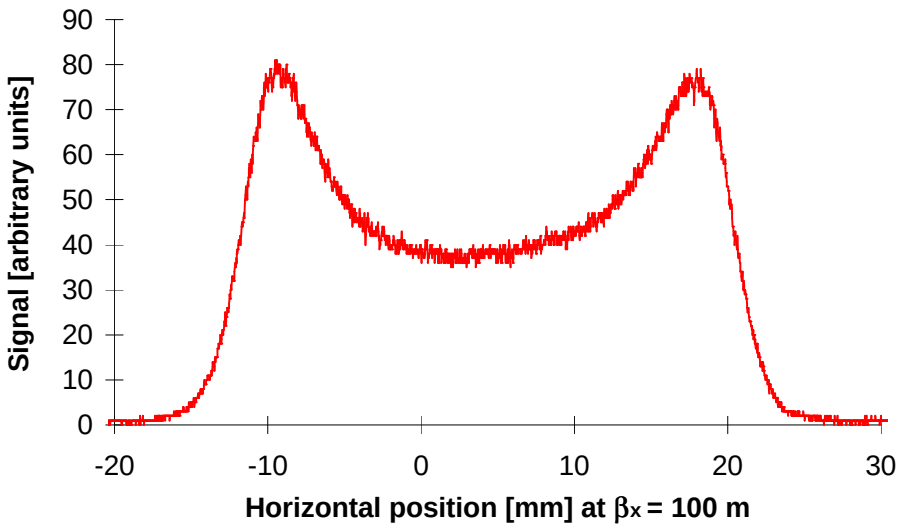

Figure 4.7: Example of a wire scan of the kicked beam.

Later on two "linear" wire scanner units have been installed (in BA2 and BA4, Fig. 4.1) to improve the quality of the measurements. In these scanners the wire is fixed in a shiftable fork moving with a speed of 0.4 m/s. Secondary particle emission caused by the beam hitting the wire can be either observed by scintillators or by measuring the depletion current that replaces lost charges in the wire.

An application software package [89], running on workstations in the control system, allows to trigger the scanner, to set gains (voltage for the photo multiplier or amplification for the depletion current), to choose the timing in the SPS super cycle, to display the scans and fit it with a Gaussian curve and to archive the data. To store the large amount of data collected in the dynamic aperture experiments an extended catalogue was created.

After kicking the beam a typical double peak structure appears in the wire scanner profiles (Fig. 4.7). To test the impact of the wire on the beam many scans have been performed. For the original wire thickness of 36 μm a drop of $2.9 \cdot 10^{-3}$ in the intensity could be observed per scan (Fig. 4.8 (a)). The subtle effects intended to study in this experiment are in the order of this loss. Therefore, it has been decided to replace the 36 μm carbon wires in BA4 with 8 μm wires for both the horizontal and vertical scanners. With such a thin wire the intensity loss per scan is reduced to some $0.7 \cdot 10^{-4}$ per scan (Fig. 4.8 (b)) and no beam blow up can be observed. With the position resolution of the ruler and the sensitivity of the scintillator $5 \cdot 10^7$ protons (10^{-4} of a typical intensity) can be clearly detected at the edge of the beam profile.

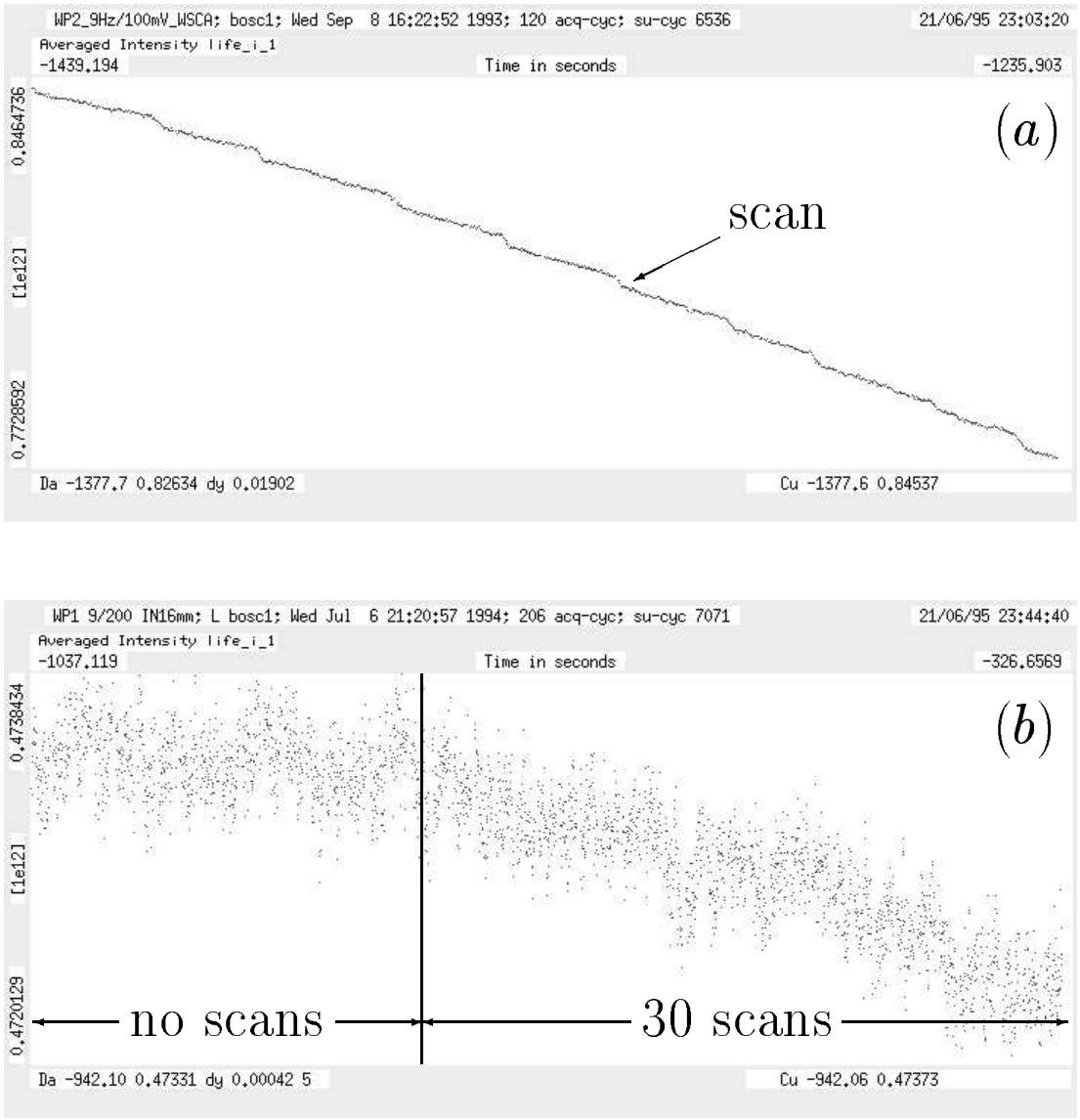

Figure 4.8: Influence of wire scans on the beam intensity. In the upper graph (a) the effect of the thick wire (35 μm) is recorded. At every passage the beam intensity drops by about $2.9 \cdot 10^{-3}$. Scans with the thin wire (8 μm) lead to a much smaller decrease of the beam intensity of some $0.7 \cdot 10^{-4}$ per scan (b).

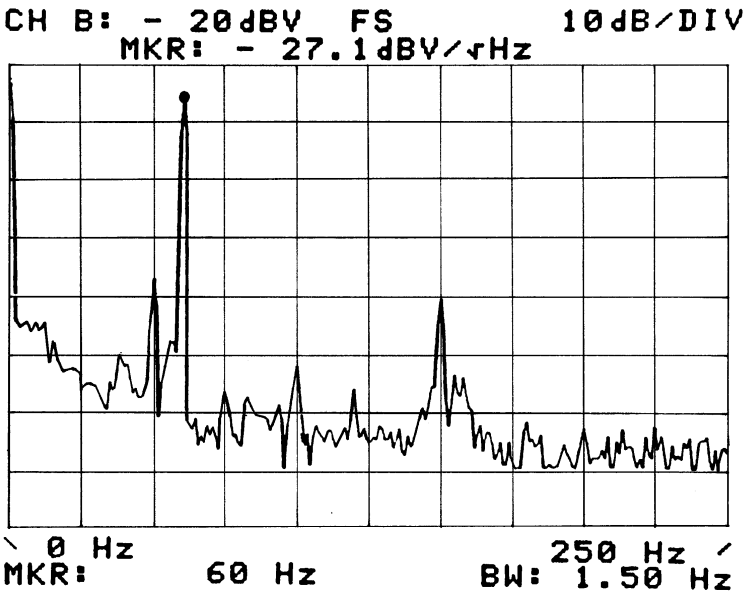

Figure 4.9: Natural tune ripple spectrum. Up to 250 Hz three natural tune ripple lines are above the noise level (50, 100 and 150 Hz) as expected from the voltage power supply ripple. The large 60 Hz line was introduced by the modulating quadrupole and is used for calibration purposes.

4.2.2 Experimental Conditions

The energy of 120 GeV was chosen to have small remanent fields in the SPS magnets, negligible saturation and space charge effects and at the same time a large impact of the nonlinear fields on the particle motion. The 1 σ normalized emittance as given by the preaccelerator chain amounts to some 5 mm $\cdot$ mrad in the horizontal and vertical plane. The intensity was kept below 10^{12} protons to minimize the resistive wall effect. The momentum spread was measured from the longitudinal Schottky signal to be some 10^{-3}. In each experimental session the closed orbit distortions, the linear coupling and the chromaticity were corrected to very small values. The detuning curve was measured and the short-term dynamic aperture evaluated.

This preparation was done in pulsed mode. Every 14.4 s the proton beam was injected into the SPS, accelerated to 120 GeV and kept at this energy for 8 s while the studies could be carried out. The machine was set-up with the RF switched on. Once the strong sextupoles were turned on all systems normally used to counteract collective instabilities could be switched off and the kicker was used to explore different betatron amplitudes.

The long-term studies were performed in a mode with the RF switched off (coasting beam) since RF noise could not be reduced to an acceptable level. With the continuous tune measurement system [75] the natural ripple spectrum was determined and showed 7 major lines that add up to a total modulation depth of $0.5 \cdot 10^{-4}$, which is half the measured total tune ripple depth. All these conditions are summarized in Tab. 4.1.

In Tab. 4.2 the parameter range covered in the experiment is shown. The two working points WP1 and WP2 are depicted in Fig. 4.10 with the detuning due to the nonlinearities (see Sec. 4.2.4). WP1 is close to a horizontal 8^{th} order resonance, WP2 close to a horizontal 5^{th} order resonance. Both resonances are strong but do not define the dynamic aperture. However, a number of 7^{th} order resonances lead to particle loss at both working points.

The additional modulation frequencies (9, 40 and 180 Hz) were chosen for the following reasons: 9 Hz to test the low frequency range, 40 Hz as a frequency close to but different from the main power supply ripple frequency of 50 Hz and 180 Hz as a typical synchrotron frequency. Experiments were also made with combinations of two frequencies. The horizontal tune modulation depth was $0.5 \cdot 10^{-3}, 1.1 \cdot 10^{-3}$ and $1.87 \cdot 10^{-3}$, the larger values being applied at WP1 to obtain loss rates similar to those at WP2. The ratio of horizontal and vertical tune modulation depth was $\Delta Q_x / \Delta Q_z = 1.75$ given by the beta functions at the modulating quadrupole.

The kick strength was varied to probe different betatron amplitudes up to the dynamic aperture. Furthermore the scrapers were used to precisely define the edge of the beam.

4.2.3 Tracking Model

The computer code SIXTRACK [3] is used for the tracking studies. Drift spaces, dipoles and quadrupoles are modeled as thick lenses, all other elements, skew quadrupoles and sextupoles, are approximated by thin lenses. In addition to the 8 strong sextupoles, the 108 chromaticity correction sextupoles are included in the model. The effect of the closed orbit is introduced by shifting the sextupoles by the measured values, the linear coupling is adjusted to the measured one using one family of 6 skew quadrupoles, the chromaticity is corrected to zero. Particles are distributed in betatron amplitude and momentum to probe a sufficient fraction of the phase space. The scraper is used as observation point because the losses are detected at that place in the experiment.

Table 4.1: Fixed beam parameters for the SPS experiment.

RF	short-term on, long-term off
Energy E	120 GeV
1σ normalized emittance	$\approx$ 5mm $\cdot$ mrad hor. and ver.
Momentum spread $\Delta p/p$	$\approx 10^{-3}$
Intensity I (beam current)	$< 10^{12}$ p (7 mA)
Closed orbit rms	$\leq$ 0.3 mm hor. and ver.
Linear coupling	$\mid Q_x - Q_z \mid \leq$ 0.003
Chromaticity $Q' = \Delta Q/(\Delta p/p)$	$\approx$ 1 hor. and ver.
Natural tune ripple lines	50, 100, 150, 300, 350, 500, 600 Hz sum of modulation depth $0.5 \cdot 10^{-4}$
Total natural tune ripple depth	$1.1 \cdot 10^{-4}$

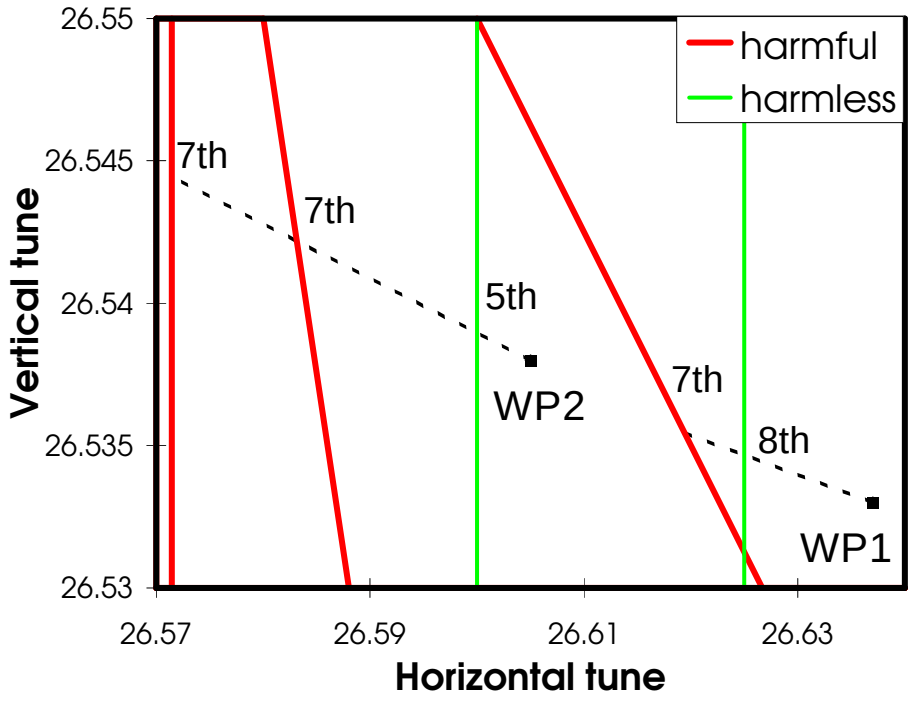

Figure 4.10: The working points WP1 and WP2 in the tune diagram.

4.2.4 Preparatory Measurements

Calibration measurements

All wire scanners (both linear and rotational) were calibrated against each other and their measured beam size was found to agree within 5–10%. Assuming that half of the difference is due to an imprecise knowledge of the beta functions their error is estimated to be less than 10%.

Another important parameter is the kicker strength as this defines the mean amplitude of the particle distribution. The kicker strength was measured as a function of the input voltage (see Sec. 4.2.1) and the absolute calibration was done by using the distance of the

Table 4.2: Studied parameter range for the SPS experiment.

Working points (Q_x, Q_z)	WP1 (26.637, 26.533) WP2 (26.605, 26.538) others
Tune modulation frequencies	9, 40, 180, 9+40, 9+180 Hz
Horizontal tune modulation depth	$0.5 \cdot 10^{-3}$, $1.1 \cdot 10^{-3}$, $1.87 \cdot 10^{-3}$
Kick strength (at $\beta_x = 100$ m)	1.9 – 19.5 mm
Horizontal scraper position	10.8 mm – beam pipe

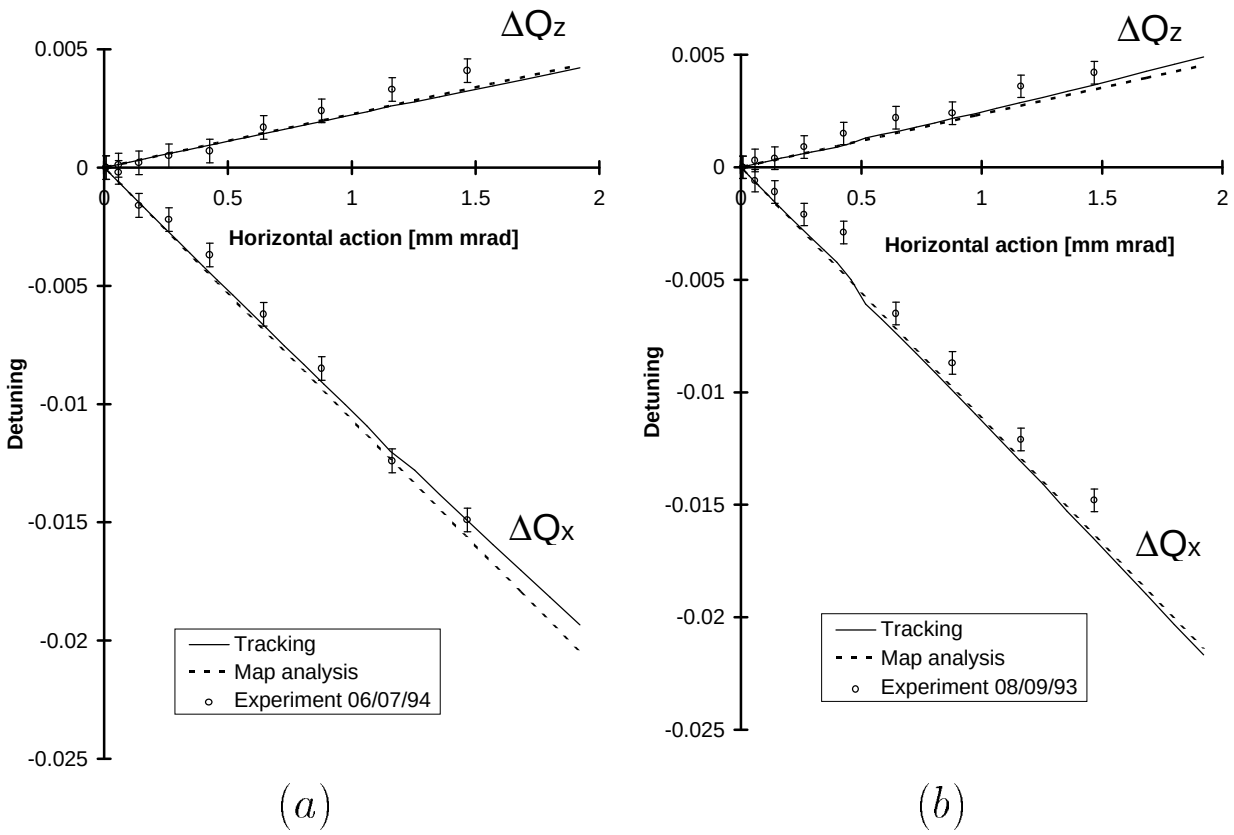

Figure 4.11: Detuning at WP1 (a) and WP2 (b).

two peaks in the profile of a kicked beam (see Appendix A).

Amplitude dependence of betatron tunes

Since the amplitude dependent tune is an important property of any nonlinear oscillator system a disagreement of this quantity between tracking and experiment would cast doubt on the validity of the tracking model.

For the SPS experiment, where sextupoles are the dominant nonlinear elements, equations (2.52) and (2.54, 2.55) hold. In Fig. 4.11 the detuning as a function of action is depicted for the model (from postprocessing tracking data and from a map analysis using normal forms) and the experimental data respectively. As expected from equations (2.54, 2.55) the increase of the detuning with action is linear. The experimental data agree very well with the expectation from the model both in the horizontal and in the vertical plane. Tab. 4.3 summarizes all detuning coefficients, where a and b are taken from the experiment while the term c has only been computed.

Table 4.3: Detuning coefficients at WP1 and WP2.

	a [10^{-3} (mm mrad)$^{-1}$]	b [10^{-3} (mm mrad)$^{-1}$]	c [10^{-3} (mm mrad)$^{-1}$]
WP1	-5.2	1.1	-0.3
WP2	-5.6	1.2	-0.3

4.3 The Scraper Experiment

The detection of slow particle losses in the 1989 experiments was the starting point for an extensive study of particle loss as a function of betatron amplitude, tune modulation depth and tune modulation frequency. Emphasis was put on quantitative results. A very narrow particle distribution in amplitude and momentum would be ideal for such a study. However, one had to face the problem that the particle distribution extended over a wide range of amplitudes.

To partly overcome this problem the experiment was done in the following way: firstly, a single kick of well known strength was applied instead of blowing up the beam with many small kicks. Although the latter choice had considerable operational advantages, the first alternative was chosen because the maximum of the particle distribution was thereby placed at a desired amplitude and the resulting distribution could be estimated analytically (see Appendix A). Secondly, a scraper was used to define a maximum betatron amplitude and, after a subsequent retraction, it acted as the physical aperture. Thirdly, for reasons of reproducibility a complex experimental procedure had to be strictly followed (compare Fig. 4.12): at first the horizontally kicked beam was scraped vertically to remove the vertical beam tail (time T_{-3}, intensity I_{-3}). Then the vertical scraper was retracted, the horizontal scraper was moved in (T_{-2}, I_{-2}) and thereafter the additional tune modulation was switched on (T_{-1}, I_{-1}). Waiting until a stationary particle distribution with an approximately constant loss rate was produced, the horizontal scraper was retracted (T_0, I_0), typically by 1 mm, to create an amplitude region free of particles that was expected to be filled by some transport process. The losses were supposed to stabilize after a time which is denoted by T_{1b} leading to a new stationary particle distribution. T_{1a} was determined from the point of intersection of the linear slope of the intensity with the line $I_0 = const.$ After some 15 min the tune modulation was switched off and the beam was scraped once more vertically (T_2, I_2) and horizontally (T_3, I_3) to determine the plane in which the particle losses took place predominantly.

In the initial set-up, where the beams were heated with many small kicks, the time evolution of the intensity suggested that the loss process could be described by a diffusion model. Considering an action dependent diffusion coefficient $D(I_x)$ the appropriate diffusion equation reads

$$\frac{\partial f(I_x,t)}{\partial t} = \frac{\partial}{\partial I_x}\left(D(I_x)\frac{\partial f(I_x,t)}{\partial I_x}\right). \tag{4.1}$$

Such a diffusion model was also used in a similar scraper experiment under collision

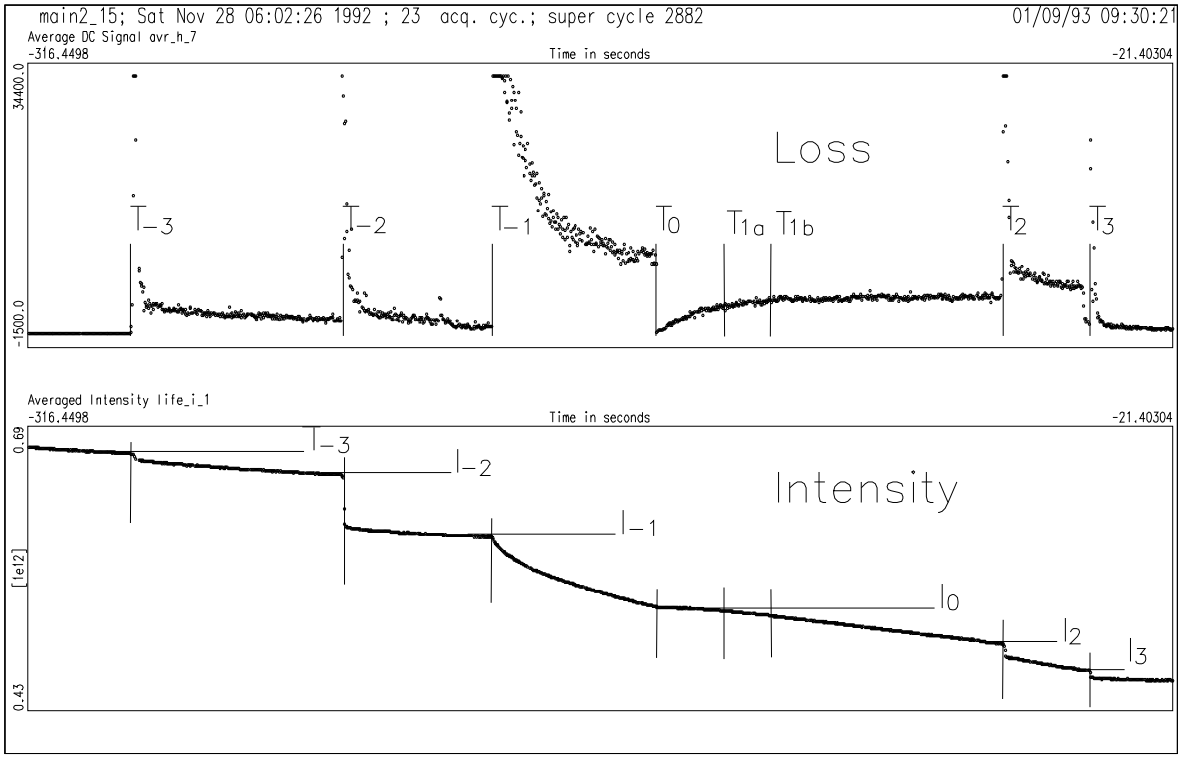

Figure 4.12: Loss rate and beam intensity as a function of time in the scraper experiment. At T_{-3} the beam is scraped vertically to remove the beam tail. At T_{-2} the horizontal scraper is moved in and at T_{-1} the additional tune modulation is switched on. The horizontal scraper is retracted at T_0. T_{1b} is the time after which the loss rates are stabilized and T_{1a} represents the time obtained from the intersection of the linear intensity slope with the line $I_0 = const.$ At T_2 the beam is scraped once more vertically and at T_3 horizontally to test in which of the plane the losses occured predominantly.

conditions at the HERA proton ring [90].

In the experimental period of 1993 the following parameters were varied: at WP1 and WP2 three frequencies (9 Hz, 40 Hz and 180 Hz) and the tune modulation depths $1.1 \cdot 10^{-3}$ and $1.87 \cdot 10^{-3}$ were tested. In addition, at WP1 the tune modulation depth $\Delta Q_x = 0.55 \cdot 10^{-3}$ was studied. Besides this systematic parameter scan the influence of two simultaneously applied modulation frequencies (9+40 Hz and 9+180 Hz) was examined at WP1 and compared to an experimental run at a different working point. A total of 61 experimental runs were recorded (a complete list can be found in Appendix B).

Table 4.4: Experimental stability of particle motion at WP2. L denotes the integrated particle loss after 15 s following the switch-on time of the tune modulation T_0. T_{1a} is determined from the point of intersection of the linear slope of the intensity with the line $I_0 = const$, n is the number of experimental runs with the same modulation frequency and depth. The quoted error is the standard deviation of the mean value. All experimental cases were done with the same kick strength and scraper positions.

	$\Delta Q_x = 0.55 \cdot 10^{-3}$			$\Delta Q_x = 1.1 \cdot 10^{-3}$	
	L [%]	$T_{1a} - T_0$ [s]	n	L [%]	n
9 Hz	5.2 ± 1.1	13.4 ± 5.6	3	5.8 ± 3.3	7
40 Hz	6.4	13.5	1	8.9 ± 4.5	3
180 Hz	6.7 ± 2.4	17.0 ± 7.3	6	12.3 ± 6.9	4

4.3.1 Experimental Results

Intensity measurements

Only results from WP2 will be discussed as in this case all tune modulation depths and frequencies were tested. Tab 4.4 shows the integrated loss L taken 15 s after switching on the tune modulation and the time interval $T_{1a} - T_0$ corresponding to the average transport time between the beam edge and the retracted scraper position. This time interval was the quantity originally measured in the experiment of 1989.

A larger modulation depth leads to a larger loss L but the errors are so large that one can not quantify reliably the difference between the different modulation depths and frequencies. The time $T_{1a} - T_0$ obtained for the smaller modulation depth has similar errors and for the larger depth it was even impossible to determine this value.

These difficulties to obtain quantitative results persisted in spite of a determined effort: the beam observation tools were specially prepared and all instruments were calibrated, the linear machine properties of the SPS were measured and corrected, the nonlinear content of the machine was determined with very good precision and an elaborate measurement procedure was applied. The limiting parameter turned out to be the large transverse beam size which could not be reduced below a certain limit due to operational considerations. The conclusion was that further progress would require a much narrower distribution in betatron amplitude.

Discussion of diffusion models

With the initial set-up of the scraper experiment indications were found that the particle loss may be described by a diffusion process. Assuming a diffsion model a diffusion coefficient in (4.1) must be found that would allow to describe the experimental intensity curves. According to the experimental findings of earlier years any model description of these curves has to include a strong amplitude dependence of the diffusion coefficient (like for instance I_x^m) and an amplitude (I_{x0}) below which only a background mechanism leads to particle loss. For example, rest gas scattering leads to a diffusion coefficient

$D(I_x) = D_0 I_x$ [90]. One therefore arrives at a four-parameter model similar to that used in Ref. [67]:

$$D(I_x) = \begin{cases} D_0 I_x & \text{if } I_x < I_{x0}, \\ D_0 I_x + D_1 (I_x - I_{x0})^m & \text{if } I_{x0} < I_x. \end{cases} \tag{4.2}$$

Firstly a simple approach was tested, namely fitting a diffusion coefficient which increases linearly with action to the experimental data. Unfortunately, this fitting procedure did not converge in all analyzed cases. Due to the discouraging results obtained one had to refrain from a more detailed analysis using the four parameters in Eq. (4.2).

In contradiction to measurements at the HERA proton ring [90], where a diffusion model was successfully employed for the description of particle losses during luminosity runs, the irreproducibility of the experimental results in the SPS experiment prevents a quantitative determination of a diffusion coefficient and a decision if a diffusion model is appropriate to describe the loss mechanism. However, the main source for nonlinearities in the case of HERA was the beam-beam interaction whereas sextupoles are the dominating nonlinear elements in the SPS.

In addition, some interesting qualitative results concerning the so-called "shoulder" could be obtained. This phenomenon, first found in 1989, can be described as follows. After the retraction of the scraper there are only small losses during a certain time interval. Thereafter a very linear decrease of the intensity curve occurs over a long period without any pronounced transition region (within the measurement precision, see Fig. 4.13). In 1993 this effect has been shown to be reproducible given the same experimental conditions as in 1989. In addition, several examples of this behavior were found in 1994 at WP2 (different from the earlier "shoulder" cases). A general precondition seems to be a scraping down to small amplitudes. The observation of a "shoulder" was shown to be in contradiction with a diffusion model [74].

Moreover, detailed tracking studies (Sec. 4.5) seem to indicate that a diffusion model like Eq. (4.2), which is valid over the whole phase phase, does not fit to the phenomenology of the loss processes.

Effect of two modulation frequencies

In 1991 it was observed that the lifetime dropped to about one third when two frequencies (9 Hz and 180 Hz) were applied instead of only one (9 Hz) when the same total tune modulation depth was kept. The same procedure was tested in 1993 at another working point (see Fig. 4.14 (*a*), WP1) and for comparison the experiment at the original working point was repeated (Fig. 4.14 (*b*)), confirming the previous result. The interesting observation is that the effect of two frequencies in case (*a*) is less pronounced than in case (*b*).

The effect of two modulation frequencies can be understood qualitatively as follows [9]. With only one modulation frequency the resonance condition reads

$$kQ_x + lQ_z + m\frac{f_{mod}}{f_{rev}} = p, \tag{4.3}$$

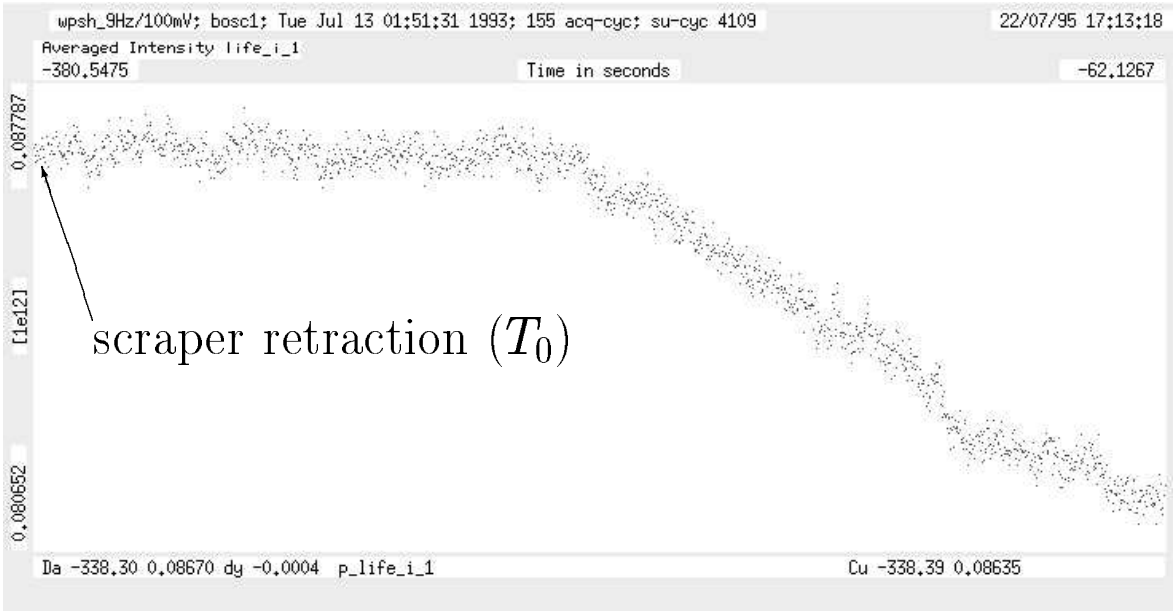

Figure 4.13: The "shoulder". After retracting the scraper the intensity stays constant at first and then decreases linearly in time without a pronounced transition region.

f_{mod} being the modulation frequency and f_{rev} the revolution frequency, i.e. resonance sidebands are created around the main resonance $kQ_x + lQ_z = p$. For high modulation frequencies the sidebands have a large spacing; for low frequencies the spacing is small and the sidebands may overlap so that particles can be transported over wide amplitude regions. With two modulation frequencies the resonance condition is

$$kQ_x + lQ_z + m\frac{f_{mod1}}{f_{rev}} + n\frac{f_{mod2}}{f_{rev}} = p. \tag{4.4}$$

Having a high and a low modulation frequency (in this case $f_{mod1} = 180$ Hz and $f_{mod2} = 9$ Hz) the high frequency f_{mod1} leads to widely spaced sidebands $kQ_x + lQ_z + m\frac{f_{mod1}}{f_{rev}} = p$ around the main resonance. Around those principal sidebands additional sidebands due to the low frequency f_{mod2} are created which can overlap.

Now the different behavior of the two working points can be explained. In Fig. 4.15 the working points for both cases are shown together with the detuning lines (dotted) up to the dynamic aperture. In case (a) the dynamic aperture is close to a 7^{th} order resonance, in case (b) it is close to a 5^{th} order resonance. Only the first order resonance sidebands due to the higher frequency (180 Hz) are depicted which are by far the strongest sidebands for the chosen modulation depth and frequency (compare Eq. (2.75)). One of the sidebands at each working point can reach the particle distribution.

From tracking data the resonance driving term of the 5^{th} order resonance in case (b) was found to be about a factor 500 larger than the driving term of the 7^{th} order res-

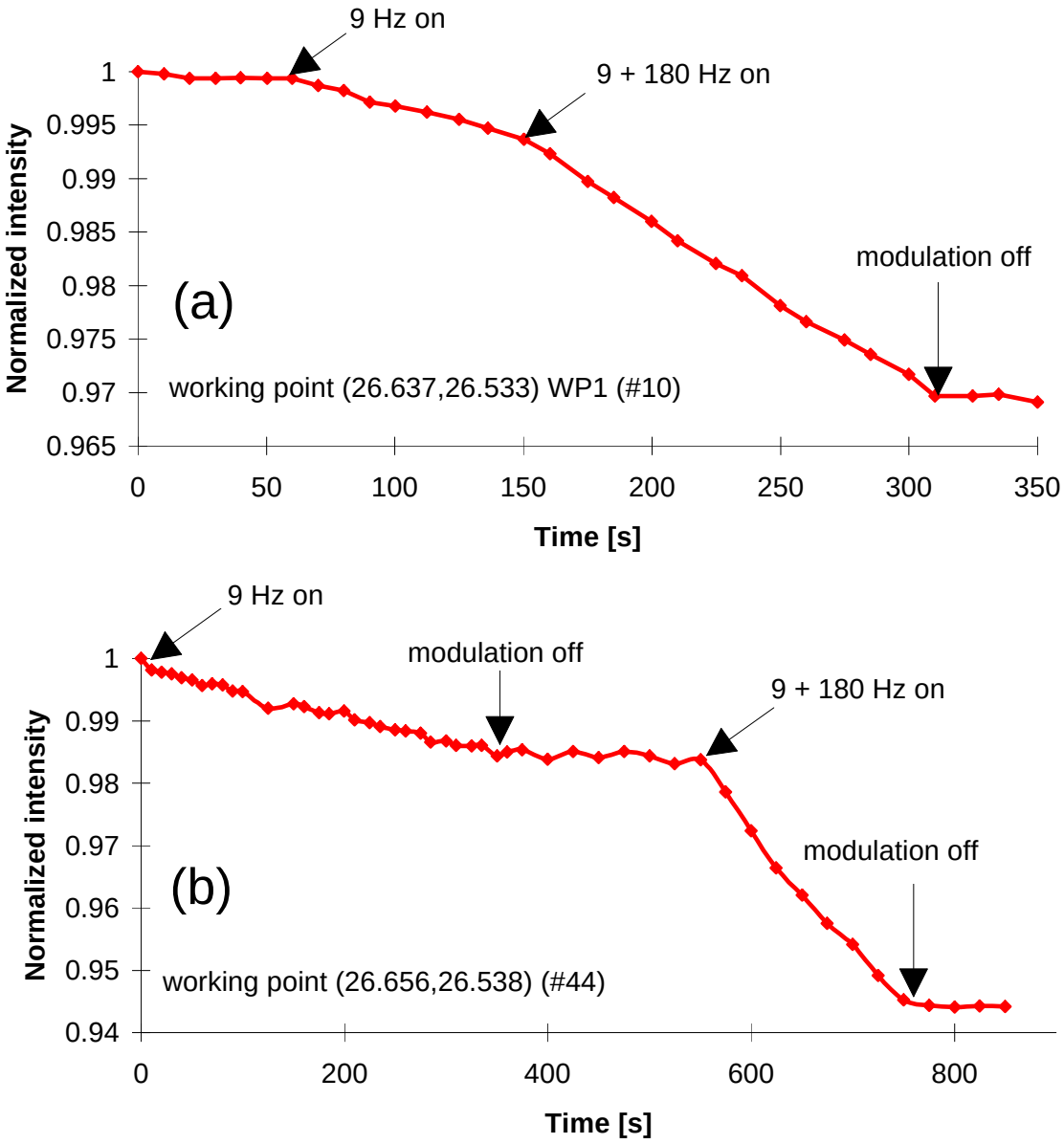

Figure 4.14: Beam intensity versus time for one and two modulation frequencies at two different working points. Different from case (*a*), case (*b*) shows a significant difference between one and two modulation frequencies.

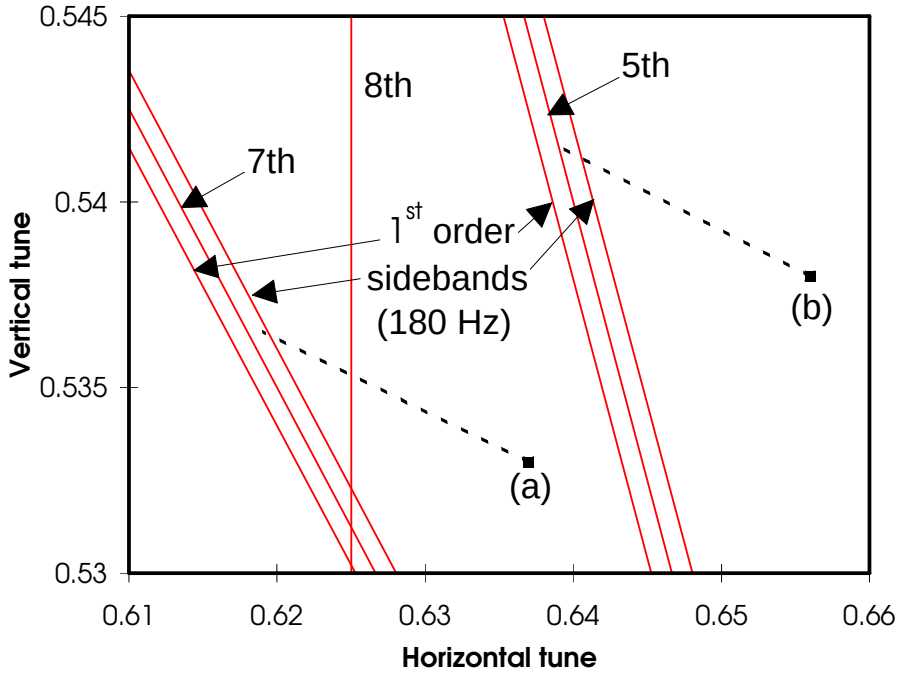

Figure 4.15: Tune diagram for the cases where two modulation frequencies were applied simultaneously. The chosen working points are denoted by (a) and (b), the dotted lines indicate the detuning curve up to the dynamic aperture. Shown are the relevant sum resonances and their first order sidebands due to the larger modulation frequency (180Hz).

onance in case (a). One can therefore expect that the island sizes (which are given by equations (2.69, 2.70)) of the resonance sidebands around the first order 180 Hz sidebands in case (b) are much larger than those in case (a). As a consequence more of these sidebands can overlap and the amplitude region of overlapped sidebands is larger leading to a stronger particle loss in case (b).

4.3.2 Intensity Curves Obtained from Numerical Simulations

Computer simulations were carried out [91] that aimed at reproducing the experimentally obtained intensity curves for the different modulation frequencies and depths. These simulations were restricted to WP2 as sizable particle losses were found at this working point prior to 10^6 turns in the amplitude region of interest.

Method of simulation

The experimental particle distribution extended over a wide amplitude region. Therefore, reasonable agreement with simulations could only be expected when this distribution was considered in some ways. Due to the limited computing power and the long time interval

to be studied, the beam could only be represented by a small number of particles which was chosen to be 180. They are called "superparticles" because each of them should represent a certain range in horizontal betatron amplitude r and momentum deviation $\eta = \Delta p/p$. The vertical distribution is treated only approximately. To each "superparticle" an intensity weight is assigned according to its initial position in the measured particle distribution $f(r, \eta)$. The simulated time-dependent intensity is derived by subtracting from the initial intensity the weight of a "superparticle" when it is lost.

In the tracking the particles were started at a location where the dispersion is small. Therefore one may factorize the distribution $f(r, \eta)$ as $f_r(r) f_\eta(\eta)$. For the horizontal betatron distribution $f_r(r)$ a Gaussian distribution with standard deviation σ was assumed which was justified by wire scan profiles. After a kick k this leads to a distribution (see Appendix A)

$$f_r(r) = \frac{r}{\sigma^2} \exp\left\{-\frac{k^2 + r^2}{2\sigma^2}\right\} \mathrm{I}_0\left(\frac{kr}{\sigma^2}\right), \tag{4.5}$$

where nonlinear phase space distortion have been neglected. I_0 is the modified Bessel function of first kind and order zero. The distribution $f_\eta(\eta)$ of the momentum deviation $\eta = \Delta p/p$ is conveniently represented by

$$f_\eta(\eta) = \frac{2}{\pi} \cos^2\left(\frac{\pi}{2} \frac{\eta}{\eta_{max}}\right). \tag{4.6}$$

To verify the validity of Eq. (4.5), the tune curve $Q_x(r)$ (compare Fig. 4.11 (b)) was multiplied with the distribution $f_r(r)$ after a kick (σ being obtained from a fit to a wire scan profile before the kick and k derived from the calibrated kick strength) and the result was compared with the horizontal tune distribution obtained from the transverse Schottky signal (see Fig. 4.16 (a)). The overall agreement is satisfactory with the exception of a peak, which is due to the collective movement of particles in the 5^{th} order resonance islands. Furthermore, at smaller tunes (left-hand side of Fig. 4.16 (a)), corresponding to large horizontal betatron amplitudes, the experimental Schottky signal is reduced compared to the model since in the accelerator particles were already lost at those amplitudes. The momentum distribution $f_\eta(\eta)$ as depicted in Fig. 4.16 (b) agrees with the longitudinal Schottky signal.

The "superparticles" were started with initial conditions (r_m, η_n) with $m = 0, 1, ..., 35$ and $n = -2, -1, ..., 2$ and the assigned weights were computed as

$$w_{mn} = \int_{r_1}^{r_2} f_r(r)\, \mathrm{d}r \int_{\eta_1}^{\eta_2} f_\eta(\eta)\, \mathrm{d}\eta. \tag{4.7}$$

The numbers $(r_1, r_2, \eta_1, \eta_2)$ are defined below. To obtain a better resolution close to the beam edge the step size in amplitude was reduced in this region and the integration borders for r in (4.7) are computed as

$$r_1 = \begin{cases} 0 & \text{if } m = 0, \\ \frac{1}{2}(r_{m-1} + r_m) & \text{if } m > 0, \end{cases} \qquad r_2 = \begin{cases} \frac{1}{2}(r_m + r_{m+1}) & \text{if } m < 35, \\ r_{max} & \text{if } m = 35. \end{cases} \tag{4.8}$$

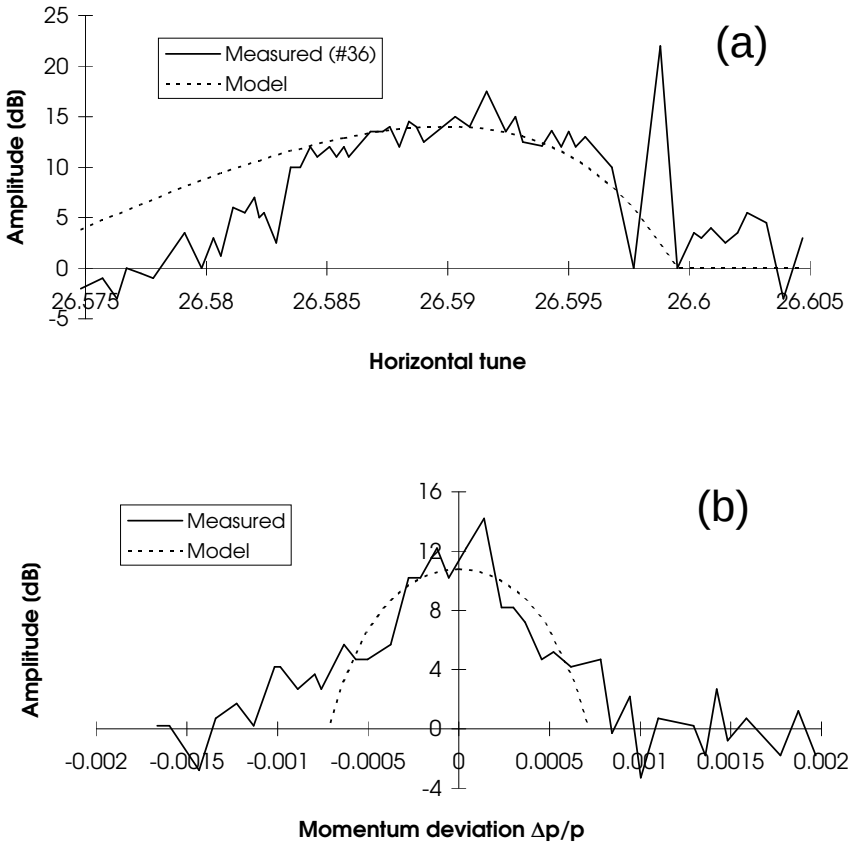

Figure 4.16: Comparison between measured and theoretical distribution functions. In part (a) the measured tune distribution (solid line) is shown together with the theoretical one (dashed line). The amplitude is plotted in logarithmic scale. In part (b) the measured and assumed momentum distribution is depicted. Both measurements were performed with the Schottky system.

where r_{max} is given by the scraper position. For the momentum distribution a constant step size $\Delta\eta = 2.5 \cdot 10^{-4}$ was chosen and the integration borders for η were

$$\eta_1 = \begin{cases} -\eta_{max} & \text{if } n = -2, \\ \left(n - \frac{1}{2}\right)\Delta\eta & \text{if } n > -2, \end{cases} \qquad \eta_2 = \begin{cases} \left(n + \frac{1}{2}\right)\Delta\eta & \text{if } n < 2, \\ \eta_{max} & \text{if } n = 2. \end{cases} \tag{4.9}$$

In the tracking the three relevant time intervals $[T_{-2}, T_{-1}]$, $[T_{-1}, T_0]$ and $[T_0, T_1]$ were treated separately. The complete intensity curve was then computed by properly matching the three time intervals.

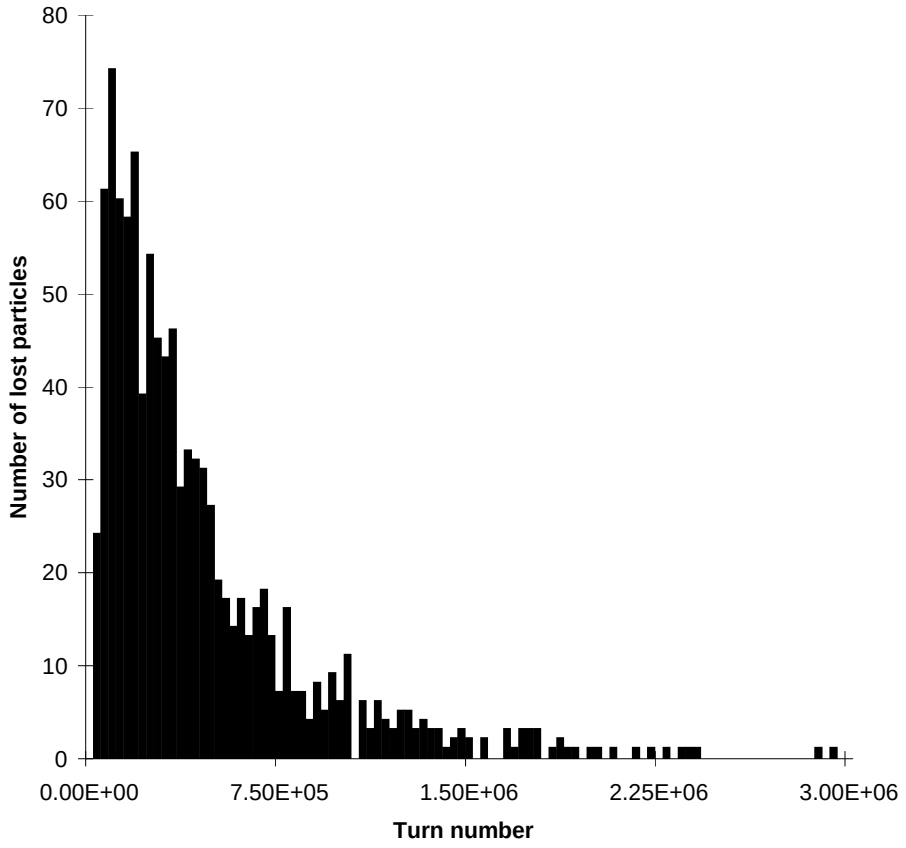

Figure 4.17: Distribution of survival times of a sample of 640 particles initially placed in a small region of phase space [11]. Working point WP1 was used with a horizontal start amplitude of 16.0 mm (at $\beta_x = 100$ m) and a tune modulation of 40 Hz and $\Delta Q_x = 1.1 \cdot 10^{-3}$.

Error estimates

There are various types of errors. The first comes from the lack of statistics since only 180 weighted particles are tracked. The individual survival time of those "superparticles" may be very different from the average survival time in the chaotic regime. To study this in more detail 640 particles were started in a very small phase space region. Their loss time distribution is shown in Fig. 4.17. The maximum loss is reached after a short time followed by a very long tail with an almost exponential decrease.

Furthermore a number of experimental values are used as input for the simulation. To estimate the effect of the measurement errors of these values on the simulated intensity curves the input parameters are varied by their uncertainty (typically 5%). The results are listed in Tab. 4.5. The total error is given as the square root of the sum of squares of the individual errors (last row in Tab. 4.5).

Table 4.5: Error estimation for the intensity drop in the interval $[T_{-1}, T_0]$ by varying parameters.

ΔQ_x	$0.55 \cdot 10^{-3}$	$1.1 \cdot 10^{-3}$
emittance ϵ	+3%/−6%	+3%/−6%
momentum width η_{max}	+1%/−3%	+2%/−5%
kick strength a	+6%/−6%	+10%/−10%
scraper position	+3%/−12%	+3%/−11%
total	+8%/−14%	+12%/−17%

Results

Six cases have been studied: two modulation depths ($\Delta Q_x = 5.5 \cdot 10^{-4}, 1.1 \cdot 10^{-3}$) and three modulation frequencies (9 Hz, 40 Hz, 180 Hz). Two examples are shown in Fig. 4.18. The simulated normalized intensity curve is depicted together with an experimental run.

Besides the above stated statistical error there is clearly a systematic underestimation of the losses and loss rates for all six tracking cases. As an example the experimental intensities in the two cases shown in Fig. 4.18 at T_1 are lower compared to the simulations by 15% and 22% in part (a) and (b) respectively. One has to conclude that even though all qualitative features of the experimental intensity curves appear in the simulated curves, this method is unable to predict loss rates or beam lifetimes with reasonable accuracy.

4.4 The Wire Scanner Experiment

Besides employing the scrapers, which are by nature destructive, as a beam observation tool, there is also the possibility in the SPS to use the almost nondestructive scanner system with the 8 μm flying wires (see Sec. 4.2.1) for the dynamic aperture studies. In these investigations the beam profile is the object of study. The wire scanner profiles are the projections of the particle distribution in phase space onto the $x-$ and $z-$axis respectively and their time evolution allows a deeper insight into particle loss mechanisms. In particular the time dependent half base width of those profiles can be directly compared with survival plots obtained from simulations. It has to be mentioned that the scrapers were still needed as an experimental tool: firstly they allow a definition of the beam edge and secondly, once taken out to a larger amplitude, they serve as a known physical aperture limiter.

Taking advantage of the experience from the scraper experiment, which showed that the variation of the modulation frequency had hardly any effect on the loss rates, this new set of studies was restricted to a single modulation frequency of 9 Hz. The influence of the modulation depth on the particle stability was much more pronounced and for both working points a modulation depth was used which caused well detectable particle losses (i.e. $\Delta Q_x = 1.87 \cdot 10^{-3}$ at WP1 and $\Delta Q_x = 0.55 \cdot 10^{-3}$ at WP2 respectively).

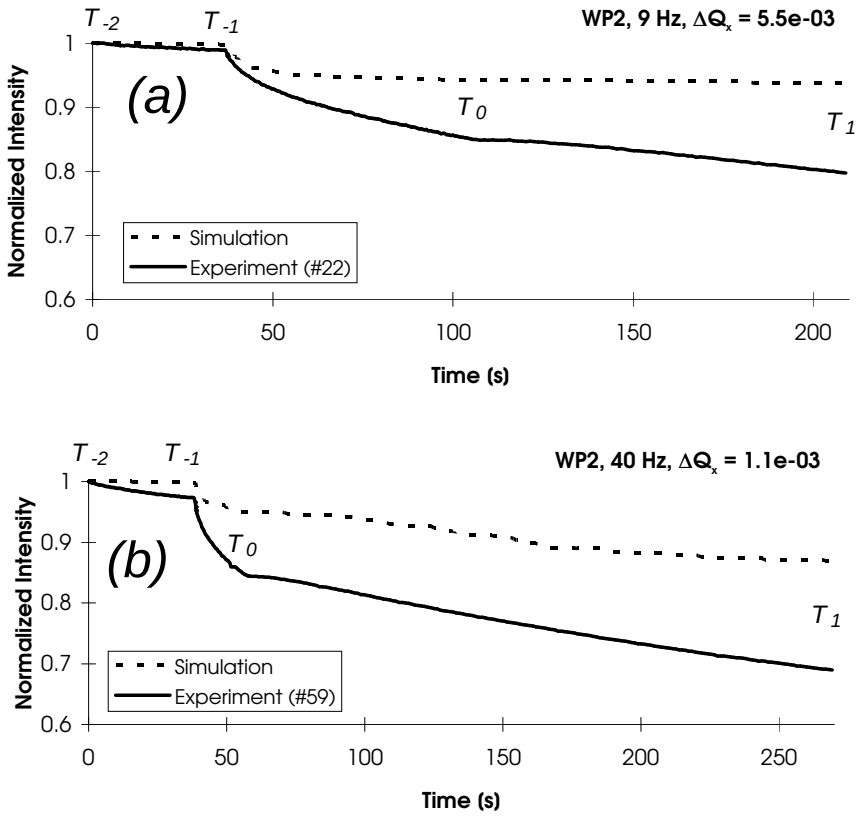

Figure 4.18: Measured and computed intensity curves at working point WP2 with a tune modulation of 9 Hz and $\Delta Q_x = 0.55 \cdot 10^{-3}$ (a) and a tune modulation of 40 Hz and $\Delta Q_x = 1.1 \cdot 10^{-3}$ (b). Note thate the origin of the intensity scale is suppressed.

4.4.1 Beam Profile Measurements

For this set of experiments the following procedure was used: firstly the horizontally kicked beam was freed from vertical beam tails using a vertical scraper. Then the beam was scraped horizontally by moving the scraper to an *inner* position. Thereafter this scraper was retracted to an *outer* position to study the processes leading to particle losses in between those two scraper positions. After this scraping procedure the tune modulation was switched on and horizontal beam profiles were recorded about every minute for typically 15 minutes. Fig. 4.19 shows the first and last scan of such a run.

Two different set-ups were used: firstly, the *inner* scraper position was held constant and the *outer* position was varied for different experimental runs (this situation will be referred to as the fist set-up in the following section) and secondly, the *inner* position was varied and the *outer* position was kept constant (this will be referred to as the second set-up).

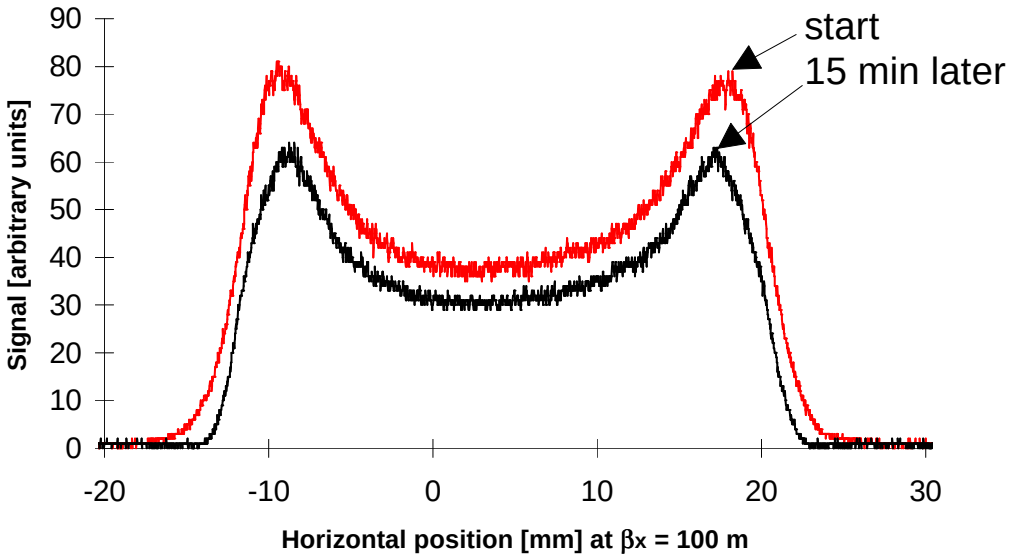

Figure 4.19: Time evolution of a beam profile after a horizontal kick. Shown are two profiles obtained with the horizontal wire scanner (8 μm wire) 15 min apart for a beam under the influence of additional tune modulation of 9 Hz and $\Delta Q_x = 1.87 \cdot 10^{-3}$ at WP1 (#78). In this case the beam was not scraped horizontally.

First working point - WP1

Part (a) and (b) of Fig. 4.20 show the half beam width and the normalized intensity of the first set-up with the constant *inner* scraper position (18 mm) while (c) and (d) were obtained with a constant *outer* position (26 mm). Moreover, there is one horizontally unscraped run denoted by #78. In each set-up there is one case, #62 and #76 respectively, with almost identical conditions. This may serve as a reference to compare the two situations. In the first set-up particle transport phenomena above 18 mm are studied while in the second set-up amplitudes below 18 mm are investigated. In all legends the values given in millimeters are the differences between the *inner* and the *outer* scraper position normalized to $\beta_x = 100$ m. An estimate of the measurement precision is attached to the cases #64 and #77. The band borders that are visible in part (c) will be discussed in Sec. 4.5.

In the first set-up (Fig. 4.20 (a)) the beam width remains constant for all cases after a slight drop over the first 100 s. The normalized intensity (part (b)) evolves also rather similarly in all cases leading to a difference of not more than 2% after a period of 650 s. One can conclude that in this set-up the growth of the betatron amplitudes is too fast to lead to any sizeable differences between the tested scraper positions.

In the second set-up (Fig. 4.20 (c)), considering the first 150 s, the beam width is strongly reduced for the unscraped run (#78), it stays almost constant for the intermediate

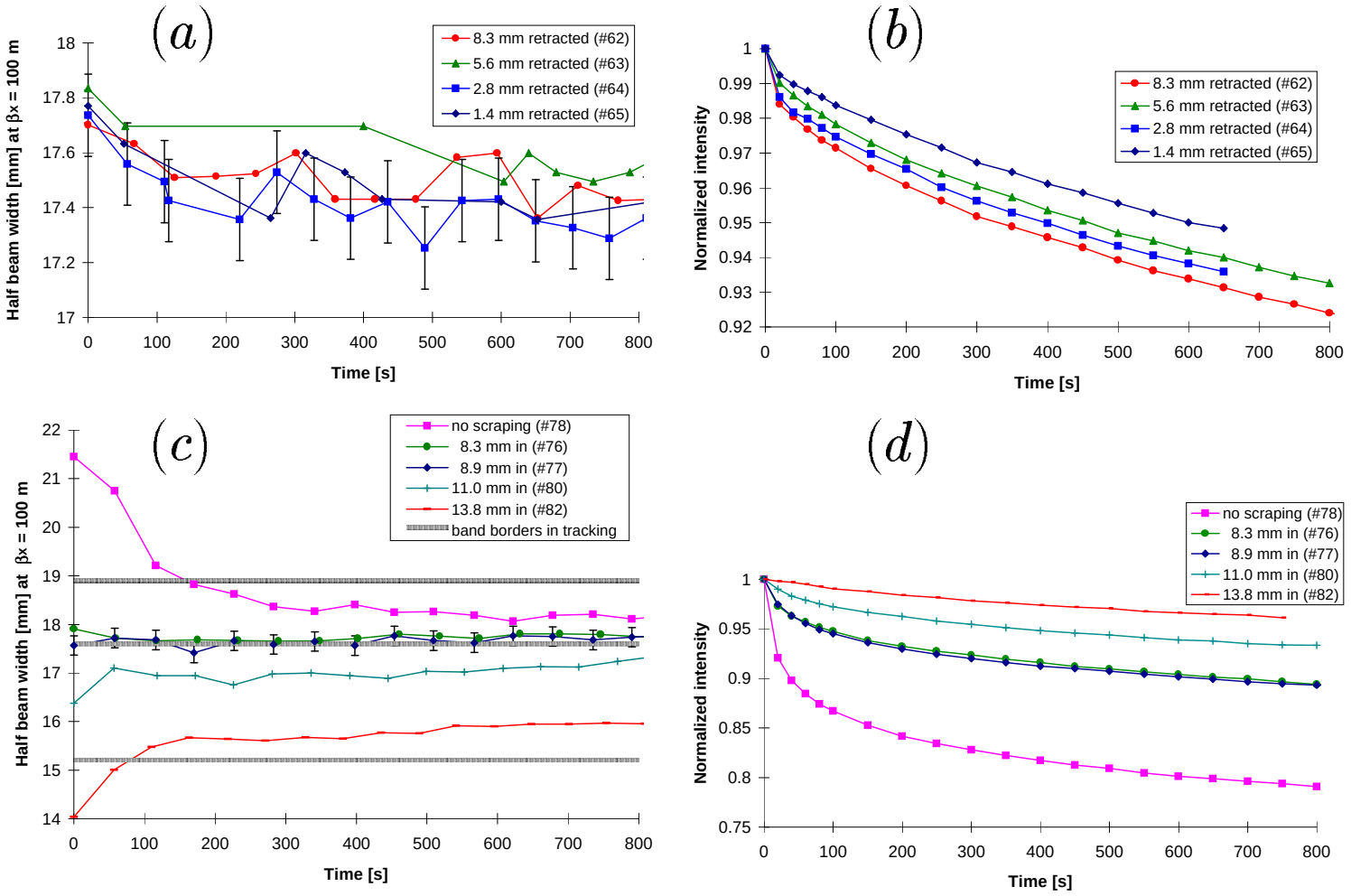

Figure 4.20: Wire scanner measurements at WP1. In (*a*) and (*b*) the half beam width and normalized intensity are shown for a fixed *inner* scraper position of 18 mm and different retraction values. In (*c*) and (*d*) the *inner* scraper position was varied and the *outer* position was kept fixed at 26 mm. The quoted numbers in the labels are the distance between the initial *inner* and the final *outer* scraper position. The band borders in part (*c*) are explained in Sec. 4.5.

cases (#76, #77, #80) and it increases appreciably for the low amplitude run (#82). Disregarding the first 150 s the half beam widths change slowly over a long period of 600 s. In the cases at larger amplitudes this width is slightly decreasing and at lower amplitudes it is slightly increasing. After 800 s four cases almost merge at the same amplitude while the width in the lowest amplitude case is still somewhat smaller but seems to slowly approach this value as well. The normalized intensity varies strongly for the first 150 s but thereafter the lifetime is approximately the same in all cases.

Second working point - WP2

At the second working point the two set-ups are similar to those of working point WP1. However, the *inner* scraper position in the first set-up (larger amplitude regime) is slightly larger (19 mm). Part (*a*) and (*b*) represent again the regime of large amplitudes while (*c*) and (*d*) show the second set-up (lower amplitude regime). The runs #66 and #83 are the reference cases for WP2 and therefore made under similar conditions.

In the first set-up all cases have a very similar behavior concerning half beam width and normalized intensity. Compared to the first working point the motion seems, however, considerably more unstable resulting in a decreasing width of the beam over at least the first 600 s. Note also that at this working point a four times smaller tune modulation depth was applied.

In the second set-up the half beam widths also seem to tend to the same value after 800 s, however, the merging process is less pronounced than that of WP1. The normalized intensities (part (*d*)) have not reached a regime of stabilized lifetimes as it was the case at WP1.

4.4.2 Dynamic Aperture

In Sec. 2.11 the problems defining the dynamic aperture were mentioned. The SPS experiment was rather restricted by the large natural beam size. This precludes any fine exploration of the phase space as it is done in tracking by varying the amplitude in small steps. In particular small chaotic regions within an otherwise stable region can not be detected. However, the maximum amplitude above which no particles survive after a certain time is a measurable quantity and serves as the dynamic aperture definition in this experiment.

Another limitation in the aperture studies was the fact that the full time interval of interest (15 min storage time or 40 million turns in the SPS, comparable to the LHC injection time) could not be fully explored with tracking simulations, only one third (345 s) could be reached with reasonable computing effort.

Measurements

Experimentally, the dynamic aperture is determined by using the maximum base width of the wire scan profiles (Fig. 4.19). In Fig. 4.22 (*a*) four wire scan measurements at WP1 with additional tune modulation are displayed. These curves were smoothed and

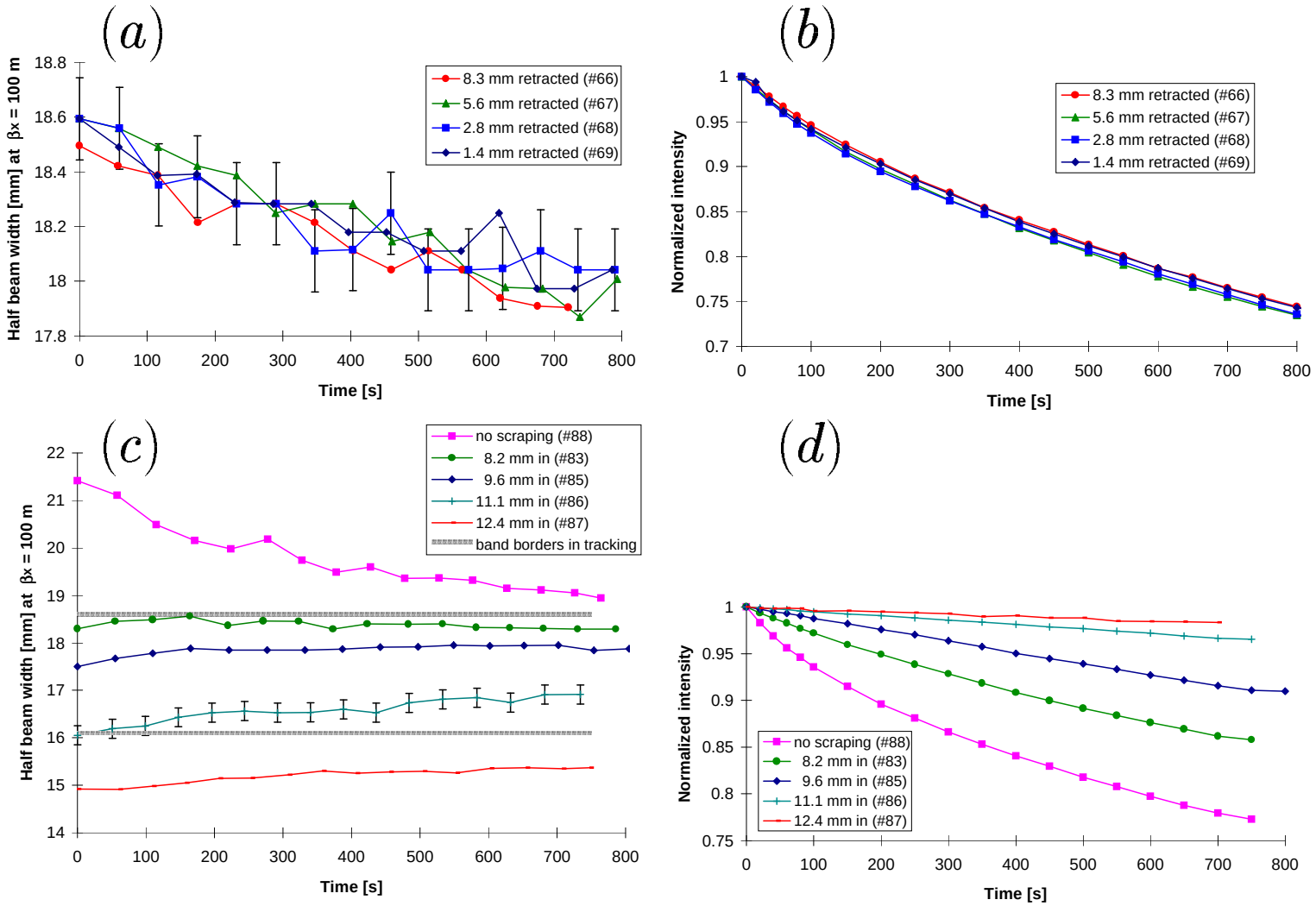

Figure 4.21: Wire scanner measurements at WP2. In (*a*) and (*b*) the half beam width and normalized intensity are shown for a fixed *inner* scraper position of 19 mm and different retraction values. In (*c*) and (*d*) the *inner* scraper position was varied and the *outer* position was kept fixed at 26 mm. The quoted numbers in the labels are the distance between the initial *inner* and the final *outer* scraper position. The band borders in part (*c*) are explained in Sec. 4.5.

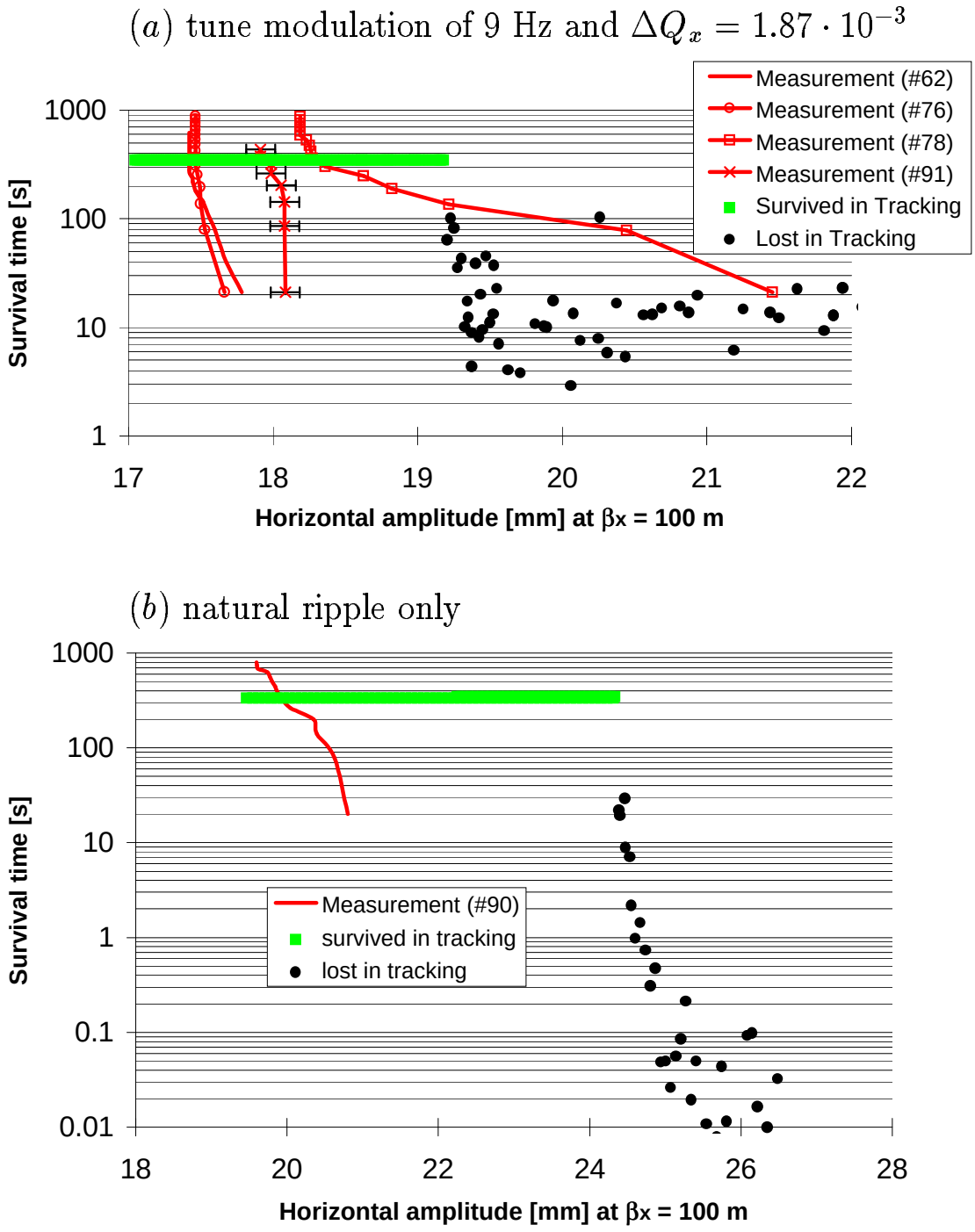

Figure 4.22: SPS dynamic aperture studies at WP1. Measurement and computational results for the dynamic aperture with and without additional tune ripple is shown in part (a) and (b) respectively.

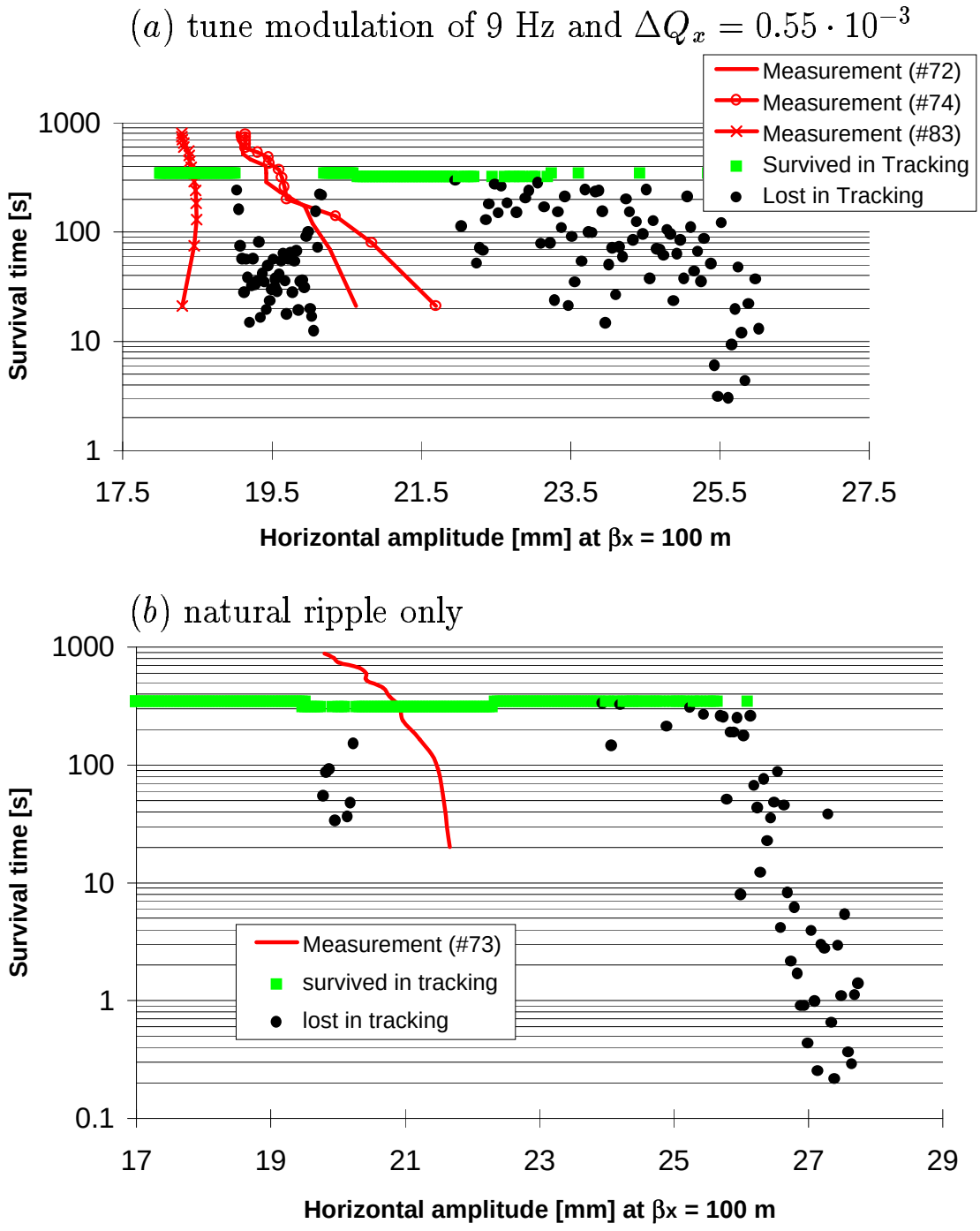

Figure 4.23: SPS dynamic aperture studies at WP2. Measurement and computational results for the dynamic aperture with and without additional tune ripple is shown in part (a) and (b) respectively.

Table 4.6: Comparison of measured and computed dynamic aperture in the SPS experiment. All values are given for $\beta_x = 100$ m. For the onset of chaos there are two values: the larger one is the border above which no regular particles could be found, the lower (in brackets) is the lowest amplitude at which large scale chaotic motion sets in. The measured dynamic aperture and the loss border are both determined after 345 s.

case	measured dynamic aperture $a_{x,meas}$ [mm]	onset of chaos in tracking ($2 \cdot 10^5$ turns) $a_{x,chaotic}$ [mm]	loss border in tracking ($1.5 \cdot 10^7$ turns) $a_{x,loss}$ [mm]	relative difference between measurement and loss border $\left(\frac{a_{x,loss}}{a_{x,meas}} - 1\right)$ [%]
WP1, 9 Hz, $\Delta Q_x = 1.87 \cdot 10^{-3}$	17.4	(7.7) 14.3	19.2	10
WP2, 9 Hz, $\Delta Q_x = 0.55 \cdot 10^{-3}$	19.5	(7.4) 8.3	22.3	14
WP1, natural ripple only	20.0	(15.7) 23.1	24.4	22
WP2, natural ripple only	20.9	(9.8) 23.6	25.7	23

the estimated error bars are shown in case #91. The reproducibility of the experimental results was found to be within 2% for two measurements under the same conditions but 5 months apart (#62 and #76). Due to the rather large beam size the results depend on the measurement procedure: cases #62 and #76 were scraped horizontally after kicking, whereas cases #78 and #91 were left unscraped and in addition the latter case was kept for some extra 15 min without additional tune modulation. Initially one observes a significant difference which, however, reduces to only 5% after 345 s.

Fig. 4.23 (a) shows the situation for WP2 where the applied ripple depth was about 4 times smaller. For two cases (#72 and #74) the beam was not scraped, case #83, for which the beam was scraped horizontally, shows the interesting feature that the beam size grows first and then shrinks again. Also at WP2 the differences of the various cases after 345 s are reduced to less than 3%.

Finally figures 4.22 (b) and 4.23 (b) show the experimental results with natural tune ripple only. The results of all measured cases are summarized in Tab. 4.6.

Computations

As described in Sec. 3.4 survival plots are used to determine the dynamic aperture. According to the experimental conditions the particles are tracked with large horizontal displacements while a vertical displacement of roughly one σ of the vertical beam size is considered.

In this experiment, where relatively large tune modulation is present, the onset of chaos is a much too pessimistic indicator for the long-term stability. In all tracked cases a wide amplitude range could be found (column three in Tab. 4.6) where chaotic (after 200 000 turns) and regular regions alternate. For each chaotic region in that amplitude

range a particular sum resonance is found which apparently causes the unstable behavior. At WP1 the lost particles correspond to a coupled 7^{th} order resonance (Fig. 4.22 (a)) or to a horizontal 13^{th} order resonance (Fig.. 4.22 (b)). At WP2 (Figs. 4.23 (a) and (b)) the losses at large amplitudes correspond to a horizontal 7^{th} order resonance and the losses at about 20 mm are due to another coupled 7^{th} order resonance. These resonances can be found in Fig. 4.10.

Comparison

The computed dynamic aperture is shown in column four in Tab. 4.6. The last column in this table shows the relative difference in percent between computed and measured dynamic aperture, both determined after 345 s. In the cases with additional tune modulation the relative difference is about 10% but without ripple this number rises to more than 20%. Moreover in the tracking one finds a broad region of apparently regular motion outside the experimental stability border which not present in the cases with additional tune modulation. From this one has to conclude that an essential destabilizing effect is missing in the tracking model. A rough estimate for the magnitude of this effect is given by the strength of additional tune modulation because the experimental dynamic aperture without extra tune modulation agrees well with that of the tracking when this ripple is introduced (compare the last two entries in column two with the first two entries in column four of Tab. 4.6). The missing effect also corresponds to the final lifetime in Fig. 4.20 (d) that is reached at all amplitudes; in tracking no losses can be found at the lower amplitudes.

This effect is still not yet fully understood. However, there are some unlikely candidates. The effect of ground motion can be obtained by extrapolating LEP measurements [92,93]. The estimated emittance growth rate due to this effect has a time constant of some hundred years. An estimate for the space charge induced tune shift [94] gives values much below 10^{-6} and collective instabilities could not be observed in the Schottky spectra. Neglected systematic nonlinearities would lead to measurable detuning with amplitude and the SPS tune ripple was measured with good precision with a phase-locked loop. In addition, it can be understood from the measured voltage ripple of the SPS power supplies [95].

A test was made to estimate the effect of random magnetic field errors. Quadrupole and octupole errors in the SPS quadrupoles were considered ($b_{2,ran} = 7.96 \cdot 10^{-4}$, $b_{4,ran} = 4.31 \cdot 10^{-4}$ in the focusing and $b_{2,ran} = 9.95 \cdot 10^{-4}$, $b_{4,ran} = 4.98 \cdot 10^{-4}$ in the defocusing quadrupoles measured at $r_0 = 40$ mm [92,96]). For the test WP2 with natural ripple only was chosen since in this case regular particle motion outside the measured dynamic aperture was found in the simulations (see Tab 4.6). Five random error seeds were examined and the onset of chaos was found to be (9.8) 21.5 mm (compare with the third column in Tab 4.6). The two most unstable seeds were taken for long-term tracking and the smallest aperture obtained was 23.7 mm compared to 25.7 mm without random field errors. This indicates that random field errors can explain a part of the difference between the measured and computed dynamic aperture.

4.5 Phenomenology of Chaotic Particle Motion

One of the main purposes of the aperture studies was to improve the phenomenological understanding of the intricate nature of the particle motion in phase space thus continuing earlier studies [60]. In particular the chaotic regime generated by the interplay of nonlinearities and harmonic tune modulation was of interest.

Simulation studies at WP1, based on the methods described in Sec 3.4, are presented in the following section. The subsequent section describes experimental results which demonstrate the existence of an interesting phenomenon first found in the tracking.

4.5.1 Simulation Results

For working point WP1 and a tune modulation of 9 Hz and $\Delta Q_x = 1.87 \cdot 10^{-3}$ three betatron amplitudes (16.8, 18.8 and 19.5 mm at $\beta_x = 100$ m) close to the long-term dynamic aperture were studied. All sum, skew and difference resonances in that amplitude range up to order 13 are shown in Fig. 4.24.

In the tracking studies the stability of particle motion was tested with three methods. Firstly, the angular distance of a pair of initially close-by particles after 20 000 turns was computed. The most chaotic behavior was found at the smallest amplitude (Tab. 4.7). Secondly, the tunes averaged over one modulation period (5000 turns) were determined for one particle. Twenty averaged tune values at each of the three amplitudes are depicted in Fig. 4.24 together with the tune modulation depth. At the smallest amplitude (most to the right in Fig. 4.24) the 8^{th} order resonance is crossed due the tune modulation leading to large fluctuations of the averaged tunes. The presence of this resonance also explains the strong chaotic behavior found with the first method. The largest amplitude (most to the left in Fig. 4.24) just reaches the 7^{th} order resonance beyond which strong particle loss takes place. Note that the tunes follow closely the detuning curve shown in Fig. 4.11 (a). Thirdly, 640 particles were started with initial conditions distributed over a very small phase space region at each of the three amplitudes and they were tracked for 3 million turns. It is necessary to consider such distributions rather than single particles due to the chaotic nature of the motion in the studied amplitude range in phase space.

The amplitude evolutions for the three starting amplitudes are shown in Fig. 4.25 using 32 of the 640 particles. The amplitudes are averaged over one tune modulation period. At the lowest amplitude (Fig. 4.25 (c)) the particles fill quickly (less than 10^5 turns) an amplitude band around the 8^{th} order resonance and stay within the band. The width of the region of overlapping sidebands computed with formulae (2.69), (2.75) and (2.78) agrees with the width of this band within 10%. The detuning term for this computation was taken from Tab. 4.3 and the driving term was obtained from the resonance island size found in the tracking (see Sec. 3.4 and Eq. (2.69)). None of 640 particles was lost (Tab. 4.7). For the second amplitude (18.8 mm, Fig. 4.25 (b)) the amplitudes spread slowly ($10^5 - 10^6$ turns). Eventually they either reach the 7^{th} order resonance, after which they are extracted in some 10^4 turns, or they are attracted down to the 8^{th} order resonance: in Fig. 4.25 (b) several particles show a decrease in their amplitude after 1.9 million turns

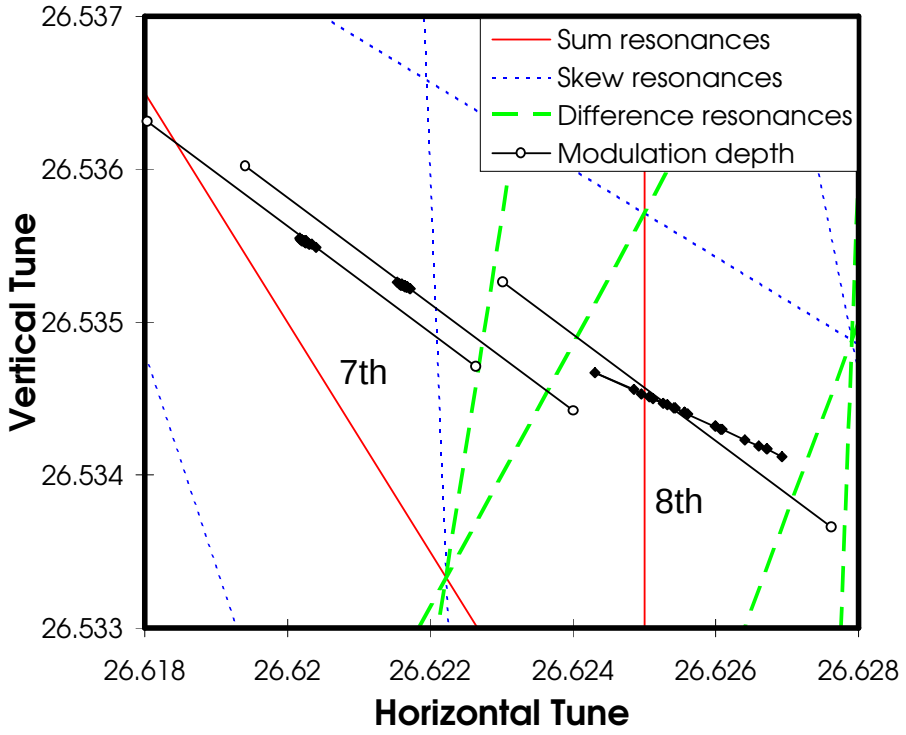

Figure 4.24: Tune diagram and detuning with amplitude at working point WP1. The tune range close to the dynamic aperture is depicted with resonances up to order 13. The lines limited by open circles indicate the tune modulation depth. Their slope is given by the horizontal and vertical beta function at the location of the modulating quadrupole. Each diamond symbol represents the averaged tune per tune modulation period for the horizontal betatron amplitudes 16.8, 18.8 and 19.5 mm (right to left). The averaged tunes are on the detuning curve.

and occupy thereafter an amplitude range which corresponds to that of part (c). The particles starting at 19.5 mm (Fig. 4.25 (a)) fill the same band as the particles starting at 18.8 mm. But since they start very close to the upper band border most particles are lost and only few are attracted to the 8^{th} order resonance.

Fig. 4.26 shows the evolution of the rms amplitude for the three cases. The very chaotic particles starting at 16.8 mm show an strong initial increase of the rms value which is not present in the other cases. For the larger amplitudes the rms values are only given up to 1.7 million and 2.7 million turns respectively, since thereafter a sizable loss or attraction to the 8^{th} order resonance sets in which perturbs the evolution of the rms value.

The observations of the chaotic particle motion in phase space can be summarized as follows: at small amplitudes there is a band of strongly chaotic particles, which nevertheless survive for very long periods. This band is separated from a band of larger amplitudes where individual particles slowly either grow or decrease their betatron am-

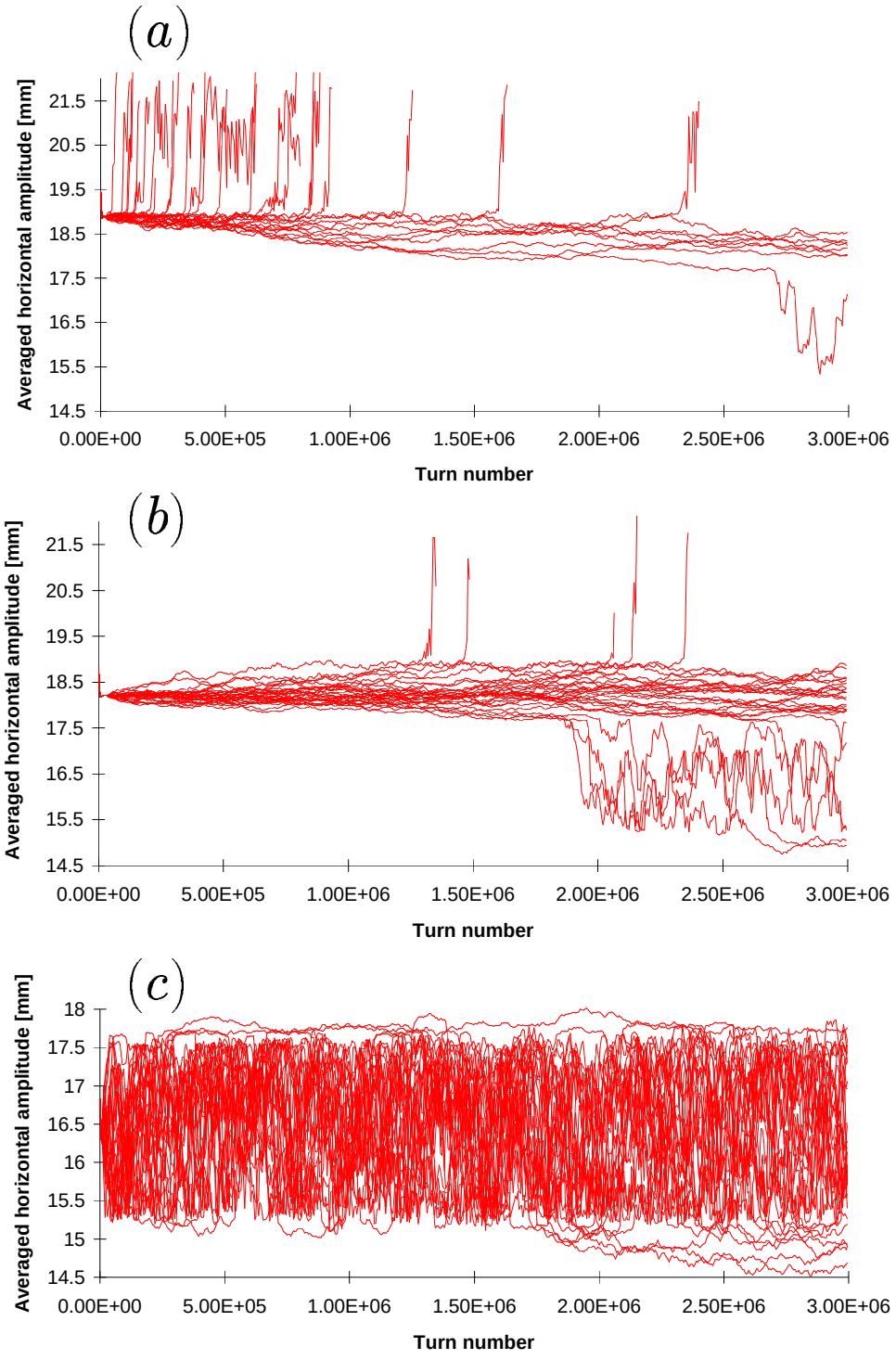

Figure 4.25: Amplitude evolution of particle distributions. 32 particles are started at $a_x = 19.5$ mm (a), 18.8 mm (b) and 16.8 mm (c) under the influence of tune modulation of 9Hz and $\Delta Q_x = 1.87 \cdot 10^{-3}$. The amplitude is averaged over one tune modulation period.

Table 4.7: Stability of particle motion at three different starting amplitudes

Horizontal amplitude [mm] at $\beta_x = 100$ m	16.8	18.8	19.5
Separation angle [π] of 2 particles after 20 000 turns	0.9	$0.45 \cdot 10^{-4}$	$0.8 \cdot 10^{-3}$
Lost particle out of 640	0	102	502
Amplitude rms value [mm] after 1.5 million turns	0.82	0.29	0.28

plitude until they reach the bounds of the band. Finally, beyond a certain amplitude, a rapid particle loss takes place. It has to be mentioned that a band structure was also found at WP2. This scenario is in clear contradiction to a global diffusion model. However, the amplitude evolution in time may be appropriately described by using firstly a separate (amplitude dependent) diffusion coefficient for each band and secondly transition probabilities between these bands.

4.5.2 Experimental Observations

The first prediction from the tracking is the very existence of those bands. They are shown as thick grey lines in figures 4.20 (c) and 4.21 (c) for WP1 and WP2 respectively. The experimental data seem to be consistent with the phenomenological picture: the half beam width decreases in the outer band and increases in the lower band for WP1. At WP2 only one clear band could be identified in the tracking. Above this band the half beam width is decreasing in the experiment while inside and below this band the width stays constant or increases slightly.

The second prediction is the attraction of particles towards lower amplitudes at WP1 which is clearly visible in Fig. 4.25 (b). Due to a large amplitude distribution this effect may however be screened by a considerable intensity loss as seen for instance in Fig. 4.19. It is therefore mandatory to scrape the beam tails so that the particles in the region of fast losses are removed but a sufficient number of particles remain in the amplitude band seen in part (a) and (b) of Fig. 4.25. This type of experiment could be set up in the SPS and the result is depicted in Fig. 4.27.

The double peak structure of a wire scan profile is shown right after the kick and 15 min later. The interesting feature is the shifting of the peaks down to smaller amplitudes without a reduction in peak height. At the same time about 5% of the beam intensity was lost. A system in which the betatron amplitudes increase on average would show a behavior similar to the one depicted in Fig. A.5. There the peaks move slightly inwards but loose considerably in height. Therefore, the experimental observation can only be interpreted as the predicted amplitude decrease of a sizeable fraction of the beam. This observation is not a singular event but was found in four separate experimental runs.

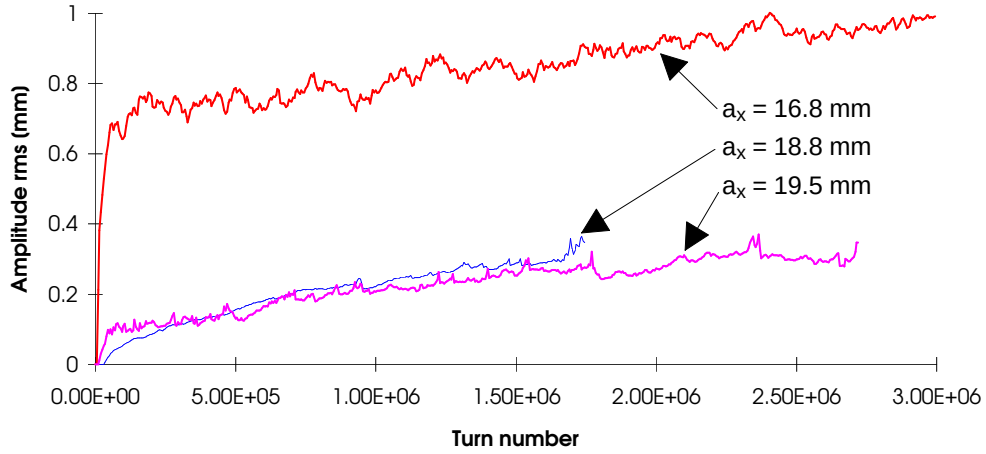

Figure 4.26: Time dependent rms amplitude. The same start amplitudes are chosen as in Fig. 4.25.

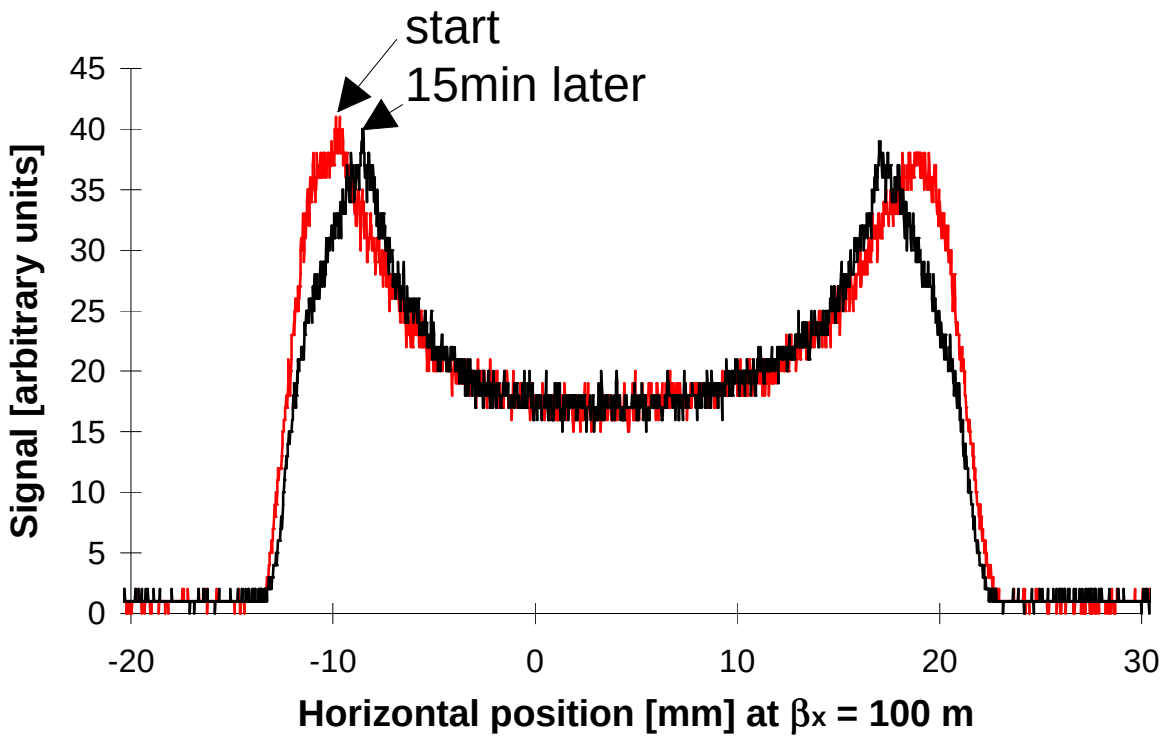

Figure 4.27: Reduction of betatron amplitudes of a sizeable fraction of the beam at working point WP1 (#65). The first scan was taken before the tune modulation was switched on and the second 15 min later. The peaks in the profile move inwards without loosing their height. This means that a considerable number of particles are shifted to smaller amplitudes.

Chapter 5

The Dynamic Aperture Experiment at the HERA Proton Ring

The dynamic aperture of the HERA proton ring at injection energy is limited by strong nonlinear field errors of the superconducting magnets. Persistent currents lead to large systematic multipole errors while mechanical imperfections mainly cause randomly distributed nonlinearities. Moreover, the slow decay of the persistent currents is a source of additional random field errors since the decay rate varies considerably from magnet to magnet.

The magnetic field errors of the superconducting HERA magnets are known in great detail. Each individual magnet was cold tested and the multipole errors were recorded at several excitation levels. In addition, at injection level the decay of the persistent currents was measured. Results of those measurements are available from publications [1,2,97,98] and from a data basis.

No dedicated dynamic aperture experiments have been performed in the first years of the HERA operation. However, from parasitic measurements the dynamic aperture was estimated to be about 7 mm in both planes (at $\beta_y = 76$ m, the maximum beta function in the regular sections) which is only half the value expected from earlier simulations [99]. While the dynamic aperture was sufficient for the operation, the need for higher bunch currents is expected to require a larger dynamic aperture and thus, a clear understanding of the aperture limitations is desirable [100]. Furthermore, the HERA proton ring at injection energy is similar to the LHC in such a regime and an aperture experiment is a good test bench for the numerical tools used in the design process of the LHC.

5.1 Preparation of the HERA Proton Ring

The standard injection optics was used for all studies. Beams of 60 or 10 bunches with standard emittances and momentum spread were prepared (Tab. 5.1).

Great care was taken to adjust the closed orbit in order to assure that the dynamic aperture is inside the physical aperture which is tight at several locations near the interaction points. The physical aperture in the regular sections is 27.5 mm for a perfectly

Table 5.1: Beam parameters for the HERA experiment.

RF	on						
Energy E	40 GeV						
1σ normalized emittance	$\approx 5\text{mm} \cdot \text{mrad}$ hor. and ver.						
Momentum spread $\Delta p/p$	$\approx 5 \cdot 10^{-4}$						
Intensity I (beam current)	$\approx 2 \cdot 10^{12}$ p (13 mA) in 60 bunches $\approx 4 \cdot 10^{11}$ p (3 mA) in 10 bunches						
Closed orbit rms	≤ 2 mm hor. and ver.						
Linear coupling	$\mid Q_x - Q_z \mid \leq 0.002$						
Chromaticity $Q' = \Delta Q/(\Delta p/p)$	≈ 1 hor. and ver.						
Natural tune ripple lines	Frequency [Hz]	50	100	150	200	300	600
	$\Delta Q_{x/z}$ $[10^{-5}]$	15	8	7	4	8	20
Working points (Q_x, Q_z)	(31.284,32.303) (31.287,32.287)						

centered closed orbit. The closed orbit distortions were corrected to rms values below 2 mm in both planes and no orbit deviation was larger than 5 mm. Due to unknown beam position monitor offsets in the order of 1–2 mm and alignment errors, the physical aperture may be reduced. Regions with a reduced aperture were identified by a large loss after a kick, using loss monitors distributed around the whole ring. Short closed orbit bumps were introduced to correct the orbit in these regions. The beam was displaced in both directions until a 80% loss occurred and the orbit was then placed in the middle between the two extreme positions. With this procedure a horizontal physical aperture corresponding to 16.7 mm at $\beta_x = 76$ m (acceptance $A_x = 3.7$ mm·mrad) and a vertical physical aperture corresponding to 13.8 mm at $\beta_z = 76$ m (acceptance $A_z = 2.5$ mm·mrad) was obtained. The linear coupling was corrected with two orthogonal skew quadrupoles and the chromaticity was kept between 0 and 1 in both planes (Tab. 5.1).

For the comparison with simulations a good knowledge of the tune ripple is necessary. Several sources for tune ripple are known for the HERA proton ring [100]: power supply ripple lead to modulation frequencies of multiples of 50 Hz with ripple depths in the order of $\Delta Q_y \approx 10^{-4}$, ground motion in the HERA tunnel causes modulation frequencies between 1 Hz and 20 Hz with modulation amplitudes in the order of $\Delta Q_y \approx 10^{-5}$, vibrations of the vacuum pumps with frequencies at 12 Hz and 24 Hz have modulation amplitudes of $\Delta Q_y \approx 10^{-5}$ [101] and a non-vanishing chromaticity leads to a tune modulation with the synchrotron frequency, typically of the order of $\Delta Q_y \approx 10^{-5}$. In the following only the tune ripple due to the power supply ripple is considered. The relevant tune modulation frequencies and depth were estimated in two different ways: firstly, the voltage ripple at the main power supply was measured and, using a transmission line model of the superconducting magnet string and a model of the optical properties of the HERA proton ring, the tune modulation depths were computed, and secondly, a phase locked loop was used for a measurement of the tune modulation in the stored beam. Six major lines could be identified with both methods (Tab. 5.1). The second method gave larger modulation depth for all lines (particularly pronounced for 600 Hz) which indicates either

that the ripple spectrum changes considerably in time or that there are other sources of tune modulation than the main power supply.

The experimental tunes were chosen close to the operational ones. One setup with separated tunes and one with tunes close to the main coupling resonance was tested (Tab. 5.1).

5.2 Preparation of the Model

The tracking code SIXTRACK [3] allows the implementation of a detailed and realistic model of the HERA proton ring including individual magnetic field maps of all magnets. In the following the treatment of the magnetic multipole errors and the model adjustments are described.

5.2.1 The Multipole Error Treatment

For the multipole coefficients the notation according to (2.18) and (2.19, 2.20) respectively is used. The multipole errors in the tracking model are based on measurements on all superconducting magnets [102,103]. Great care was taken to generate realistic magnetic field errors from the data. Measurements of multipole components may suffer from feed-down effects which are caused by a slightly displaced measurement coil when a strong dominant single multipole component is present. Furthermore, the measurements with the beam extended over many hours, thus the persistent currents have a long time to decay. This motivated the following procedure to generate the multipole errors used in the tracking. The geometric component of the multipole errors are taken from measurements at high excitation of the magnets (3000 A). The persistent current part which is obtained from measurements at 250 A excitation is overlayed. In addition, these values were corrected for persistent current decay using decay data for each individual magnet. For a few quadrupole magnets, the decay data are not complete. Here average values were used.

The North and South quadrants of HERA are equipped with dipoles made by an Italien manufacturer, in the East and West quadrants dipoles made by a German manufacturer are installed. Stronger persistent current decay occurs in the North and South quadrants. Therefore, the corrector currents of these machine parts are varied until a chromaticity of $Q' = \Delta Q/(\Delta p/p) \approx 0$ was obtained in both planes. Tab. 5.2 shows the geometric part of the multipole errors and Tab. 5.3 lists the persistent current part of the multipole errors. There is another effect which modifies the multipole field inside the magnets. If the main field changes, magnetization currents are generated in the corrector coils wound on the beam pipe inside the magnets. The corresponding field distortions which affect the b_3 and b_5 values were taken into account according to Ref. [104].

Table 5.2: Geometric part of the multipole errors, measured at 3000 A, in units of 10^{-4}. The reference radius is $r_0 = 25$ mm.

dipoles (422)									
	Italian (205)		German (217)			Italian (205)		German (217)	
	mean	rms	mean	rms		mean	rms	mean	rms
a_2	-0.421	2.011	-0.009	1.582	b_2	0.013	0.712	-0.034	0.459
a_3	-0.298	0.486	-0.256	0.303	b_3	-0.762	2.431	2.703	1.603
a_4	0.376	0.979	0.194	0.874	b_4	0.044	0.269	0.187	0.178
a_5	0.062	0.215	0.035	0.153	b_5	1.789	0.711	0.929	0.583
a_6	-0.168	0.244	-0.027	0.173	b_6	-0.016	0.115	-0.046	0.096
a_7	0.001	0.117	0.022	0.085	b_7	0.010	0.223	0.340	0.206
a_8	0.016	0.141	0.009	0.098	b_8	0.020	0.077	0.013	0.063
a_9	0.010	0.095	0.024	0.096	b_9	-0.309	0.119	-0.386	0.102
a_{10}	0.016	0.094	0.037	0.088	b_{10}	-0.035	0.098	-0.019	0.085

quadrupoles (224)									
	French (120)		German (104)			French (120)		German (104)	
	mean	rms	mean	rms		mean	rms	mean	rms
a_3	0.398	1.535	0.293	1.247	b_3	0.132	1.533	0.220	1.152
a_4	-0.084	0.990	0.021	0.862	b_4	0.183	0.599	0.017	0.781
a_5	0.060	0.492	-0.018	0.450	b_5	0.741	0.544	0.667	0.626
a_6	0.977	0.423	0.873	0.577	b_6	-2.662	1.226	-2.525	1.098
a_7	0.014	0.232	0.037	0.246	b_7	-0.010	0.216	0.014	0.190
a_8	-0.115	0.313	0.002	0.273	b_8	0.162	0.273	0.149	0.267
a_9	-0.018	0.352	-0.064	0.349	b_9	0.100	0.507	0.098	0.607
a_{10}	0.051	0.382	0.012	0.424	b_{10}	-1.606	0.395	-1.487	0.376

Table 5.3: Persistent current part of the multipole errors, measured at 250 A, in units of 10^{-4}. The reference radius is $r_0 = 25$ mm.

dipoles (422)									
	Italian (205)		German (217)			Italian (205)		German (217)	
	mean	rms	mean	rms		mean	rms	mean	rms
b_3	-34.013	1.422	-33.049	1.304	Δb_3(1800 s)	3.218	0.599	1.798	0.454
b_5	10.777	0.734	11.195	0.862					
b_7	-2.360	0.422	-2.289	0.469					
b_9	0.786	0.457	0.801	0.470					

quadrupoles (224)									
	French (120)		German (104)			French (120)		German (104)	
	mean	rms	mean	rms		mean	rms	mean	rms
b_6	-21.362	1.054	-21.959	1.051	Δb_6(1800 s)	0.967	0.225	1.003	0.185

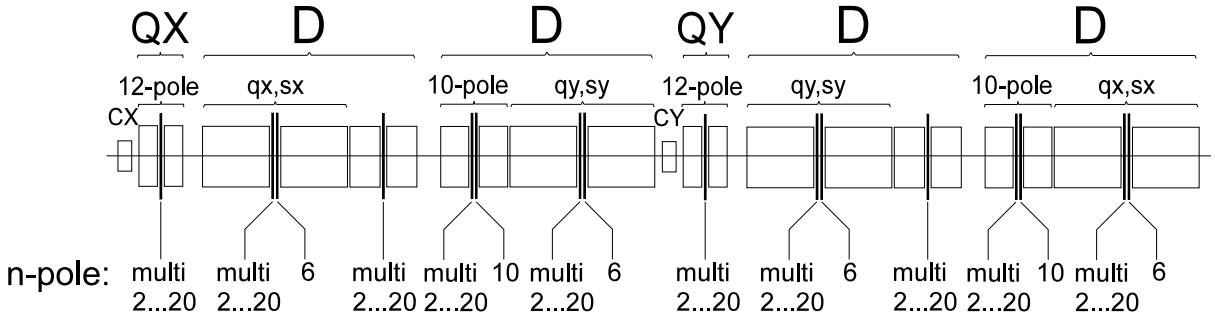

Figure 5.1: FODO cell of the HERA-p tracking model showing the positions of the nonlinear elements (n-poles). CX and CY stand for horizontal and vertical dipole corrector respectively, qx and qz are tuning quadrupoles, sx and sy represent sextupole correctors. Note that according to the HERA conventions the vertical plane is denoted by y instead of z in this picture.

5.2.2 The Tracking Model

The model of the accelerator used in the tracking calculation essentially agrees with the previously used model in Ref. [99]. However, compared to previous calculations, time dependent persistent current effects are taken into account in the description of the magnet field errors. Here is a brief description of the way the machine is represented in the input of the tracking code. Nonlinear forces are represented by thin lenses. In each half FODO cell (with a betatron phase advance of 45°), there are five thin lens kicks (Fig. 5.1). The dipole magnets are split in three parts with two multipole lenses inserted in between. The quadrupoles are split in only two parts. The thin lenses carry the multipolar field errors as obtained from magnet measurements up to order 10 (see Sec. 5.2.1) and they include the effect of correction windings of sextupole, decapole and dodecapole correctors.

The following parameters in the model are adjusted to resemble closely the actual machine parameters in HERA-p: closed orbit, tune, linear coupling, chromaticity and tune ripple. The nonzero closed orbit is generated by random dipole kicks in the multipole lenses. Simulations were performed with corrected and uncorrected orbits[1]. In both cases the kick strength of the random dipole kicks were scaled to obtain the desired values for the rms closed orbit distortion.

Linear coupling is generated by skew quadrupole components of the main field as obtained by the magnet measurements. The width of the coupling resonance is compensated to $\mid Q_x - Q_z \mid \approx 0.0015$ by using two single skew quadrupoles. The chromaticity is adjusted to a value of $Q' = \Delta Q/(\Delta p/p) \approx 0$ with two sextupole families which act in the North and South quadrants only. Finally, harmonic tune modulation is introduced at 8 different azimuthal locations. The number of positions is a compromise between computing effort and the fact that a tune ripple is actually introduced by every element. This approach was justified in [25].

[1] The Fourier transform of an uncorrected closed orbit has a large component at the betatron frequency. The spectrum of a corrected orbit is flat.

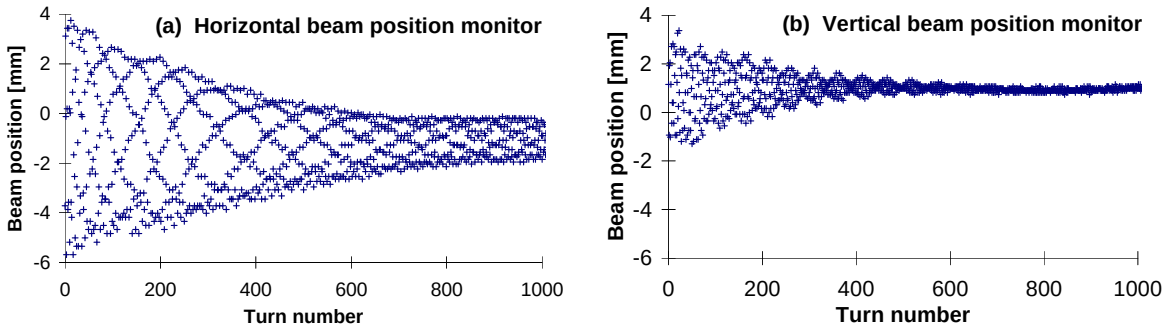

Figure 5.2: The horizontal (a) and vertical signal (b) in one of the position monitors after a horizontal kick corresponding to an action of 0.2 mm·mrad.

5.3 Comparison of Amplitude Dependent Tune Measurements with Calculations

As for the SPS the comparison of the measured and calculated amplitude dependence of the tunes serves as a first test for the tracking model. In HERA the sextupole components are a major contributor to the nonlinearities and one can assume that the Hamiltonian is well approximated by Eq. (2.52). In this case the detuning is given by (2.54) and (2.55).

5.3.1 Measurement of the Detuning

In order to determine the detuning, the beam was kicked in one plane. The betatron oscillations for 1024 turns were recorded using the beam position monitor system. The tunes were determined by two methods: by a Fourier analysis and by calculating the phase advance from turn to turn using two beam position monitors spaced by 90° in betatron phase. This procedure was repeated with different kick strengths. Each measurement was performed with a fresh beam from the injector.

In order to avoid a strong decay of the coherent signal by filamentation, the chromaticity was carefully compensated (see Tab. 5.1). Furthermore, before kicking the beam was scraped to about 20% of its original intensity to remove the tails. The injected beam current amounted to 0.2 mA per bunch, which causes a space charge tune shift in the center of the bunch of $\Delta Q_{Laslett} = 0.0016$ [100]. For small amplitudes, the coherent betatron signal decayed by 50% after 1024 turns (see also Fig. 5.2 for an intermediate kick strength).

The use of several beam position monitors allowed the determination of the tune with a precision of about $5 \cdot 10^{-4}$. In order to excite the betatron oscillations in the horizontal plane, the injection kicker was used. The kick strength was varied corresponding to an increase of the horizontal betatron amplitude between 2.5 mm and 9.1 mm (at $\beta_x = 76$ m). Taking into account the final beam size, the outermost particles of the kicked beam had an betatron amplitude of about 12.5 mm (at $\beta_x = 76$ m).

The tunes of the horizontally excited beams are plotted versus the action associated with the betatron oscillation in Fig. 5.3. It is apparent that the detuning is dominated by the lowest order terms of a nonlinear Hamiltonian system as described by Eq. (2.52). According to equations (2.54, 2.55) the detuning coefficients a and b may be determined from the slopes of the detuning curves by

$$a = \frac{\Delta Q_x}{2I_x},\ b = \frac{\Delta Q_z}{2I_x}. \tag{5.1}$$

The error bars in Fig. 5.3 are determined by taking different time intervals and beam position monitors for the tune computation. Fitting a straight line to the experimental curve, one obtains $a = -(3200 \pm 700)(\text{mm} \cdot \text{mrad})^{-1}$ and $b = (3600 \pm 1600)(\text{mm} \cdot \text{mrad})^{-1}$.

In order to excite vertical betatron oscillations, the beam was injected with a vertical angle. However, this was more difficult to control due to tight aperture constraints and coupling effects in the injection line. Unfortunately, the beam was also oscillating in the horizontal plane and only a few measurements were done. Using the coefficient a from measurements with only horizontally kicked beams, the coefficients b and c can be calculated as follows:

$$b = \frac{\Delta Q_x - 2aI_x}{2I_z},\ c = \frac{\Delta Q_z - 2bI_x}{2I_z}. \tag{5.2}$$

The three measurements made to determine the detuning as a function of the vertical action cover only one fifth of the action range of the horizontal detuning measurement ($I_z < 0.2$ mm·mrad). For the detuning coefficients in Eq. (5.2) one obtains $b \approx 6600$ (mm·mrad)$^{-1}$ and $c \approx 11400(\text{mm} \cdot \text{mrad})^{-1}$ with a relative error of nearly 100%.

Decapole and dodecapole correctors are installed in the HERA proton ring (see Fig. 5.1) to compensate for the large systematic b_5 components in the dipoles and the large systematic b_6 components in the quadrupoles at injection energy (see Tab. 5.3). To test the sensitivity of the detuning with respect to changes in the decapole and dodecapole fields, the exitation currents of these correctors were changed. The excitation current of the decapole correctors was reduced by 50%. This corresponds to a change in b_5 of $3 \cdot 10^{-4}$ at $r = 25$ mm in each dipole magnet. The strength of the dodecapole correctors was reduced by 33% ($\Delta b_6 = 8 \cdot 10^{-4}$ at $r = 25$ mm in the quadrupoles). These variations did not change the detuning within the measurement accuracy. Since the detuning with amplitude depends only weakly on the decapole and the dodecapole correctors strenght it can be concluded that the dominant contribution to the detuning comes from the sextupoles only.

5.3.2 Detuning in the Model

In order to check the sensitivity of the detuning with respect to variations in the input parameters of the model, the following quantities were varied and the corresponding detuning was calculated:

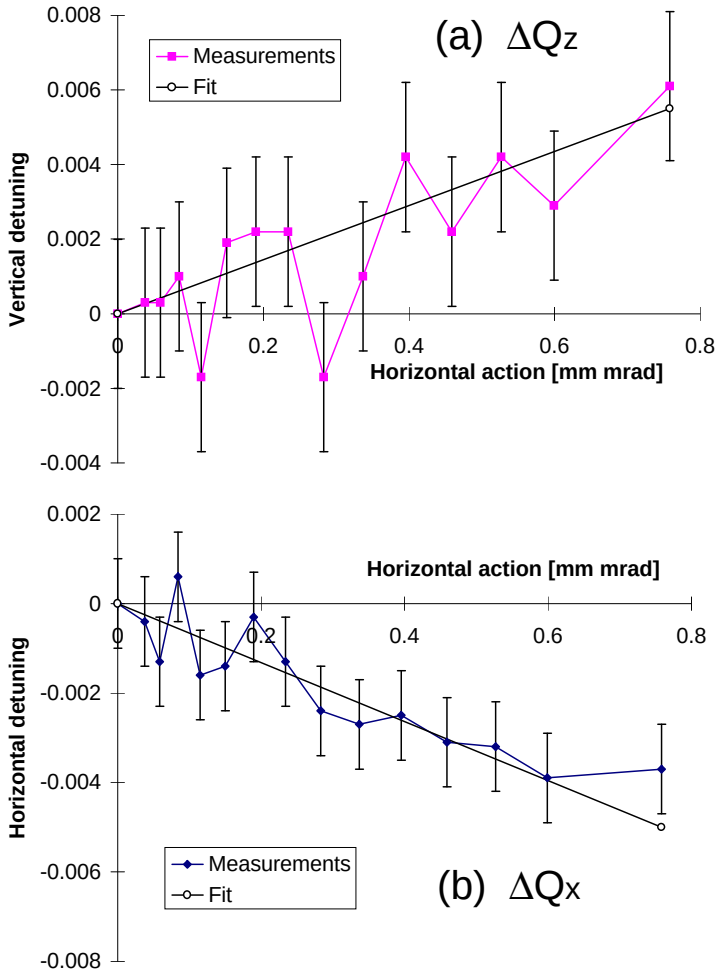

Figure 5.3: Measured horizontal (a) and vertical tune change (b) as function of the horizontal action.

– the set of random dipole kicks that create the closed orbit distortions
– the rms of the closed orbit distortions (1.5 mm to 2.5 mm)
(The rms of the closed orbit distortions in the real machine is uncertain due to unknown offsets in the BPM readings with a rms of about 1 mm.)
– the closed orbit correction (uncorrected or corrected)
– the decapole and dodecapole corrector strengths
– the strength of the sextupoles in the East and West quadrants.

Fig. 5.4 shows detuning results for changes of the horizontal action. In part (a) the reference model is compared with the experimental fit, in part (b), (c) and (d) the influence of different closed orbit distortions, changes in the decapole and dodecapole corrector

strengths and changes in the sextupole configuration (followed by a chromaticity correction) is shown.

As mentioned above, the distribution of the sextupole strength around the superconducting accelerator was not determined with complete certainty. The reason is the decay of the persistent currents which varies from magnet to magnet. One has to rely on the measurements of only two reference magnets which should represent the average of the magnets in the two half rings respectively. Since the chromaticity is only corrected globally in operation it is conceivable that some excess sextupole in one part of the machine is compensated by sextupoles in another part. The impact of such a variation on the detuning was checked by calculations. A variation of the sextupole corrector values in the East & West quadrants by $\pm 5\%$ (a typical value by which the presettings for the sextupole corrector strength vary in operation), changes the detuning coefficient a by $\pm 35\%$ provided the chromaticity was corrected with the sextupole correctors in the East and West quadrants. To clearly point out the effect of changes in the sextupole configuration, the corrector strength in the North and South quadrants was changed by 10% in Fig. 5.4 (d).

From Fig. 5.4 it turns out that only the variation of the sextupole distribution has a noticeable influence on the detuning. From the fact that the measured detuning curves agree well with the calculation based on the sextupole contribution taking into account the persistent current decay, one may conclude that the model reproduces well the distribution of the sextupole strength around the machine.

The input parameters for the reference model used for the computation of the dynamic aperture are chosen such as to yield the proper detuning coefficient a. One then obtains for the coefficient $b = 3600$ $(\text{mm}\cdot\text{mrad})^{-1}$ which is in perfect agreement with the measurement. The purely vertical detuning term c has a too large experimental uncertainty to permit a meaningful comparison. Fig. 5.5 shows one of the working points $(31.285, 32.303)$ used in the HERA-p dynamic aperture experiment at 40 GeV with resonances up to order 13 and the detuning according to an increase of the horizontal and vertical action.

5.4 Dynamic Aperture

As mentioned in Sec 2.11, a practical definition of the dynamic aperture requires to define a time interval of interest. For the HERA experiment times up to 500 s were considered, close to the foreseen injection time of the LHC, while in tracking only 105 s could be reached with reasonable computing effort. As in the SPS experiment the term "dynamic aperture" will be used for the maximum betatron amplitude above particles do not survive the time interval of interest.

5.4.1 Experimental Determination of the Dynamic Aperture

The dynamic aperture of HERA-p was determined at the injection energy of 40 GeV using two methods. In the first method the edge of the stable region was reconstructed from beam loss measurements of a kicked beam of small transverse dimensions ("pencil"

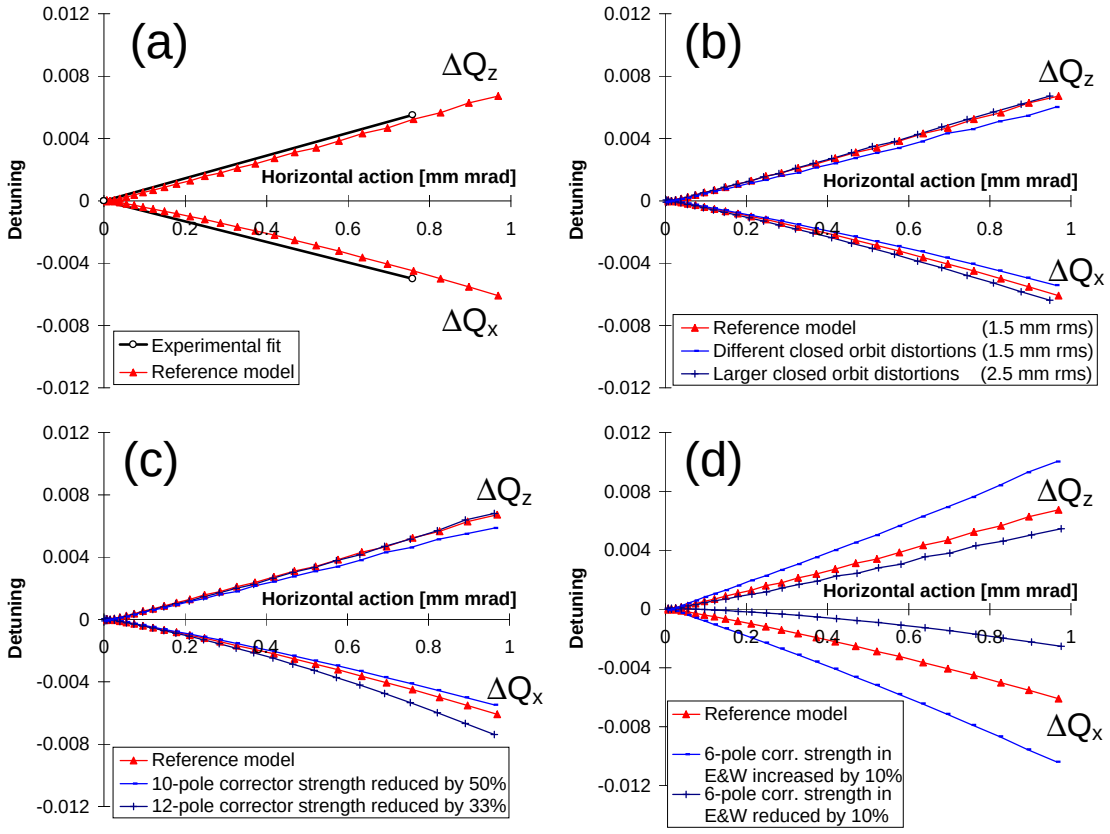

Figure 5.4: Detuning in the simulation as a function of horizontal action and for different parameter values. Part (*a*) shows the comparison of the reference model with the fit to the experimental data, part (*b*) the influence of different closed orbit distortions, part (*c*) the influence of changes in the decapole and dodecapole corrector strength and part (*d*) the influence of changes in the sextupole strength in the East and West quadrants followed by a global chromaticity correction using the sextupole correctors in the North and South quadrants.

beam) assuming an scraped Gaussian particle distribution before the kick. In the second method the available aperture was filled with a kicked beam and the base width of beam profiles, taken from a rest gas ionization monitor, were measured. The first method gives somewhat smaller results for the aperture and is described in detail in Ref. [100]. An interesting outcome is that one has to assume beam tails, which built up right after scraping, to obtain consistent results for different kick strengths. Here, only on the second method will be reported. In the following all betatron amplitudes are normalized to 76 m, the maximum value in the arcs.

Beams with 60 bunches and an intensity of about $3 \cdot 10^{10}$ protons per bunch were used (Tab 5.1). The measurements were performed in the following way. The beam was kicked horizontally with the injection kicker. The kick strength was chosen such that part of

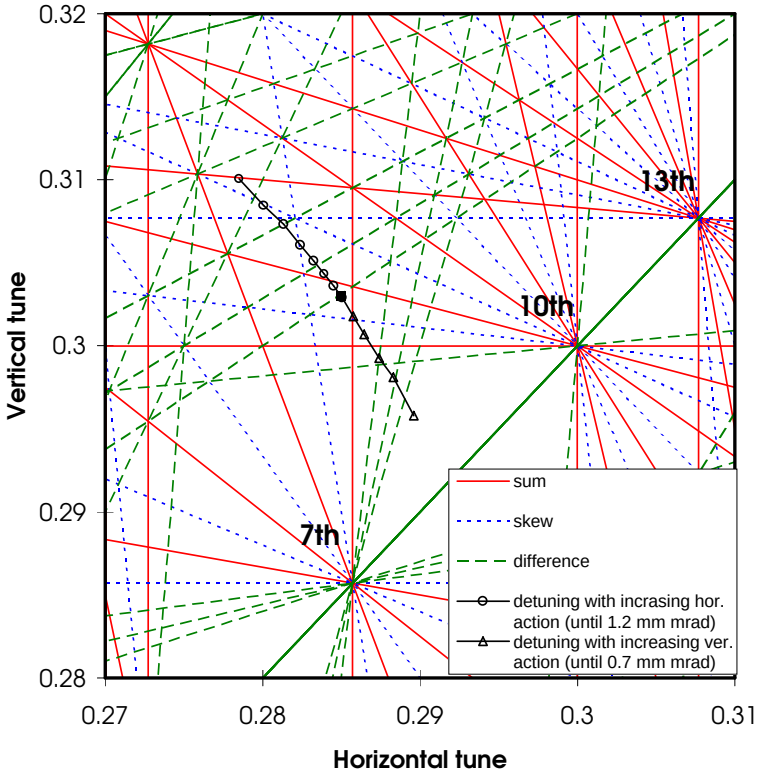

Figure 5.5: Tune diagram for the dynamic aperture experiment at the HERA proton ring at injection energy. Resonances up to order 13 and the detuning according to an increase in the horizontal and vertical action is shown for the working point (31.285, 32.303). The detuning range corresponds to the beam size in the experiment.

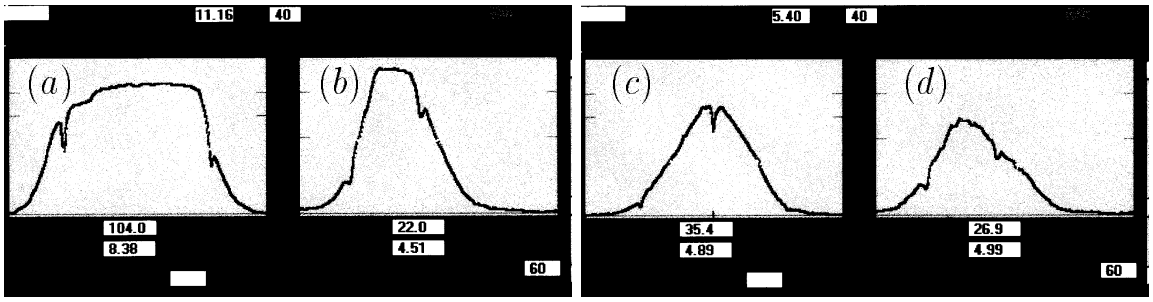

Figure 5.6: Beam profiles at two different times after a horizontal kick with a beam of 60 bunches [100]. Part (a) and (b) show the horizontal and vertical beam profile respectively right after the kick, the horizontal profile (c) and the vertical profile (d) were taken 10 minutes later. The notches are markers to determine the width of the profile.

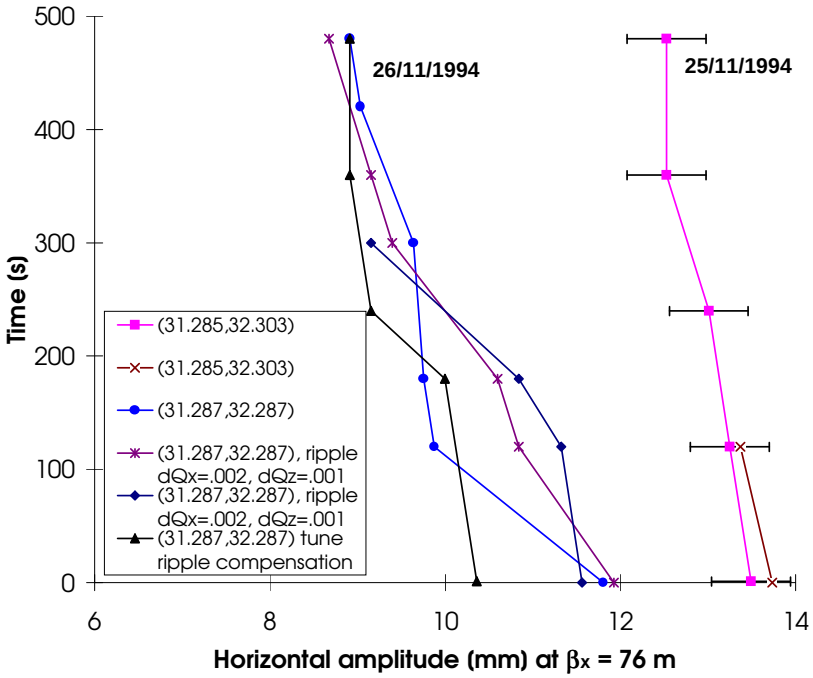

Figure 5.7: Horizontal dynamic aperture at 40 GeV derived from beam profile measurements.

the beam was lost at the physical or short term dynamic aperture. This way, the beam filled the whole available aperture. A shrinking of the base width of the horizontal beam profile went along with particle losses for about 10 min. Fig. 5.6 shows the horizontal and vertical beam profiles at two different times after the horizontal kick.

The rest gas ionization monitor, with which the beam profiles were recorded, has a time constant of about 0.5 s. For the beam parameters under consideration, the systematic error of this monitor ($\approx 1\%$ error of the measured width) and its resolution (0.1 mm) are sufficiently small to be neglected in the aperture measurement [105]. In Fig. 5.7 the results of six series of beam profile measurements are depicted. The maximum survival time of the outermost particles is shown as a function of the horizontal betatron amplitude.

The two rightmost curves in Fig. 5.7 are derived from measurements with a tune of (31.285, 32.303) (see Fig. 5.5 for the working diagram), with 60 bunches, 0.2 mA per bunch and a residual beam current of 6-7 mA after the kick. The edge of the beam distribution immediately after the horizontal kick is at 13.6 mm which corresponds to an emittance of about 2.4 mm $\cdot$ mrad. For one of these cases the profile was observed over a period of 500 s in which the maximum horizontal amplitude decreases to 12.4 mm, corresponding to an emittance of 2.0 mm$\cdot$mrad. The error bars in Fig. 5.7 are determined from the uncertainty of reading the base width of the rest gas monitor profile. Due to coupling effects, the motion excited by the injection kicker is not purely horizontal. The

vertical beam profile which was observed simultaneously indicates that the initial vertical amplitudes after the kick amounts up to 8.3 mm.

The four cases on the left-hand side in Fig. 5.7 were measured one day later and with only 10 bunches per beam. The beam was kicked with the injection kicker which reduced the intensity from 3 mA to 1 mA. The tunes were close to or within the width of the coupling resonance at (31.287, 32.287). In two cases an additional tune modulation of 50 Hz and a depth of ($\Delta Q_x = 0.002, \Delta Q_z = 0.001$) was applied. In another case the natural tune ripple at 100 Hz, 300 Hz and 600 Hz was compensated. All four runs exhibit the same behavior within the measurement precision. In all cases investigated the measured horizontal edge of the beam distribution was significantly smaller than for the two cases shown in the right-hand side of Fig. 5.7. Since the beam was right on the coupling resonance, the initial horizontal and vertical betatron oscillation amplitudes are expected to be equal. This is approximately confirmed by the beam profiles after the kick. The edge of the beam immediately after the kick was found at 10.5 mm horizontally and 9.2 mm vertically. The emittance values which correspond to the beam edges are $\epsilon_x =$ 1.45 mm·mrad and $\epsilon_z = 1.2$ mm·mrad. Ten minutes later the values are reduced to 8.7 mm horizontally and vertically corresponding to emittance values of $\epsilon_{x/z} = 1.0$ mm $\cdot$ mrad.

5.4.2 Dynamic Aperture in the Model

The dynamic aperture is computed by two methods: firstly, the chaotic border is determined from the evolution of the distance of pairs of initially close-by particles (Lyapunov analysis), and secondly, by long-term tracking over 5 million turns. To get an upper bound for the dynamic aperture particles were launched in the horizontal plane only; vertical motion was introduced through coupling. The momentum amplitudes were $\Delta p/p \approx 1 \cdot 10^{-4}$ (0.66 σ of the longitudinal distribution). It was checked by tracking that particles with small momentum amplitude survive longer than particles with larger amplitudes. For the estimation of a lower bound (number in brackets in column six in Tab. 5.4), the vertical start amplitude was about 0.5 σ of the measured vertical amplitude distribution. In some cases (#2, #10 and #12) a Lyapunov analysis was done with $2 \cdot 10^5$ instead of $2 \cdot 10^4$ turns and it was found that $2 \cdot 10^4$ turns may not always be sufficient for detection of chaos.

Tab. 5.4 summarizes all tracking cases. The reference case (#1) has a modest rms of closed orbit distortions, a detuning that agrees with the experiment and no tune ripple. The other cases have the following properties: an uncorrected closed orbit (#2, #3, #6, #8, #10, #11, #12), a larger rms of closed orbit distortions (#3, #11), a stronger detuning (#5, #6, #12), a weaker detuning (#7, #8), tune ripple (#9 to #12) and finally different tunes (#4) with a coupled beam.

The table allows a qualitative differentiation between the various effects. There is no significant systematic difference between a corrected and an uncorrected closed orbit (compare #1 with #2, #5 with #6 and #7 with #8). The increase of the rms of closed orbit distortions as well as the addition of tune ripple leads to a reduction of the dynamic aperture but both effects do not add up when combined. Increasing the detuning (by changing the sextupole configuration) leads to an even larger reduction in the dynamic

Table 5.4: Stability of particle motion in the tracking simulation. All amplitude values are given for $\beta_x = 76$ m, "SP E&W" stands for a change in the sextupole corrector strength in the East and West quadrants followed by a subsequent global chromaticity correction using the sextupole correctors in the North and South quadrants. The stepsize for the detection of chaos is 0.53 mm, for long-term tracking it is 0.13 mm. The number in brackets in column six gives a lower estimate for the horizontal chaotic border (obtained with an increased vertical start value), the other number in column six gives an upper bound for the horizontal chaotic border (vertical start value zero).

#	tune	closed orbit distortions hor. rms [mm]	closed orbit distortions ver. rms [mm]	remark	onset of chaos [mm]	turns	loss border [mm]	turns
1	(31.2850, 32.3030)	1.5	1.5	orbit corrected	(12.2) 14.7	$2 \cdot 10^5$	–	–
2	(31.2850, 32.3030)	1.5	1.5	orbit uncorrected	15.6 15.1	$2 \cdot 10^4$ $2 \cdot 10^5$	15.2	$5 \cdot 10^6$
3	(31.2850, 32.3030)	2.5	2.5	orbit uncorrected	14.4	$2 \cdot 10^4$	–	–
4	(31.2877, 32.2862)	1.5	1.5	coupled, orbit corrected	15.4	$2 \cdot 10^5$	–	–
5	(31.2850, 32.3030)	1.5	1.5	SP E&W +5% orbit corrected	(12.4) 13.9	$2 \cdot 10^5$	–	–
6	(31.2850, 32.3030)	1.5	1.5	SP E&W +5% orbit uncorrected	13.9	$2 \cdot 10^4$	–	–
7	(31.2850, 32.3030)	1.5	1.5	SP E&W −5% orbit corrected	(12.3) 15.6	$2 \cdot 10^5$	16.4	$5 \cdot 10^6$
8	(31.2850, 32.3030)	1.5	1.5	SP E&W −5% orbit uncorrected	16.7	$2 \cdot 10^4$	–	–
9	(31.2850, 32.3030)	1.5	1.5	tune ripple orbit corrected	(6.97) 14.1	$2 \cdot 10^5$	–	–
10	(31.2850, 32.3030)	1.5	1.5	tune ripple orbit uncorrected	14.5 13.9	$2 \cdot 10^4$ $2 \cdot 10^5$	14.3	$5 \cdot 10^6$
11	(31.2850, 32.3030)	2.5	2.5	tune ripple orbit uncorrected	13.8	$2 \cdot 10^4$	13.8	$5 \cdot 10^6$
12	(31.2850, 32.3030)	1.5	1.5	SP E&W +5%, tune ripple orbit uncorrected	13.4 12.8	$2 \cdot 10^4$ $2 \cdot 10^5$	13.2	$5 \cdot 10^6$

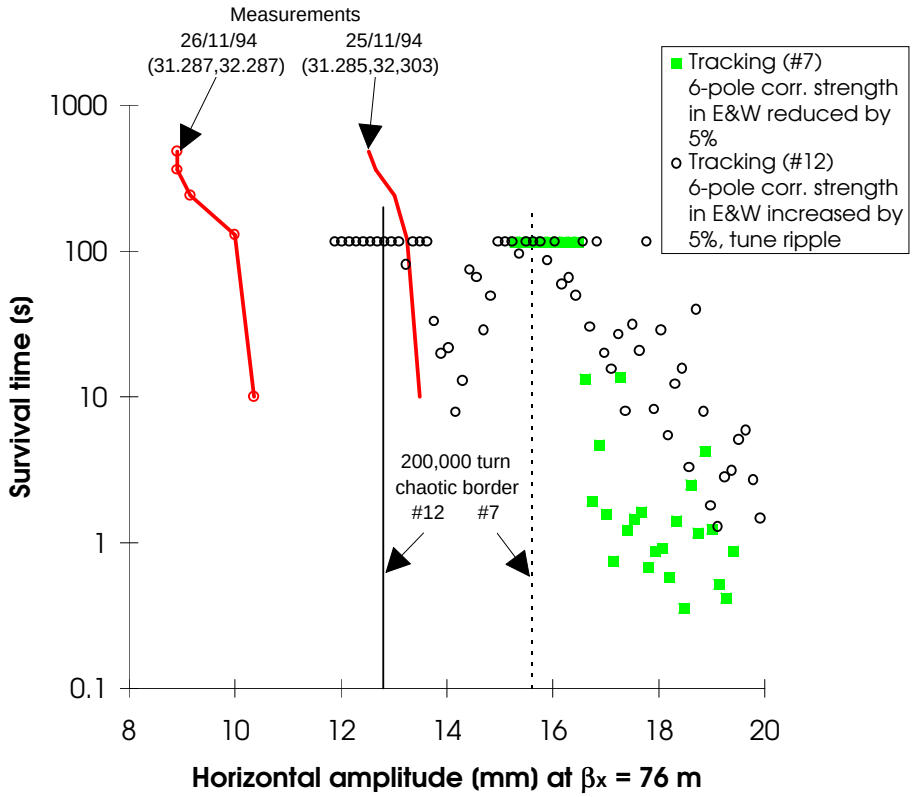

Figure 5.8: Survival plots for the cases #7 and #12 (Tab. 5.4) together with their chaotic border and the horizontal dynamic aperture measured under different conditions.

aperture, while decreasing the detuning increases the dynamic aperture by roughly the same amount. Finally, adding the tune ripple leads to a further reduction of the stability border. Coupling does not seem to decrease the stable area (#4). It is interesting to notice that in two cases with tune ripple (#10, #12) a region with chaotic behavior was discovered in an amplitude range well inside the dynamic aperture.

Out of the four cases for which long-term tracking was performed the two with the smallest and the largest loss border respectively are depicted in the survival plot in Fig. 5.8. Shown are the losses between 0.1 and 100 s and the chaotic borders together with the measured horizontal dynamic apertures. Particles surviving longer than 5 million turns build the upper straight line at 105 s.

5.4.3 Comparison of Measured and Computed Dynamic Aperture

The loss border (determined after 5 million turns or 105 seconds) of the cases, for which long-term tracking was performed, was found to be less than 5% larger than the chaotic border. Therefore, it may be justified to compare the measured dynamic aperture (deter-

mined after 500 s) with the chaotic border in the tracking simulations.

In the experiments there is no adequate control of the vertical oscillation amplitudes due to uncorrected local coupling. The coupling is only corrected globally using two orthogonal skew quadrupoles. In the detuning measurements an amplitude ratio between vertical and horizontal betatron amplitudes of up to 39% could be observed (see Fig. 5.2). Therefore, the coupling should always be considered in the interpretation of the measured aperture data by using the sum acceptance $A = A_x + A_z$ or the total transverse aperture $a_{trans} = \sqrt{\beta(A_x + A_z)}$ [35].

Since the vertical amplitude of particles at the horizontal beam edge can not be determined in the experiments an interval for A and a_{trans} will be given, that is possible according to the coupling. For the measurements with separated tunes one obtains in this way a range for the total dynamic aperture after 500 s of $(12.6 - 13.5)$ mm (the upper bound is determined as $12.6 \cdot \text{mm}\ \sqrt{1 + 0.39^2} = 13.5$ mm) which corresponds to a sum acceptance range of $(2.08 - 2.39)$ mm $\cdot$ mrad.

For the measurements on the coupling resonance an almost round beam was observed. Hence the maximum total dynamic aperture should be $\sqrt{2}$ times the measured horizontal or vertical beam edge which gives an interval of $(8.8 - 12.4)$ mm or a sum acceptance of $(1.01 - 2.02)$ mm $\cdot$ mrad.

In Tab. 5.5 the results are summarized. The larger number given in column five (relative difference between measurement and tracking) is a pessimistic estimate.

For the separated tunes the measured and computed dynamic aperture agree to within 20%. However, the residual coupling in the tracking was smaller than in the experiment and the amplitude ratio observed in the experiment was not reached for particles which were started with a vanishing vertical amplitude. Space charge effects were disregarded in the simulation. They would lead to a 10–20% change of the detuning coefficients [100]. Since the aperture is strongly dependent on the detuning (see cases #5 to #8 and #12 in Tab. 5.4) this effect may explain a part of the discrepancy. If one compares the dynamic aperture values for the tracking cases with increased detuning (#5, #6 and #12) with the best experimental value one obtains an agreement better than 10%.

On the coupling resonance the agreement between measured and computed dynamic aperture is worse than with separated tunes (Tab. 5.5). However, the experimental result that neither additional tune modulation ($\Delta Q_x = 0.002, \Delta Q_z = 0.001$) nor the compensation of the largest tune ripple frequencies changed the measured dynamic aperture at this working point is not understood. Theoretical estimates [8] and the SPS experiments showed a clear dependence of the dynamic aperture on such a large tune ripple. Furthermore, the tune ripple compensation has been successfully applied under collision condition with beam-beam interaction to reduce the particle loss [106].

In 1995, half beam profile widths of 11.8-12.5 mm (at $\beta_x = 76$ m) were obtained with parasitic profile measurements at injection energy during normal operation. These numbers are a lower estimate for the dynamic aperture since the beam was not kicked and the physical aperture was not as large as one year before. In some of these measurements the tunes were very close to the ones on the coupling resonance in 1994. Since all these

Table 5.5: Comparison of measured and computed dynamic aperture of the HERA proton ring at 40 GeV. All amplitude values are given for $\beta = 76$ m. The range of acceptance or aperture for the measured values is determined by assuming a minimal or maximal vertical amplitude possible for the obtained horizontal beam edge using the measured coupling. The range in the computed aperture is obtained by varying input parameters (see Tab. 5.4). Case #8 out of this table was disregarded since the chaotic border was determined with $2 \cdot 10^4$ turns only and may be therefore too large.

case		amplitude ratio	transverse acceptance	transverse dynamic aperture	relative difference between measurement and tracking
(Q_x, Q_z)		$\sqrt{A_z}/\sqrt{A_x}$	$A_x + A_z$ [mm · mrad]	$a_{trans} = \sqrt{\beta(A_x + A_z)}$ [mm]	$\left(\frac{a_{trans,track}}{a_{trans,meas}} - 1\right)$ [%]
(31.285,32.303)	measured	$\lessapprox 0.39$	2.08–2.39	12.6–13.3	3–23
	tracking	≈ 0	2.29–3.54	12.8–15.6	
(31.287,32.287)	measured	≈ 1	1.01–2.02	8.8–12.4	23–75
	tracking	≈ 0.8	3.11	15.4	

numbers are larger than the dynamic aperture measured on the coupling resonance in 1994 it is likely that a unknown effect reduced the dynamic aperture at that time which is normally not present.

Like in the SPS experiment there are indications that the particle losses in the HERA proton ring at injection energy can not be described by a simple diffusion mechanism as it is possible under collision conditions. The gap which is created by a retracted scraper is filled much too fast and not with steadily increasing speed [107].

Taking into account all experimental observations it is likely that there exists a yet unknown mechanism that leads to particle loss. The necessary assumption of beam tails right after scraping to obtain consistent aperture values from beam loss experiments (as mentioned in Sec 5.4.1) indicats such a mechanism which may explain the remaining difference of measured and computed dynamic aperture even present for the separated tunes in 1994.

Chapter 6

Dynamic Aperture Simulation for the LHC

In the last two chapters it has been shown that tracking simulations can reproduce the dynamic aperture of hadron rings in the presence of nonlinear magnetic fields and harmonic tune modulation with reasonable accuracy. Such conditions are typical for the LHC at injection energy where the particles have to survive for about 15 minutes before the acceleration can start. In this chapter a study will be presented that examines the influence of tune modulation on the dynamic aperture of the LHC at injection energy [108].

From the experience of existing superconducting magnets an estimate of the magnetic field errors can be derived. However, little is known about the level of tune modulation to be expected from the power supplies of the LHC. As a first guess the measured tune ripple of the SPS was used.

6.1 Preparations

The LHC lattice version 2 at injection energy and the set of multi-polar errors assumed at that time was used (see Tab. 6.1 and Ref. [109]). Two seeds of random magnetic errors in the LHC dipoles and up to four ripple depths were tested. For both seeds of random magnetic errors it was checked that only few values are outside and close to 3 σ of the distribution (at that time no cut was applied in SIXTRACK). For both cases a nonlinear detuning correction using normal forms (see Sec. 2.10 and Ref. [33]) was performed using sextupoles and decapoles. Round beams with equal horizontal and vertical emittances were tracked and the full 6 dimensional phase space was considered with a relative momentum deviation of $\Delta p/p = 1.25 \cdot 10^{-3}$.

For the modulation spectrum seven ripple lines in the range from 50 Hz to 1000 Hz were taken (see Tab. 4.1 and Ref. [95]). Their ripple depths $\Delta Q_{x/z}$ were ranging from about $5 \cdot 10^{-6}$ to $5 \cdot 10^{-5}$ with a total cumulated depth of roughly 10^{-4}.

For every case, 64 particles were tracked up to 3 million turns (about 5 minutes of storage time) which takes 15 to 20 days of CPU-time each (see Tab. 3.2). For this

Table 6.1: Multipole errors of the LHC dipoles at injection energy in units of 10^{-4}. The referenc radius is $r_0 = 10$ mm. The systematic imperfections refer to the magnets of ring 1 where particles rotate clockwise. The + sign is used in the odd arcs, the − sign in the even arcs [109].

	mean	rms		mean	rms
a_3	± 0.086	0.186	b_3	-3.800	0.882
a_4	0.023	0.186	b_4	∓ 0.110	0.550
a_5	± 0.020	0.041	b_5	0.340	0.083
a_6	0.000	0.022	b_6	∓ 0.001	0.014
a_7	± 0.010	0.011	b_7	0.035	0.012
a_8	0.000	0.005	b_8	± 0.002	0.005
a_9	0.000	0.004	b_9	0.007	0.003

purpose SIXTRACK had to be adapted to the used hardware (IBM-SP1 RISC station cluster at that time) and system software to render optimal tracking speed and data loss protection in case of a system crash [110]. Half a month of CPU-time has to be considered the ultimate limit and only a few carefully chosen cases could be treated in this way.

6.2 Results

Part (a) and (b) of Fig. 6.1 show the survival plots of a "good" seed (denoted as "Seed No 1"). In part (a) the simulations are shown for the case without and with tune ripple (total ripple depth 10^{-4}). Above 9 mm (corresponding to about 10 s survival time) no difference is observed. Below that value the loss time of particles is in most cases smaller when a tune ripple is applied. This is even more pronounced when the ripple depth is increased by a factor of 5 (Fig. 6.1 (b)).

The border of stability for the tracked 3 million turns shrinks from 8.2 mm to 7.2 mm (at $\beta_x = 172$ m) when the strong ripple ($5 \cdot 10^{-4}$) is applied. That is a reduction of the dynamic aperture by 12%. Shown in the same graph are the borders of onset of chaotic motion which in the case of increased ripple depth is reduced by about 10% (6.3 mm compared to 5.8 mm). It is interesting to note that the border of chaotic motion is not altered when the ripple is increased by another factor of 2 but the particle loss after 10 s increases.

In Fig. 6.2 (a) and (b) a "bad" seed (denoted as "Seed No 2") is shown. In this case the dynamic aperture is reduced by a factor of 1.5 compared to the "good" seed. Part (a) shows that there is a large spread and no difference in loss times with or without ripple above 6.5 mm (corresponding again to about 10 s) and here even below 6.5 mm the difference in the loss times is not very pronounced. Increasing the ripple depth by a factor 5 (Fig. 6.2 (b)), as in the other case, leads to faster particle loss beyond 10 s and the stability border for 3 million turns (267 s) is decreased from 5.9 mm to 4.9 mm, i.e. by 17%. The reduction of the border of chaotic motion is even more pronounced in this case: some 30% from 3.2 mm to 2.3 mm.

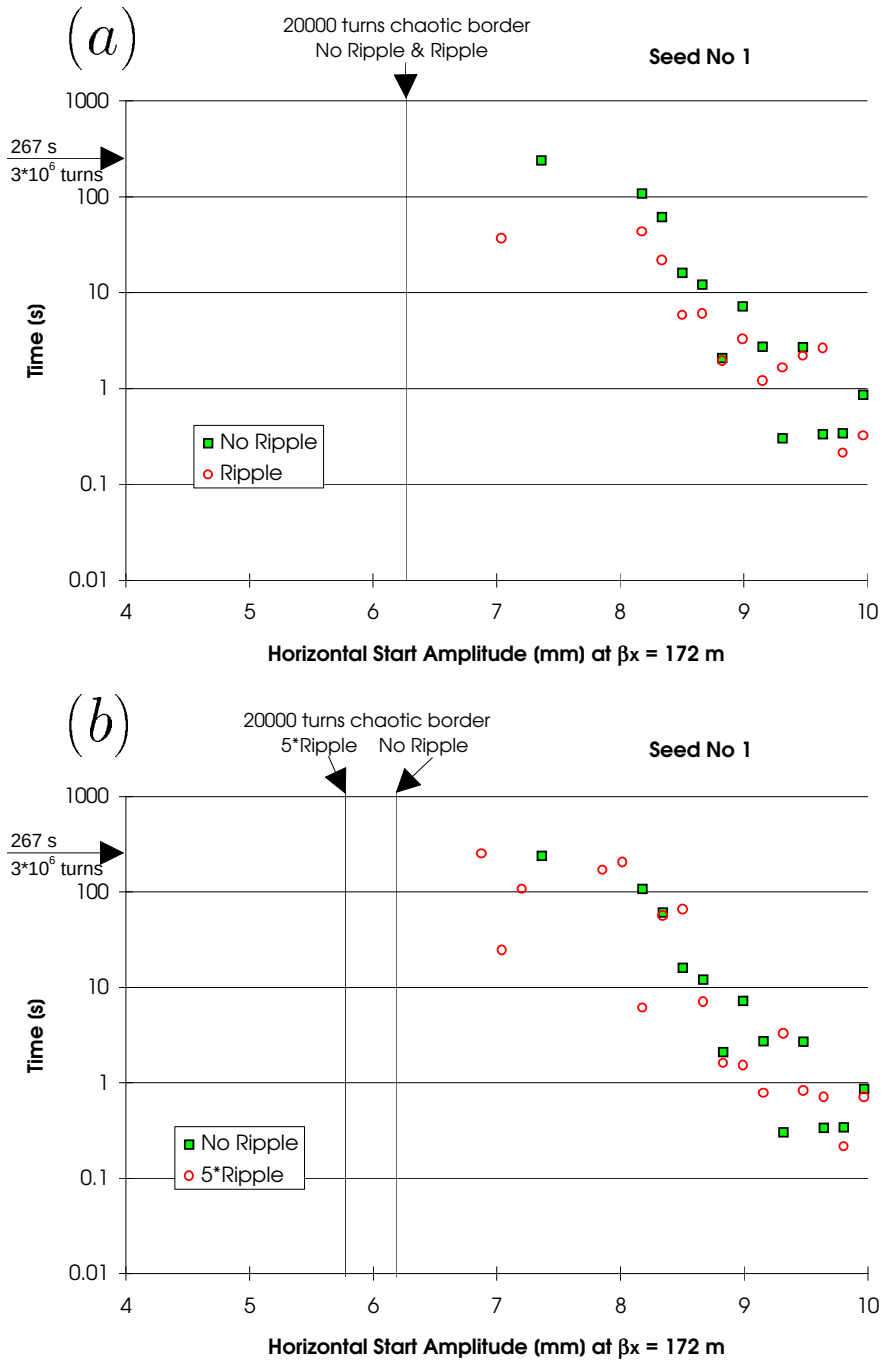

Figure 6.1: Survival plots for LHC version 2 which show the influence of tune ripple on the dynamic aperture at injection energy for a "good" seed of random multipole errors. In part (a) the LHC without tune ripple is compared with the LHC with a tune ripple of 10^{-4}, in part (b) a five times stronger tune ripple is applied. Only particles that are lost prior to $3 \cdot 10^6$ turns, corresponding to 267 s storage time, are shown.

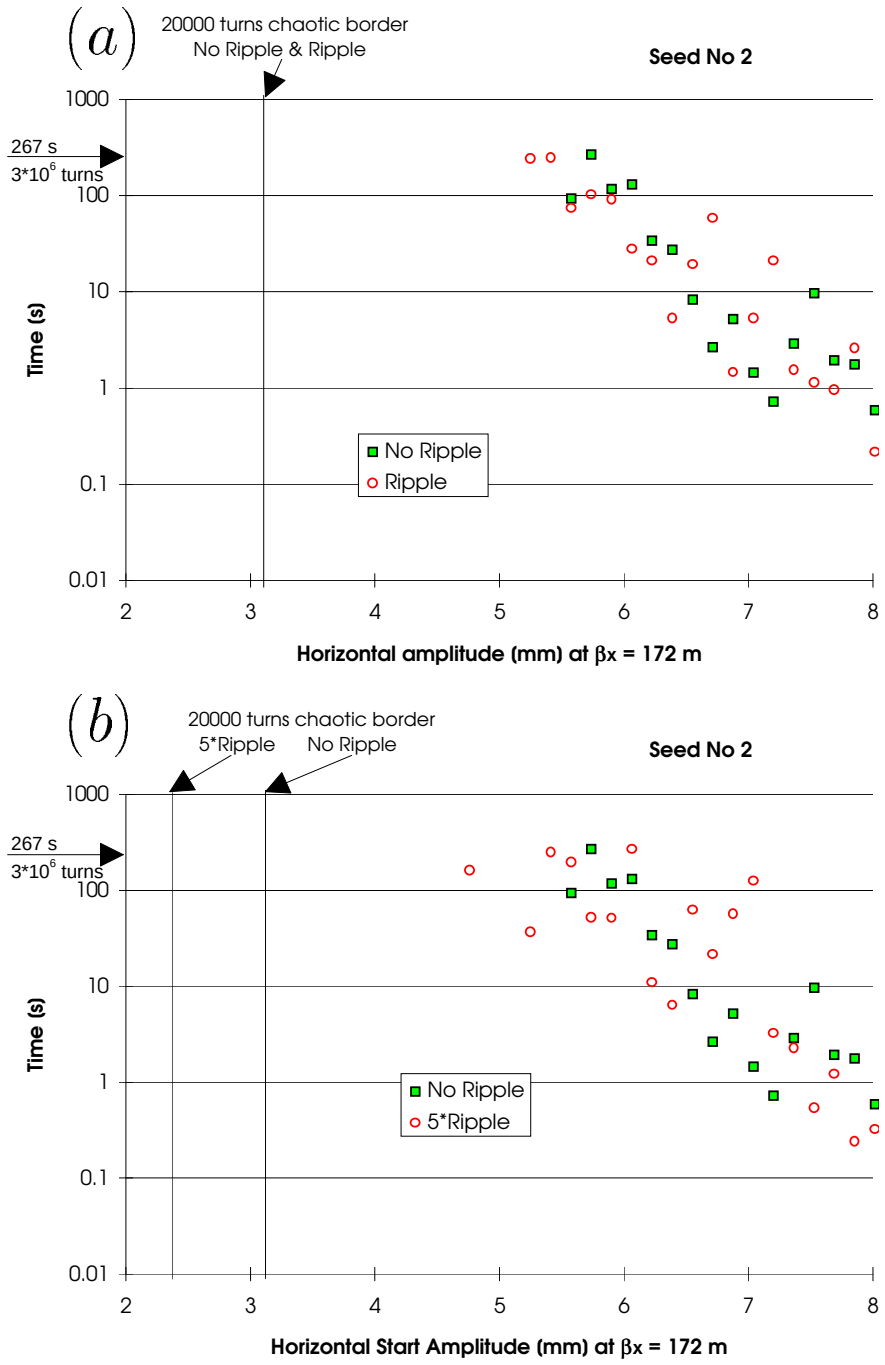

Figure 6.2: Survival plots for LHC version 2 which show the influence of tune ripple on the dynamic aperture at injection energy for a "bad" seed of random multipole errors. In part (a) the LHC without tune ripple is compared with the LHC with a tune ripple of 10^{-4}, in part (b) a five times stronger tune ripple is applied. Only particles that are lost prior to $3 \cdot 10^6$ turns, corresponding to 267 s storage time, are shown.

In summary, a reduction of the dynamic aperture of more than 10% has been observed when a tune ripple is considered which is 5 times the measured values of the SPS, i.e. $5 \cdot 10^{-4}$. The border of chaotic motion is reduced by at least 10% for both seeds.

Currently it is foreseen to put scrapers at 6 σ with an assumed sigma of 1.2 mm at $\beta_y = 176$ m [111]. Taking into account that both cases are tracked with equal horizontal and vertical emittance and assuming that the sum acceptance is approximately the same for all ratios of horizontal and vertical amplitudes, the calculated dynamic apertures have to be multiplied with $\sqrt{2}$ to obtain the horizontal or vertical dynamic aperture. In this way one finds that the dynamic aperture of the "bad" seed is sleightly smaller than the foreseen limit when the strong tune ripple is applied.

For a more realistic evaluation of the effect of tune modulation a better estimate of the LHC tune ripple spectrum is needed. To this end studies are pursued to derive such a spectrum from LHC magnet measurements and calculations. Moreover the considerably smaller dynamic aperture for the "bad" seed is not yet understood.

Chapter 7

Conclusions

In this thesis the long-term stability of particle motion in hadron storage rings has been examined. Chaotic motion generated by transverse nonlinear fields and harmonic tune modulation was considered. A large amount of experimental data was collected and analyzed. The experimental results were compared with computer simulations.

The initial objective of a series of SPS experiments had been to obtain quantitative results for the transport coefficient as a function of betatron amplitude, tune modulation frequency and tune modulation depth. Despite sustained effort this objective was not attained with the techniques available. Instead, detailed studies revealed that the physical system under study was much more complex than anticipated. However, qualitative results of earlier experiments could be confirmed: the loss rates increase with increasing tune modulation depth but there is practically no dependence on the tune modulation frequency in the range from 9 to 180 Hz. The effect of two modulation frequencies was tested and found to be in qualitative agreement with theoretical expectations.

Dynamic aperture measurements were performed at the SPS, with controlled nonlinearities created by 8 strong sextupoles, and the HERA proton ring under normal operating conditions. These measurements were compared with long-term computer tracking. For the SPS the measured and computed dynamic aperture agree within 10% when a tune ripple about 10 times stronger than the natural one was applied. This agreement deteriorates for a smaller tune modulation depth and the relative difference reaches about 20% when only the natural tune ripple is considered. A 20% agreement between measurement and simulation could also be achieved for the HERA proton ring given clear experimental conditions. In both cases an additional destabilizing effect seems to be missing that is not yet identified.

Experimental results from the SPS and the HERA proton ring at injection, as well as the detailed tracking investigations for the SPS, seem to indicate that a continuous diffusion model is not appropriate for the description of the overall loss mechanism. The

diffusion description may be valid only for locally restricted regions in phase space.

Tracking simulations for the SPS and the LHC confirmed that the chaotic border is often a too pessimistic estimate for the dynamic aperture, particularly when tune modulation is involved. Furthermore, simulations for the SPS showed that even strong chaoticity does not necessarily lead to particle loss. Therefore, long-term tracking, in which the loss-time of particles is computed, is still the only reliable tool for the determination of the dynamic aperture.

The interesting effect that particles can decrease their betatron amplitude in the chaotic regime, by being captured in a region of overlapping sidebands, was predicted by tracking and could be confirmed in the SPS experiment. This further strengthens the confidence in the results of tracking programs.

Acknowledgments

I am thankful to CERN and DESY for the possibility to work on accelerator problems, for financial support and hospitality.

Dr. F. Schmidt deserves my special thanks for encouragement, guidance and innumerable stimulating discussion. His support for the adaptation of the computer code SIXTRACK to various problems is warmly acknowledged.

I am thankful to Prof. Dr. P. Schmüser for his continuous interest, many discussions and his strong support. I would like to thank Dr. J. Gareyte for encouragement, enlightening discussions on various problems, help in SPS experiments and support. Furthermore I am very grateful to Dr. F. Willeke for his invitation to the HERA-p dynamic aperture experiment and for many valuable suggestions.

I am grateful to the accelerator physics groups at CERN and DESY for providing a good working atmosphere, for interest and help, in particular Dr. O. Brüning, Dr. A. Faugier, Dr. W. Herr, Dr. B. Holzer, Dr. G. Hofstätter, Dr. J. Miles, Dr. M. Seidel, Dr. L. Vos and Dr. V. Ziemann. I enjoyed to work with Dr. M. Giovannozzi who also produced a part of the tracking results presented in this work. Dr. F. Zimmermann is thanked for discussions on theoretical problems and Dr. D. Gall for his help on the multipole error treatment in the HERA-p model.

I would like to thank the operations teams at CERN and DESY which have been essential to the success of the experiments. I am grateful to Dr. A. Burns, H. Jakob, I. Milstead and Dr. L. Vos for the maintenance of the SPS data acquisition system, to J. Camas, G. Crockford, G. Ferioli, J.J. Gras, Dr. R. Jung and J. Koopman for their work on the SPS wire scanner system, to E. Carlier and L. Ducimetière for their help in the use and calibration of the SPS kicker and to M. Laffin who maintained the SPS scrapers.

I want to thank Dr. T. Linnecar and Dr. W. Scandale who made an important contribution to the SPS experiment in measuring the natural tune ripple.

I am especially thankful to Dr. F. McIntosh who considerably improved the performance of the computer facilities and programs used in this study.

Finally, I would like to thank Dr. O. Brüning, Dr. J. Gareyte, Dr. J. Miles, Dr. M. Seidel, Dr. F. Schmidt, Prof. Dr. P. Schmüser and Dr. F. Willeke for carefully reading the manuscript.

Appendix A

Kicked Particle Distributions in Hadron Storage Rings

With kicked beams different regions of the phase space can be sampled. In the following some formulae are given that describe the particle distribution of a hadron beam in phase space after a kick has been applied. The case of two phase space dimensions is treated and the unkicked distribution is assumed to be Gaussian. All formulae presented here have been implemented in a notebook [112] and are available in the CERN Mathematica software pool. They have been used for the calibration of the SPS instrumentation.

Using the coordinates $(\tilde{y}, \tilde{y}') = (y, \alpha_y y + \beta_y y')$ a Gaussian particle distribution in phase space can be expressed as

$$f_0(\tilde{y}, \tilde{y}') = \frac{1}{2\pi\sigma^2} \exp\left\{-\frac{1}{2\sigma^2}(\tilde{y}^2 + \tilde{y}'^2)\right\}. \tag{A.1}$$

After a kick the distribution is shifted in the $\tilde{y}'$–direction by an amount k resulting in

$$f_1(k, \tilde{y}, \tilde{y}') = \frac{1}{2\pi\sigma^2} \exp\left\{-\frac{1}{2\sigma^2}(\tilde{y}^2 + (\tilde{y}' - k)^2)\right\} \tag{A.2}$$

and using polar coordinates $r = \sqrt{\tilde{y}^2 + \tilde{y}'^2}, \phi = \arctan(\tilde{y}'/\tilde{y})$ one arrives at

$$f_2(k, r, \phi) = \frac{1}{2\pi\sigma^2} \exp\left\{-\frac{1}{2\sigma^2}\left(r^2 + k^2 - 2kr\sin\phi\right)\right\}. \tag{A.3}$$

If the particle tune is amplitude dependent the distribution evolves due to filamentation and one obtains the radial symmetric distribution

$$f_3(k, r) = \frac{1}{2\pi}\int_0^{2\pi} \mathrm{d}\phi\ f_2(k, r, \phi) = \frac{1}{2\pi\sigma^2} \exp\left\{-\frac{k^2 + r^2}{2\sigma^2}\right\} \mathrm{I}_0\left(\frac{kr}{\sigma^2}\right), \tag{A.4}$$

where I_m are modified Bessel functions of order m. In Fig. A.1 there is an example for an originally Gaussian particle distribution that is kicked and filamented.

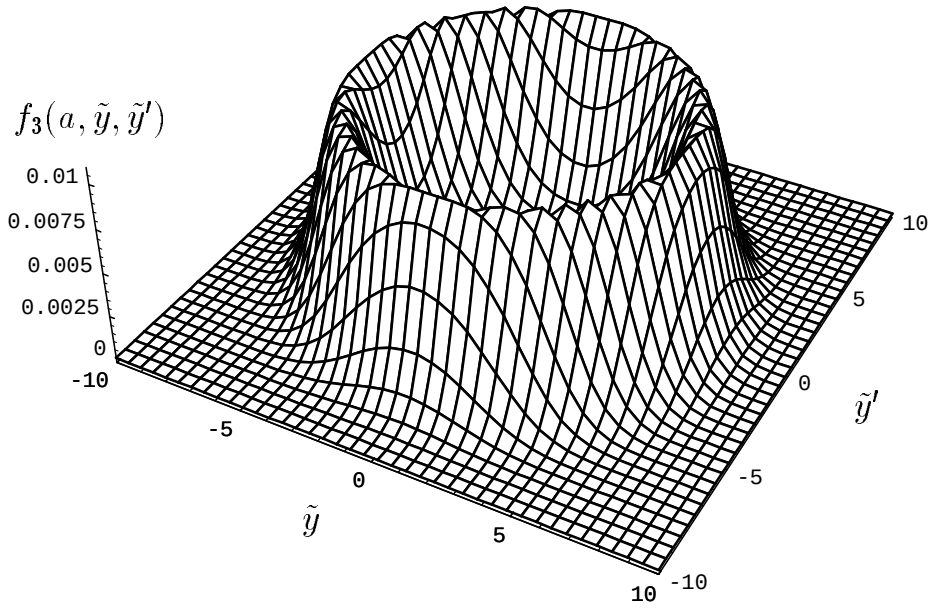

Figure A.1: Kicked and filamented particle distribution for $\sigma = 1$ and $k = 6$.

A.1 Particle Number at Amplitude r

For amplitude dependent effects the number of particles at a certain amplitude is of interest. It can be computed as

$$f_4(k,r) = 2\pi\ r\ f_3(k,r) = \frac{r}{\sigma^2}\exp\left\{-\frac{k^2+r^2}{2\sigma^2}\right\}\mathrm{I}_0\left(\frac{kr}{\sigma^2}\right). \tag{A.5}$$

Fig. A.2 shows this function for different kick strength. Local extrema are at

$$\frac{\mathrm{d}}{\mathrm{d}r}f_4(k,r) = 0, \tag{A.6}$$

which is equivalent to

$$\mathrm{I}_0\left(\frac{kr}{\sigma^2}\right)\left(1-\frac{r^2}{\sigma^2}\right)+\frac{kr}{\sigma^2}\mathrm{I}_1\left(\frac{kr}{\sigma^2}\right) = 0. \tag{A.7}$$

One can define a function

$$\mathcal{F}(w) = \frac{1}{w^2}\left(1+w\frac{\mathrm{I}_1(w)}{\mathrm{I}_0(w)}\right), \tag{A.8}$$

so that the maximum of f_4 is

$$f_{4,max}(k) = \frac{\sigma}{k}\mathcal{F}^{-1}\left(\frac{\sigma^2}{a^2}\right), \tag{A.9}$$

$\mathcal{F}^{-1}$ being the inverse function to $\mathcal{F}$. In Fig. A.3 the function $f_{4,max}(k)$ is shown.

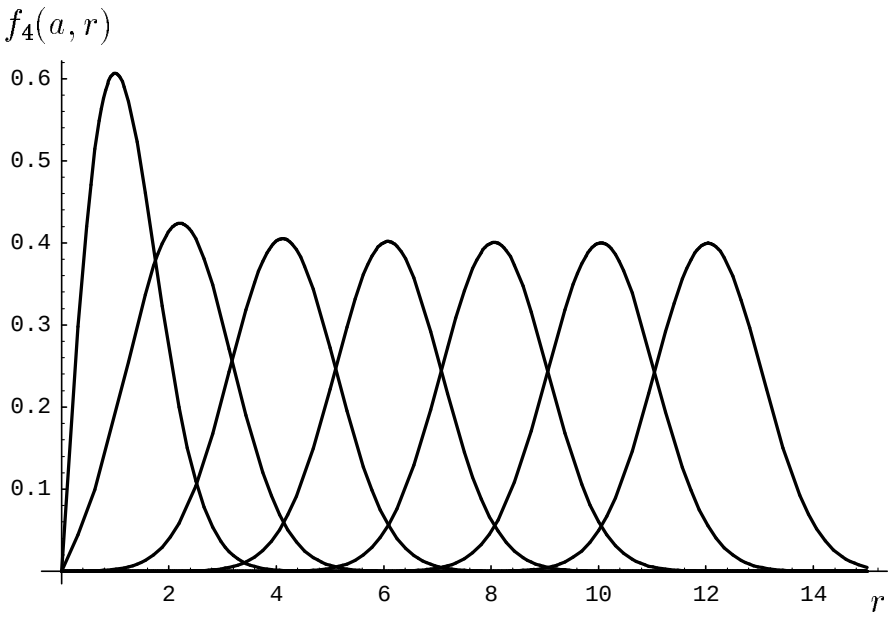

Figure A.2: Particle number f_4 as a function of the radius r for $k = 0, 2, ..., 12$ and $\sigma = 1$.

A.2 Wire Scan Signals

A wire scan profile is the projection of the distribution f_3 onto the $\tilde{y}$-axis. Without dispersion one has

$$\begin{aligned} f_5(k,\tilde{y}) &= \int_{-\infty}^{+\infty} d\tilde{y}' f_3(k, \sqrt{\tilde{y}^2+\tilde{y}'^2}) \\ &= \frac{1}{\pi\sigma^2}\exp\left\{-\frac{k^2+\tilde{y}^2}{2\sigma^2}\right\}\int_0^{\infty}\exp\left\{-\frac{\tilde{y}'^2}{2\sigma^2}\right\}\mathrm{I}_0\left(\frac{k\sqrt{\tilde{y}^2+\tilde{y}'^2}}{\sigma^2}\right)d\tilde{y}', \quad \text{(A.10)} \end{aligned}$$

and if there is a scraper present at position c

$$\begin{aligned} f_6(k,\tilde{y},c) &= \int_{-c}^{+c} f_3(k, \sqrt{\tilde{y}^2+\tilde{y}'^2})d\tilde{y}' \\ &= \frac{1}{\pi\sigma^2}\exp\left\{-\frac{k^2+\tilde{y}^2}{2\sigma^2}\right\}\int_0^{c}\exp\left\{-\frac{\tilde{y}'^2}{2\sigma^2}\right\}\mathrm{I}_0\left(\frac{k\sqrt{\tilde{y}^2+\tilde{y}'^2}}{\sigma^2}\right)d\tilde{y}'. \quad \text{(A.11)} \end{aligned}$$

Fig. A.4 and Fig. A.5 show the functions f_5 and f_6 respectively.

It is difficult to find explicit expressions for $f_{5,max}(k)$ and $f_{6,max}(k,c)$, but one can define these functions via a numerical maximum search routine using appropriate starting conditions.

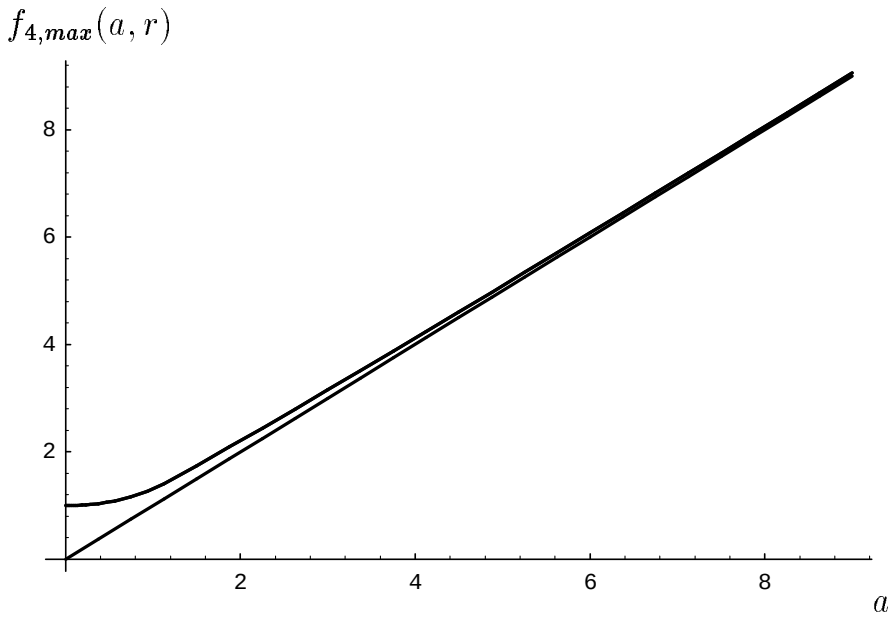

Figure A.3: Maximum of f_4 as a function of the kick strength k for $\sigma = 1$. The straight line is the function $f = k$.

With a nonzero dispersion D at the position of the wire scanner and a momentum distribution $g(\eta)$, $\eta = \Delta p/p$ being the momentum deviation, one has

$$f_{5,D}(k,\tilde{y}) = \int_{\eta_{min}}^{\eta_{max}} f_5(k,\tilde{y} - D\eta)g(\eta)\mathrm{d}\eta \tag{A.12}$$

and with a scraper at position c

$$f_{6,D}(k,\tilde{y},c) = \int_{\eta_{min}}^{\eta_{max}} f_6(k,\tilde{y} - D\eta,c)g(\eta)\mathrm{d}\eta. \tag{A.13}$$

Taking a parabolic momentum distribution

$$g(\eta) = c_2\eta^2 + c_0 \tag{A.14}$$

where

$$c_2 = -\frac{3}{4\eta_{max}^3} \quad \text{and} \quad c_0 = \frac{3}{4\eta_{max}}. \tag{A.15}$$

one arrives at

$$f_{5,D}(k,\tilde{y}) = \frac{3}{2\eta_{max}} \int_0^{\eta_{max}} f_5(k,\tilde{y} - D\eta)\left(1 - \frac{\eta^2}{\eta_{max}^2}\right)\mathrm{d}\eta \tag{A.16}$$

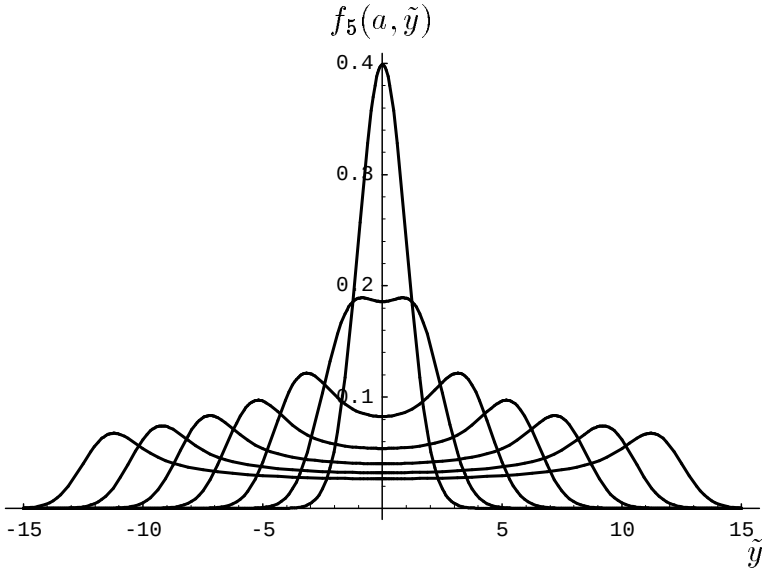

Figure A.4: f_5 for kick strengths $k = 0, 2, ..., 12$ and $\sigma = 1$

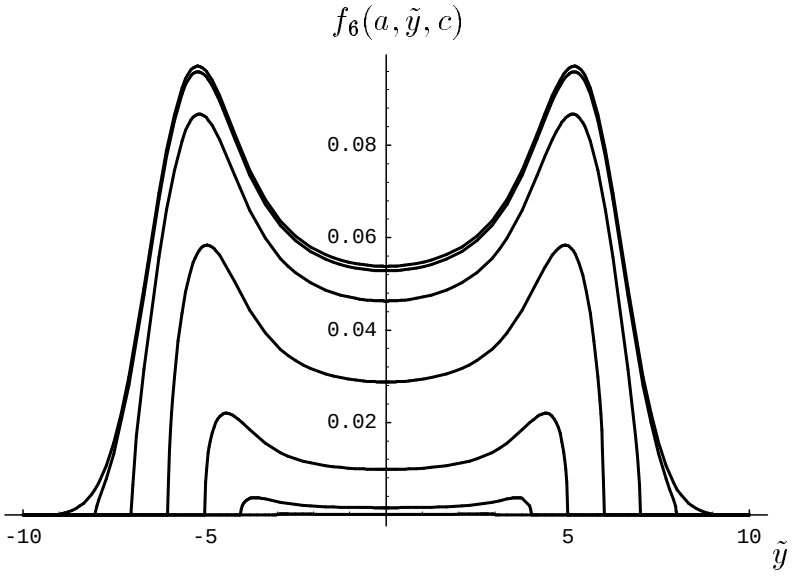

Figure A.5: f_6 for kick strengths $k = 7, c = 3, 4, ...9$ and $\sigma = 1$.

and in the case with a scraper one obtains

$$f_{6,D}(k,\tilde{y},c) = \frac{3}{2\eta_{max}} \int_0^{\eta_{max}} f_6(k,\tilde{y}-D\eta,c)\left(1-\frac{\eta^2}{\eta_{max}^2}\right) \mathrm{d}\eta. \tag{A.17}$$

One can define the functions $f_{5,D,max}(k)$ and $f_{6,D,max}(k,c)$ in the same way as $f_{5,max}(k)$ and $f_{6,max}(k,c)$, i.e. via numerical means.

A.3 Loss due to Scraping

Without dispersion the loss due to scraping is

$$\begin{aligned} f_7(k,c) &= \int_c^\infty f_3(k,r) 2\pi r \ \mathrm{d}r \\ &= \frac{1}{\sigma^2} \exp\left\{-\frac{k^2}{2\sigma^2}\right\} \int_c^\infty \exp\left\{-\frac{r^2}{2\sigma^2}\right\} \mathrm{I}_0\left(\frac{kr}{\sigma^2}\right) r \mathrm{d}r. \end{aligned} \tag{A.18}$$

Appendix B

Survey of the SPS Dynamic Aperture Experiment from November 1992 until December 1994

This survey contains all experimental cases of the SPS Dynamic Aperture Experiment from November 1992 until December 1994. To observe the effect of tune modulation on the particle stability in a nonlinear machine the following procedures have been used (Fig. B.1):

1^{st} Method (November 1992 - November 1993):
A horizontally kicked beam is scraped vertically first to remove the beam tail. Then the vertical scraper is retracted completely. The horizontal scraper is put in, the ripple switched on and the horizontal scraper is again retracted, typically by 1 mm. Intensity and loss are recorded. After a certain time the ripple is switched off and the beam is scraped once more in the vertical and horizontal plane.

2^{nd} Method (July 1994 - December 1994):
A horizontally kicked beam is scraped vertically first and the vertical scraper is then retracted. The beam is scraped horizontally and the horizontal scraper is retracted as well. The ripple is switched on, the intensity and losses are recorded and the horizontal beam profile is observed by a flying wire (8 μm thickness) about every minute. After a certain time the ripple is switched off again.

If not stated otherwise the IN scraper is used for horizontal scraping and the UP scraper for vertical scraping.

Used abbreviations:

#		case number
File	[boscmd]	file number in the BOSCMD catalogue
Files	[wscanmd]	file numbers in the WSCANMD BA4 catalogue
WP		working point WP1: (26.637, 26.533) WP2: (26.605, 26.538)
Kick	[kV]	kick strength
Freq.	[Hz]	modulation frequency
Am.	[mV]	modulation amplitude
T_{-3}	[s]	time of first vertical scraping
I_{-3}	$[10^{11}]$	intensity before first vertical scraping
SP v	[mm]	position of the vertical scraper
L v	[%]	loss due to vertical scraping
T_{-2}	[s]	time of first horizontal scraping
I_{-2}	$[10^{11}]$	intensity before first horizontal scraping
SP h	[mm]	position of horizontal scraper
L h	[%]	loss due to horizontal scraping
T_{-1}	[s]	time of switching on the ripple
I_{-1}	$[10^{11}]$	intensity before switching on the ripple
T_0	[s]	time of retraction of the horizontal scraper
I_0	$[10^{11}]$	intensity before the retraction of the horizontal scraper
SP h	[mm]	position of horizontal scraper
T_{1a}	[s]	time determined from the point of intersection of the *Slope* and the line $I_0 = const$
T_{1b}	[s]	time from retraction of the horizontal scraper until constant loss, determined from loss
Slope	$[10^{-3}/s]$	slope of intensity after reaching state of constant slope following the retraction of horizontal scraper
T_2	[s]	time of second vertical scraping (1. method) or time when ripple is switched off (2. method)
I_2	$[10^{11}]$	intensity at time T_{-2}
SP v	[mm]	position of vertical scraper
L v	[%]	loss due to vertical scraping
T_3	[s]	time of second horizontal scraping
I_3	$[10^{11}]$	intensity before second horizontal scraping
SP h	[mm]	position of horizontal scraper
L h	[%]	loss due horizontal scraping
Remark		remark
-		not done
empty field		value is unknown or could not be determined
NB		new beam
D		intensity drop after kick clearly visible
WS		wire scans
σ_x	[mm]	standard deviation of the horizontal particle distribution at $\beta_x = 100$m
σ_z	[mm]	standard deviation of the vertical particle distribution at $\beta_z = 100$m

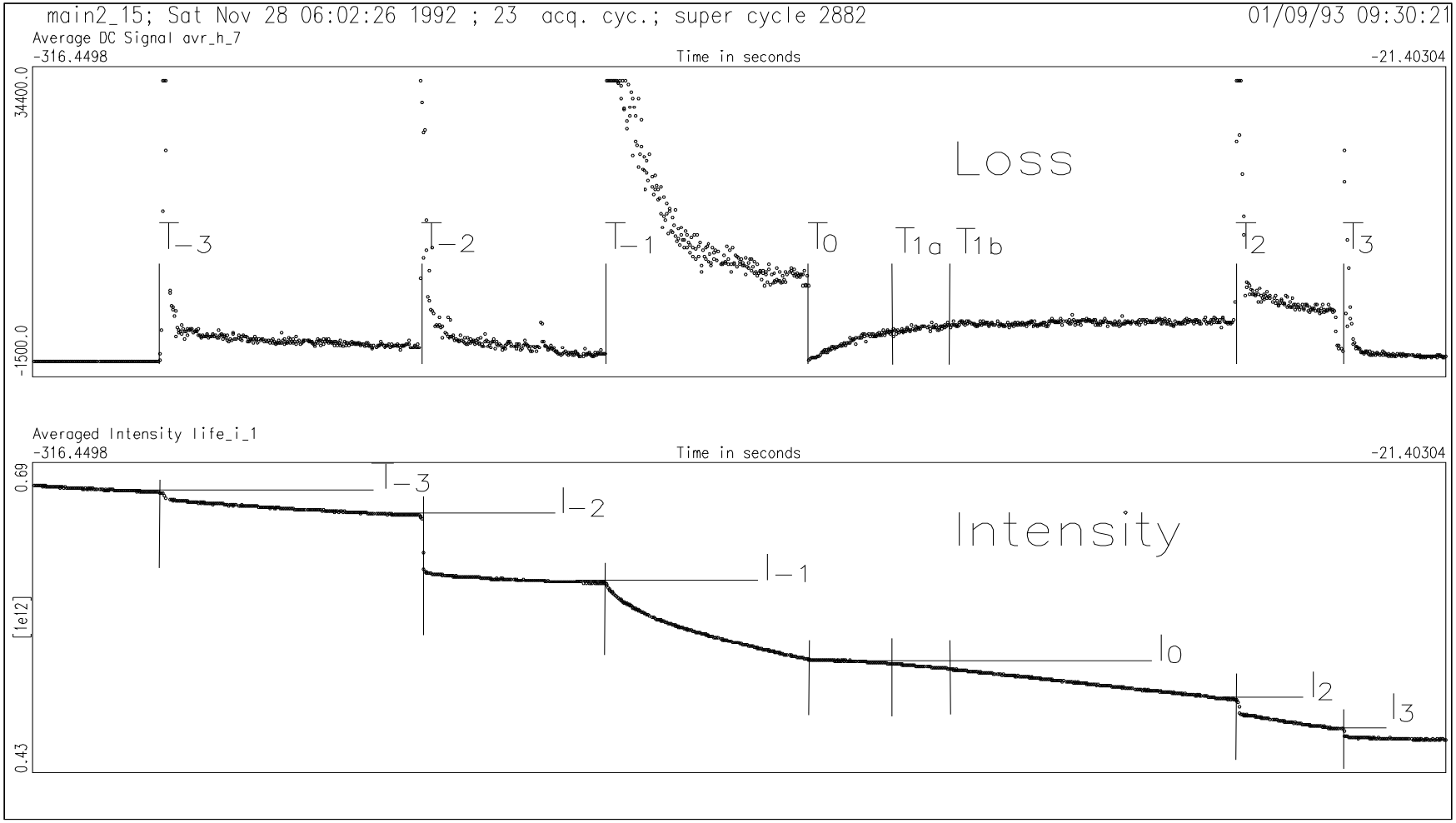

Figure B.1: Procedure for the SPS dynamic aperture experiment

Variation of tune modulation frequency and depth at WP1. 26/27 November 1992 $\sigma_x = 2.14$mm, $\sigma_z = 1.75$mm ($\beta = 100$m)

#	*File* [boscmd] *Files* [wscanmd]	*WP*	*Kick* [kV]	*Freq.* [Hz]	*Am.* [mV]	T_{-3} [s] I_{-3} [10^{11}]	*SP v* [mm] *L v* [%]	T_{-2} [s] I_{-2} [10^{11}]	*SP h* [mm] *L h* [%]	T_{-1} [s] I_{-1} [10^{11}]	T_0 [s] I_0 [10^{11}]	*SP h* [mm]	T_{1a} [s]	T_{1b} [s]	*Slope* [10^{-3}/s]	T_2 [s] I_2 [10^{11}]	*SP v* [mm] *L v* [%]	T_3 [s] I_3 [10^{11}]	*SP h* [mm] *L h* [%]	*Remark*
1	88.16.41	1	7.86	-	-	-304 6.94	3.9 0.14	-74 6.91	13.5 1.73	- -	0 6.78	14.4			0.002	586 6.77	3.9 0.15	645 6.76	13.5 0.29	NB
2	88.16.41	1	7.86	180	50	-242 6.72	3.9 0	-191 6.72	13.5 0.45		0 6.65	14.4			0.001	479 6.59	3.9 0.15	412 6.65	13.5 0.75	
3	88.16.41	1	7.86	180	200	-115 6.59	3.9 0.15	-182 6.65	13.5 0.75	-75 6.56	0 5.90	14.4	35.3		0.310	312 5.09	3.9 3.14	500 4.90	13.5 1.02	
4	88.16.41	1	7.86	180	200	-234 7.53	3.9 0	-133 7.53	13.5 1.46	-58 7.42	0 6.93	14.4	43.4		0.270	242 6.64	3.9 2.25	274 6.46	13.5 2.01	NB
5	88.16.41	1	7.86	180	100	-249 6.64	3.9 2.25	-218 6.46	13.5 2.01	-119 6.31	0 6.23	14.4	237		0.013	623 6.21	3.9 0.48	659 6.18	13.5 1.94	
6	88.16.41	1	7.86	9	200	-182 6.23	3.9 0.48	-148 6.18	13.5 1.94	-87 6.05	0 5.93	14.4	60.8		0.033	- -	- -	- -	- -	
7	88.16.41	1	7.86	40	200	-306 7.90	3.9 0	-222 7.89	13.5 1.14	-114 7.79	0 7.54	14.4	189		0.043	693 7.39	3.9 0.41	736 7.36	13.5 3.40	NB
8	88.16.41	1	7.86	40	100	-231 7.39	3.9 0.41	-187 7.36	13.5 3.40	-97 7.07	0 6.98	14.4	213		0.011	660 6.93	3.9 0.43	752 688	13.5 2.91	

Influence of two frequencies at WP1. 28 November 1992 $\sigma_x = 2.14$mm, $\sigma_z = 1.75$mm ($\beta = 100$m)

#	*File* [boscmd] *Files* [wscanmd]	*WP*	*Kick* [kV]	*Freq.* [Hz]	*Am.* [mV]	T_{-3} [s] I_{-3} [10^{11}]	*SP v* [mm] *L v* [%]	T_{-2} [s] I_{-2} [10^{11}]	*SP h* [mm] *L h* [%]	T_{-1} [s] I_{-1} [10^{11}]	T_0 [s] I_0 [10^{11}]	*SP h* [mm]	T_{1a} [s]	T_{1b} [s]	*Slope* [10^{-3}/s]	T_2 [s] I_2 [10^{11}]	*SP v* [mm] *L v* [%]	T_3 [s] I_3 [10^{11}]	*SP h* [mm] *L h* [%]	*Remark*
9	88.16.57	1	7.86	180	100	-412 6.36	3.3 0.31	-226 6.30	13.5 2.38	-125 6.09	0 5.58	14.4	134		0.059	- -	- -	- -	- -	NB
10	88.16.58	1	7.86	9+180	100	-438 7.86	3.3 0.13	-313 7.84	13.5 1.27	-250 7.73 -158 7.69	0 7.51	14.4	164		0.019	540 7.45	3.3 1.34	609 7.32	13.5 3.82	NB 180Hz 9+180Hz
11	88.16.58	1	7.86	9+40	100	-471 7.45	3.3 1.34	-408 7.32	13.5 3.82	-283 7.01	0 6.73	14.4	186		0.025	585 6.44	3.3 2.79	527 6.70	13.5 2.98	

Measurements at WP1 using a different kick strength. 28 November 1992 $\sigma_x = 2.14$mm, $\sigma_z = 1.75$mm ($\beta = 100$m)

#	*File* [boscmd] *Files* [wscanmd]	*WP*	*Kick* [kV]	*Freq.* [Hz]	*Am.* [mV]	T_{-3} [s] I_{-3} [10^{11}]	*SP v* [mm] *L v* [%]	T_{-2} [s] I_{-2} [10^{11}]	*SP h* [mm] *L h* [%]	T_{-1} [s] I_{-1} [10^{11}]	T_0 [s] I_0 [10^{11}]	*SP h* [mm]	T_{1a} [s]	T_{1b} [s]	*Slope* [10^{-3}/s]	T_2 [s] I_2 [10^{11}]	*SP v* [mm] *L v* [%]	T_3 [s] I_3 [10^{11}]	*SP h* [mm] *L h* [%]	*Remark*
12	88.16.59	1	8.83	180	100	-177 6.28	3.3 0.48	-299 6.40	14.9 1.56	-99 6.24	0 6.11	15.8	8.7	23	0.073	196 6.04	3.3 1.32	243 5.94	14.9 0	NB, D
13	88.16.59	1	8.83	9	100	-446 6.04	3.3 1.32	-399 5.94	14.9 0	-234 5.92	0 5.80	15.8	0		0.086	216 5.70	3.3 1.23	277 5.57	14.9 0	

Study of the 8th order resonance at WP1 and test of a new WP. 28 November 1992 $\sigma_x = 2.14$mm, $\sigma_z = 1.75$mm ($\beta = 100$m)

#	*File* [boscmd] *Files* [wscanmd]	*WP*	*Kick* [kV]	*Freq.* [Hz]	*Am.* [mV]	T_{-3} [s] I_{-3} [10^{11}]	*SP v* [mm] *L v* [%]	T_{-2} [s] I_{-2} [10^{11}]	*SP h* [mm] *L h* [%]	T_{-1} [s] I_{-1} [10^{11}]	T_0 [s] I_0 [10^{11}]	*SP h* [mm]	T_{1a} [s]	T_{1b} [s]	*Slope* [10^{-3}/s]	T_2 [s] I_2 [10^{11}]	*SP v* [mm] *L v* [%]	T_3 [s] I_3 [10^{11}]	*SP h* [mm] *L h* [%]	*Remark*
14	88.16.60	1	6.83	9	200	-320 6.79	2.8 0.88	-163 6.69	11.9 2.99	-84 6.44	0 5.80	12.8	0		0.045	233 5.73	3.3 1.74	341 5.36	11.9 0	NB
15	88.16.60	1	6.83	9	200	-582 5.72	2.8 5.07	-503 5.36	11.9 0	-271 5.31 -71 5.20	0 4.75	12.8	0		0.382	- -	- -	- -	- -	
16	88.16.61	1	7.86	180	100	-446 6.76	3.3 0.30	-343 6.73	13.5 1.78	-113 6.59	0 6.53	14.4				407 6.52	3.4 0.77	446 6.45	13.5 2.17	NB
17	88.16.64	(.640, .533)	7.86	180	100	-276 6.98	3.3 0.57	-171 6.92	13.5 2.60	-70 6.70	0 6.45	14.4				- -	- -	- -	- -	NB
18	88.16.65	(.643, .533)	7.86	180	100	-228 7.46	3.3 0.40	-168 7.40	13.5 2.03	-103 7.24	0 7.19	14.4				- -	- -	- -	- -	NB

Variation of tune modulation frequency and depth at WP2. 28 November 1992 $\sigma_x = 2.14$mm, $\sigma_z = 1.75$mm ($\beta = 100$m)

#	*File* [boscmd] *Files* [wscanmd]	*WP*	*Kick* [kV]	*Freq.* [Hz]	*Am.* [mV]	T_{-3} [s] I_{-3} [10^{11}]	*SP v* [mm] *L v* [%]	T_{-2} [s] I_{-2} [10^{11}]	*SP h* [mm] *L h* [%]	T_{-1} [s] I_{-1} [10^{11}]	T_0 [s] I_0 [10^{11}]	*SP h* [mm]	T_{1a} [s]	T_{1b} [s]	*Slope* [10^{-3}/s]	T_2 [s] I_2 [10^{11}]	*SP v* [mm] *L v* [%]	T_3 [s] I_3 [10^{11}]	*SP h* [mm] *L h* [%]	*Remark*
19	88.16.66	2	8.83	180	100	-261 6.42	3.4 3.58	-44 4.66	13.5 4.29	-182 6.11	0 4.13	14.4	18.1	37	0.779	159 3.73	3.4 1.61	232 3.63	13.5 0.83	NB, D
20	88.16.66	2	8.83	9	100	-218 3.73	3.4 1.61	-146 3.63	13.5 0.83	-83 3.59 -36 3.42	0 3.24	14.4	8.2	26	0.553	339 2.59	3.4 2.32	294 2.65	13.5 1.13	2nd event not logged
21	88.16.66	2	8.83	40	100	-143 2.59	3.4 2.32	-190 2.65	13.5 1.13	-70 2.47	0 2.35	14.4	8.4	18	0.483	- -	- -	- -	- -	
22	88.16.68	2	8.83	9	50	-203 6.22	3.4 1.29	-107 6.01	13.5 8.15	-69 5.47	0 4.74	14.4	16.2	34	0.653	106 4.47	3.4 3.58	133 4.20	13.5 1.90	NB
23	88.16.68	2	8.83	9	50	-164 4.47	3.4 3.58	-134 4.20	13.5 1.90	-85 4.10	0 3.74	14.4	8.8	27	0.623	- -	- -	- -	- -	
24	88.16.70	2	8.83	180	50	-141 7.74	3.4 1.03	-99 7.54	13.5 8.35	-56 5.81	0 4.94	14.4	9.5	19	0.911	91 4.57	3.4 1.53	124 4.33	13.5 1.38	NB, D
25	88.16.71	2	8.83	40	50	-135 6.79	3.4 1.03	-80 6.59	13.5 7.59	-43 6.02	0 5.36	14.4	13.5	28	0.833	89 5.02	3.4 2.99	134 4.67	13.5 1.71	NB
26	88.16.72	2	8.83	9	50	-157 7.08	3.4 0.99	-115 6.91	13.5 8.39	-43 6.20	0 5.57	14.4	17.1	39	0.719	104 5.23	3.4 3.25	137 4.93	13.5 3.85	NB, D

Study at WP2 with RF. 28 April 1993 $\sigma_x = 1.85$mm, $\sigma_z = 2.03$mm ($\beta = 100$m)

#	*File* [boscmd] *Files* [wscanmd]	*WP*	*Kick* [kV]	*Freq.* [Hz]	*Am.* [mV]	T_{-3} [s] I_{-3} [10^{11}]	*SP v* [mm] *L v* [%]	T_{-2} [s] I_{-2} [10^{11}]	*SP h* [mm] *L h* [%]	T_{-1} [s] I_{-1} [10^{11}]	T_0 [s] I_0 [10^{11}]	*SP h* [mm]	T_{1a} [s]	T_{1b} [s]	*Slope* [10^{-3}/s]	T_2 [s] I_2 [10^{11}]	*SP v* [mm] *L v* [%]	T_3 [s] I_3 [10^{11}]	*SP h* [mm] *L h* [%]	*Remark*
27	93.2.50	2	5.85	40	50	- -	- -	-52 9.55	13.1 4.29		0 8.70	15.0	32.4		0.322	- -	- -	- -	- -	NB RF on
28	93.2.50	2	5.85	40	50	-194 20.00	4.4 1.20	-75 17.87	13.1 4.14		0 14.30	15.0				- -	- -	220 13.00	13.1 4.38	NB RF on
29	93.2.50	2	5.85	40	50	- -	- -	-49 13.00	13.1 4.38		0 11.23	15.0				307 9.74	4.4 1.74	378 9.10	13.1	RF on
30	93.2.50	2	5.85	40	100	-148 9.74	4.4 1.74	9.10	13.1 1.10		0 7.24	15.0				- -	- -	6.32	13.1	RF on

Study at WP2 using a small kick amplitude. 28 April 1993 $\sigma_x = 1.85$mm, $\sigma_z = 2.03$mm ($\beta = 100$m)

#	*File* [boscmd] *Files* [wscanmd]	*WP*	*Kick* [kV]	*Freq.* [Hz]	*Am.* [mV]	T_{-3} [s] I_{-3} [10^{11}]	*SP v* [mm] *L v* [%]	T_{-2} [s] I_{-2} [10^{11}]	*SP h* [mm] *L h* [%]	T_{-1} [s] I_{-1} [10^{11}]	T_0 [s] I_0 [10^{11}]	*SP h* [mm]	T_{1a} [s]	T_{1b} [s]	*Slope* [10^{-3}/s]	T_2 [s] I_2 [10^{11}]	*SP v* [mm] *L v* [%]	T_3 [s] I_3 [10^{11}]	*SP h* [mm] *L h* [%]	*Remark*
31	93.2.51	2	5.85	40	100	- -	- -	-111 18.59	11.6 6.99	-272 19.59	0 15.93	13.6	20.9		0.150	- -	- -	341 15.17	11.6 2.37	NB
32	93.2.60	(.635, .533)	5.85	9	25	-416 12.20	5.3 0.33	-74 12.14	10.6 13.18		0 10.47	11.6	0			- -	- -	- -	- -	NB, D

Variation of tune modulation frequency at WP2. 12 July 1993 $\sigma_x = 2.10$mm, $\sigma_z = 1.85$mm ($\beta = 100$m)

#	*File* [boscmd] *Files* [wscanmd]	*WP*	*Kick* [kV]	*Freq.* [Hz]	*Am.* [mV]	T_{-3} [s] I_{-3} [10^{11}]	*SP v* [mm] *L v* [%]	T_{-2} [s] I_{-2} [10^{11}]	*SP h* [mm] *L h* [%]	T_{-1} [s] I_{-1} [10^{11}]	T_0 [s] I_0 [10^{11}]	*SP h* [mm]	T_{1a} [s]	T_{1b} [s]	*Slope* [10^{-3}/s]	T_2 [s] I_2 [10^{11}]	*SP v* [mm] *L v* [%]	T_3 [s] I_3 [10^{11}]	*SP h* [mm] *L h* [%]	*Remark*
33	93.6.8	2	8.83	9	100	-244 3.33	2.9 62.5	-52 1.13	13.7 15.2	-39 0.95	0 0.89	14.6	0	55	0.246	726 0.79	2.9 20.2	761 0.60	13.7 0	NB, D
34	93.6.9	2	8.83	9	100	-215 8.22	2.9 60.8	-85 2.78	13.7 12.6	-30 2.41	0 2.33	14.6	41.2	57	0.199	674 2.13	2.9 19.7	698 16.8	13.7 0	NB, D
35	93.6.10	2	8.83	40	100	-128 5.14	2.9 60.5	-40 1.85	13.7 13.5	-25 1.59	0 1.53	14.6	55.0	100	0.192	685 1.40	2.9 19.3	734 1.08	13.7 0	NB, D
36	93.6.11	2	8.83	180	100	-210 8.46	2.9 58.1	-161 3.09	13.7 15.2	-134 2.55	0 1.89	14.6				716 1.77	2.9 16.9	755 1.42	13.7 0	NB, D RF probl.
37	93.6.16	2	8.83	180	100	-171 10.53	2.9 59.9	-80 3.68	13.7 14.4	-8 3.07	0 2.97	14.6	51.4	49	0.250	635 2.61	2.9 24.1	667 1.89	13.7 0	NB, D
38	93.6.17	2	8.83	9	100	-195 10.76	2.9 60.6	-39 3.43	13.7 14.3	-18 2.91	0	14.6	22.9	83	0.043	569 2.55	2.9 24.7	607 1.79	13.7 0	NB, D
39	93.6.18	2	8.83	180	50	-155 10.57	2.9 59.8	-27 3.66	13.7 10.9	-17 3.24	0 3.08	14.6	29.8	89	0.209	- -	- -	- -	- -	NB, D

Study of the 8th order resonance at WP1. 13 July 1993 $\sigma_x = 2.10$mm, $\sigma_z = 1.85$mm ($\beta = 100$m)

#	*File* [boscmd] *Files* [wscanmd]	*WP*	*Kick* [kV]	*Freq.* [Hz]	*Am.* [mV]	T_{-3} [s] I_{-3} [10^{11}]	*SP v* [mm] *L v* [%]	T_{-2} [s] I_{-2} [10^{11}]	*SP h* [mm] *L h* [%]	T_{-1} [s] I_{-1} [10^{11}]	T_0 [s] I_0 [10^{11}]	*SP h* [mm]	T_{1a} [s]	T_{1b} [s]	*Slope* [10^{-3}/s]	T_2 [s] I_2 [10^{11}]	*SP v* [mm] *L v* [%]	T_3 [s] I_3 [10^{11}]	*SP h* [mm] *L h* [%]	*Remark*
40	93.6.29	1	6.83	180	200	-151 9.92	2.5 63.2	-50 3.27	12.1 10.4	-34 2.89	0 2.53	13.1	5.3			512 2.14	2.5 45.3	545 1.10	12.2 0	NB
41	93.6.30	1	7.86	180	200	-133 9.40	2.9 34.4	-44 5.88	13.7 3.74	-36 5.65	0 4.58	14.5	41.8	73	0.270	511 4.19	2.9 29.4	546 2.82	13.8 4.96	NB

Reproduction of results from 1991: "shoulder"(#42 and #43) and the influence of two frequencies (#44). 13 July 1993 $\sigma_x = 2.10$mm, $\sigma_z = 1.85$mm ($\beta = 100$m)

#	*File* [boscmd] *Files* [wscanmd]	*WP*	*Kick* [kV]	*Freq.* [Hz]	*Am.* [mV]	T_{-3} [s] I_{-3} [10^{11}]	*SP v* [mm] *L v* [%]	T_{-2} [s] I_{-2} [10^{11}]	*SP h* [mm] *L h* [%]	T_{-1} [s] I_{-1} [10^{11}]	T_0 [s] I_0 [10^{11}]	*SP h* [mm]	T_{1a} [s]	T_{1b} [s]	*Slope* [10^{-3}/s]	T_2 [s] I_2 [10^{11}]	*SP v* [mm] *L v* [%]	T_3 [s] I_3 [10^{11}]	*SP h* [mm] *L h* [%]	*Remark*
42	93.6.33	(.644, .537)	8.83	9	100	-236 10.56	2.9 52.0	-128 4.64	11.8 39.4	-52 2.81	0 2.80	13.6	96.8	223	0.213	875 2.35	2.9 44.2	949 0.91	11.8 4.39	NB, D OUT used
43	93.6.33	(.644, .537)	8.83	9	100	-151 2.35	2.9 44.2	-75 0.91	11.8 4.39	-12 0.87	0 0.87	13.6	164		0.380	- -	- -	- -	- -	"shoulder" OUT used
44	93.6.36	(.656, .538)	8.83	9+180	150	-176 5.85	4.3 18.6	-41 4.57	12.3 20.4	-17 3.73 555 3.65	0 3.71	13.1			0.037 0.231	- -	- -	- -	- -	NB, D 9Hz OUT used 9+180Hz

Test of a new working point. 13 July 1993 $\sigma_x = 2.10$mm, $\sigma_z = 1.85$mm ($\beta = 100$m)

#	*File* [boscmd] *Files* [wscanmd]	*WP*	*Kick* [kV]	*Freq.* [Hz]	*Am.* [mV]	T_{-3} [s] I_{-3} [10^{11}]	*SP v* [mm] *L v* [%]	T_{-2} [s] I_{-2} [10^{11}]	*SP h* [mm] *L h* [%]	T_{-1} [s] I_{-1} [10^{11}]	T_0 [s] I_0 [10^{11}]	*SP h* [mm]	T_{1a} [s]	T_{1b} [s]	*Slope* [10^{-3}/s]	T_2 [s] I_2 [10^{11}]	*SP v* [mm] *L v* [%]	T_3 [s] I_3 [10^{11}]	*SP h* [mm] *L h* [%]	*Remark*
45	93.6.38	(.632, .538)	7.86	180	200	-119 9.08	2.9 56.7	-36 3.56	13.8 3.9	-25 3.42	0 3.00	14.6	0		1.231	- -	- -	- -	- -	NB

Measurement at WP2. 18 August 1993 $\sigma_x = 2.60$mm, $\sigma_z = 2.80$mm ($\beta = 100$m)

#	*File* [boscmd] *Files* [wscanmd]	*WP*	*Kick* [kV]	*Freq.* [Hz]	*Am.* [mV]	T_{-3} [s] I_{-3} [10^{11}]	*SP v* [mm] *L v* [%]	T_{-2} [s] I_{-2} [10^{11}]	*SP h* [mm] *L h* [%]	T_{-1} [s] I_{-1} [10^{11}]	T_0 [s] I_0 [10^{11}]	*SP h* [mm]	T_{1a} [s]	T_{1b} [s]	*Slope* [10^{-3}/s]	T_2 [s] I_2 [10^{11}]	*SP v* [mm] *L v* [%]	T_3 [s] I_3 [10^{11}]	*SP h* [mm] *L h* [%]	*Remark*
46	93.7.18	2	8.83	9	50	-163 -	2.9 -	-43 -	13.7 -	-31 -	0 -	14.6	-	51	-	427 -	2.9 -	- -	- -	NB

Test of wire scan procedure at WP2 (36μm wire). 8 September 1993 $\sigma_x = 2.10$mm, $\sigma_z = 1.98$mm ($\beta = 100$m)

#	*File* [boscmd] *Files* [wscanmd]	*WP*	*Kick* [kV]	*Freq.* [Hz]	*Am.* [mV]	T_{-3} [s] I_{-3} [10^{11}]	*SP v* [mm] *L v* [%]	T_{-2} [s] I_{-2} [10^{11}]	*SP h* [mm] *L h* [%]	T_{-1} [s] I_{-1} [10^{11}]	T_0 [s] I_0 [10^{11}]	*SP h* [mm]	T_{1a} [s]	T_{1b} [s]	*Slope* [10^{-3}/s]	T_2 [s] I_2 [10^{11}]	*SP v* [mm] *L v* [%]	T_3 [s] I_3 [10^{11}]	*SP h* [mm] *L h* [%]	*Remark*
47	93.8.20	2	8.83	9	100	-153 11.48	2.9 51.0	-40 5.09	13.7 12.8	-3 4.38	0 4.32	14.6	31.8		0.315	565 3.61	2.9 16.1	618 2.80	13.7 2.14	NB, D
48	93.8.21 1.291-350	2	8.83	9	100	-164 17.02	2.9 39.0	-44 9.81	13.7 9.68	-10 8.59	0 8.46	14.6	30.7		0.537	- -	- -	- -	- -	NB, D WS

Measurement at WP2. 7 October 1993 $\sigma_x = 1.88$mm, $\sigma_z = 2.04$mm ($\beta = 100$m)

#	*File* [boscmd] *Files* [wscanmd]	*WP*	*Kick* [kV]	*Freq.* [Hz]	*Am.* [mV]	T_{-3} [s] I_{-3} [10^{11}]	*SP v* [mm] *L v* [%]	T_{-2} [s] I_{-2} [10^{11}]	*SP h* [mm] *L h* [%]	T_{-1} [s] I_{-1} [10^{11}]	T_0 [s] I_0 [10^{11}]	*SP h* [mm]	T_{1a} [s]	T_{1b} [s]	*Slope* [10^{-3}/s]	T_2 [s] I_2 [10^{11}]	*SP v* [mm] *L v* [%]	T_3 [s] I_3 [10^{11}]	*SP h* [mm] *L h* [%]	*Remark*
49	93.9.24	2	8.83	180	50	-210 6.06	4.3 25.6	-88 3.47	13.7 19.5	-27 2.34	0 2.10	14.6	12			450 1.37	4.3 11.7	- -	- -	NB, D

Study at WP2, test of 8μm wire. 12 October 1993 $\sigma_x = 2.07$mm, $\sigma_z = 2.04$mm ($\beta = 100$m)

#	*File* [boscmd] *Files* [wscanmd]	*WP*	*Kick* [kV]	*Freq.* [Hz]	*Am.* [mV]	T_{-3} [s] I_{-3} [10^{11}]	*SP v* [mm] *L v* [%]	T_{-2} [s] I_{-2} [10^{11}]	*SP h* [mm] *L h* [%]	T_{-1} [s] I_{-1} [10^{11}]	T_0 [s] I_0 [10^{11}]	*SP h* [mm]	T_{1a} [s]	T_{1b} [s]	*Slope* [10^{-3}/s]	T_2 [s] I_2 [10^{11}]	*SP v* [mm] *L v* [%]	T_3 [s] I_3 [10^{11}]	*SP h* [mm] *L h* [%]	*Remark*
50	93.11.18 1.365-379	2	8.83	180	50	-323 9.42	4.3 13.5	136 7.74	13.7 5.52	-97 6.89	0 5.48	14.7	16		0.498	1458 3.01	4.8 5.31	1513 2.78	14.2 0	NB, D WS PM changed
51	93.11.19	2	8.83	180	50	-213 9.81	4.3 11.0	-130 8.35	13.6 14.0	-90 6.99	0 5.32	14.6	21	50	0.474	323 4.76	4.3 6.51	360 3.99	13.7 0	NB, D
52	93.11.20	2	8.83	180	50	-270 10.96	4.3 13.2	-98 8.47	13.7 11.9	-70 7.33	0 5.51	14.6	14	45	0.532	- -	- -	- -	- -	NB, D
53	93.11.21	2	8.83	180	100	-197 12.22	4.3 13.0	-101 9.89	13.6 14.3	-41 8.18	0 6.18	14.6	6	20	0.681	- -	- -	- -	- -	NB, D
54	93.11.22	2	8.83	180	100	-289 12.79	4.3 11.2	-187 10.81	13.7 11.6	-128 9.30	0 6.68	14.6	7	33	0.571	563 5.32	4.3 5.45	592 4.98	13.7 0.80	NB, D
55	93.11.23	2	8.83	40	100	-196 11.04	4.2 14.3	-118 9.19	13.7 11.9	-44 7.81	0 6.37	14.6	6	11	0.741	350 5.40	4.3 6.93	383 4.99	13.7 1.42	NB, D
56	93.11.24	2	8.83	9	100	-247 9.60	4.3 12.1	-118 7.79	13.7 13.1	-68 6.61	0 5.35	14.6	0	30	0.704	570 4.11	4.3 7.78	638 3.73	13.7 1.61	NB, D
57	93.11.25	2	7.86	180	50	-239 12.32	4.3 9.51	-107 10.64	12.2 27.0	-61 7.56	0 6.96	13.2	12	24	0.363	365 6.33	4.3 6.00	411 5.87	12.2 2.26	NB, D
58	93.11.26	2	8.83	9	100	-218 11.56	4.3 13.7	-105 9.08	13.7 12.9	-53 7.68	0 6.27	14.6	6	17	0.748	465 4.72	4.3 6.99	516 4.33	13.7 1.40	NB, D
59	93.11.27	2	8.83	40	100	-144 13.90	4.3 10.9	-60 11.77	13.7 12.3	-21 10.05	0 8.73	14.6	6	11	1.060	522 6.13	4.3 6.36	559 5.66	13.7 0.89	NB, D

Study at WP2 using different kick strengths. 3 November 1993 $\sigma_x = 1.71$mm, $\sigma_z = 1.75$mm ($\beta = 100$m)

#	*File* [boscmd] *Files* [wscanmd]	*WP*	*Kick* [kV]	*Freq.* [Hz]	*Am.* [mV]	T_{-3} [s] I_{-3} [10^{11}]	*SP v* [mm] *L v* [%]	T_{-2} [s] I_{-2} [10^{11}]	*SP h* [mm] *L h* [%]	T_{-1} [s] I_{-1} [10^{11}]	T_0 [s] I_0 [10^{11}]	*SP h* [mm]	T_{1a} [s]	T_{1b} [s]	*Slope* [10^{-3}/s]	T_2 [s] I_2 [10^{11}]	*SP v* [mm] *L v* [%]	T_3 [s] I_3 [10^{11}]	*SP h* [mm] *L h* [%]	*Remark*
60	93.12.36	2	8.83	9	50	-275 3.78	6.3 2.64	-133 3.52	13.8 6.53	-28 3.13	0 2.97	14.7	7		0.664	749 2.03	6.3 0.98	900 1.94	13.8 1.03	NB, D v problems
61	93.12.37 93.12.38	2	7.86	9	50	-433 6.72	6.5 0.89		12.2	-47 3.49	0 3.29	13.3	25	30	0.441	545 2.71	5.5 1.47	432 2.90	12.2 3.45	NB, D v problems

Variation of horizontal scraper position (retracted) at WP1, wire scans ($8\mu m$ wire). 6 July 1994 $\sigma_x = 1.52$mm, $\sigma_z = 1.31$mm ($\beta = 100$m)

#	*File* [boscmd] *Files* [wscanmd]	*WP*	*Kick* [kV]	*Freq.* [Hz]	*Am.* [mV]	T_{-3} [s] I_{-3} [10^{11}]	*SP v* [mm] *L v* [%]	T_{-2} [s] I_{-2} [10^{11}]	*SP h* [mm] *L h* [%]	T_{-1} [s] I_{-1} [10^{11}]	T_0 [s] I_0 [10^{11}]	*SP h* [mm]	T_{1a} [s]	T_{1b} [s]	*Slope* [10^{-3}/s]	T_2 [s] I_2 [10^{11}]	*SP v* [mm] *L v* [%]	T_3 [s] I_3 [10^{11}]	*SP h* [mm] *L h* [%]	*Remark*
62	93.15.47	1	8.83	9	200	-723		-557	14.7	0	-518	20.7				808	-	-	-	NB
	5.131-150					6.05	0.16	6.02	1.54	5.91	5.91					5.46	-	-	-	WS
63	93.15.48	1	8.83	9	200	-376		-229	14.7	0	-191	18.7				811	-	-	-	NB, D
	5.156-169					7.25	1.11	7.10	6.89	6.59	6.59					6.13	-	-	-	WS
64	93.15.49	1	8.83	9	200	-343		-225	14.7	0	-187	16.7				685	-	-	-	NB, D
	5.177-196					5.21	1.00	5.12	5.78	4.80	4.80					4.50	-	-	-	WS
65	93.15.50	1	8.83	9	200	-328		-209	14.7	0	-146	15.7				746	-	-	-	NB, D
	5.208-218					5.41	0.96	5.23	5.43	5.01	5.01					4.73	-	-	-	WS

Variation of horizontal scraper position (retracted) close to WP2, wire scans ($8\mu m$ wire). 23 October 1994 $\sigma_x = 1.61$mm, $\sigma_z = 1.18$mm ($\beta = 100$m)

#	*File* [boscmd] *Files* [wscanmd]	*WP*	*Kick* [kV]	*Freq.* [Hz]	*Am.* [mV]	T_{-3} [s] I_{-3} [10^{11}]	*SP v* [mm] *L v* [%]	T_{-2} [s] I_{-2} [10^{11}]	*SP h* [mm] *L h* [%]	T_{-1} [s] I_{-1} [10^{11}]	T_0 [s] I_0 [10^{11}]	*SP h* [mm]	T_{1a} [s]	T_{1b} [s]	*Slope* [10^{-3}/s]	T_2 [s] I_2 [10^{11}]	*SP v* [mm] *L v* [%]	T_3 [s] I_3 [10^{11}]	*SP h* [mm] *L h* [%]	*Remark*
66	93.18.68	(.601,	8.83	9	50	-387		-282	14.7	0	-215	20.9				2012	-	-	-	NB, D
	6.90-105	.538)				7.51	9.05	6.56	5.49	6.05	6.14					3.39	-	-	-	WS
67	93.18.69	(.601,	8.83	9	50	-281		-159	14.7	0	-110	18.7				845	-	-	-	NB, D
	6.123-138	.538)				8.14	5.90	7.32	4.37	6.86	6.93					5.00	-	-	-	WS
68	93.18.70	(.601,	8.83	9	50	-203		-110	14.7	0	-73	16.7				836	-	-	-	NB, D
	6.144-159	.538)				7.98	8.14	7.02	4.41	6.63	6.66					4.83	-	-	-	WS
69	93.18.71	(.601,	8.83	9	50	-255		-139	14.7	0	-101	15.7				840	-	-	-	NB, D
	6.165-180	.538)				7.42	9.16	6.47	3.24	6.19	6.23					4.55	-	-	-	WS

Variation of kick strength at WP2, no horizontal scraping, wire scans ($8\mu m$ wire), 23 October 1994 $\sigma_x = 1.61$mm, $\sigma_z = 1.18$mm ($\beta = 100$m)

#	*File* [boscmd] *Files* [wscanmd]	*WP*	*Kick* [kV]	*Freq.* [Hz]	*Am.* [mV]	T_{-3} [s] I_{-3} [10^{11}]	*SP v* [mm] *L v* [%]	T_{-2} [s] I_{-2} [10^{11}]	*SP h* [mm] *L h* [%]	T_{-1} [s] I_{-1} [10^{11}]	T_0 [s] I_0 [10^{11}]	*SP h* [mm]	T_{1a} [s]	T_{1b} [s]	*Slope* [10^{-3}/s]	T_2 [s] I_2 [10^{11}]	*SP v* [mm] *L v* [%]	T_3 [s] I_3 [10^{11}]	*SP h* [mm] *L h* [%]	*Remark*
70	93.18.72 6.186-200	2	8.83	9	50	-377 7.79	6.93	- -	- -	0 6.82	- -	-				- -	- -	- -	- -	NB, D WS
71	93.18.73 6.220-235	2	7.86	9	50	-367 6.75	3.25	- -	- -	0 6.35	- -	-	0		0.299	774 5.07	- -	- -	- -	NB WS "shoulder"
72	93.18.74 6.239-253	2	8.83	9	50	-159 8.43	5.45	- -	- -	0 7.39	- -	-				840 4.49	- -	- -	- -	NB, D WS
73	93.18.75 6.257-271	2	9.96	-	-	0 7.46	7.50	- -	- -	- 6.38	- -	-				1158 4.65	- -	- -	- -	NB, D WS
74	93.18.76 6.275-290	2	9.96	9	50	-107 7.66	8.49	- -	- -	0 6.25	- -	-				845 2.68	- -	- -	- -	NB, D WS

One case at WP2 and variation of horizontal scraping position at WP1, wire scans ($8\mu m$ wire). 13/14 December 1994 $\sigma_x = 1.54$mm, $\sigma_z = 1.23$mm ($\beta = 100$m)

#	*File* [boscmd] *Files* [wscanmd]	*WP*	*Kick* [kV]	*Freq.* [Hz]	*Am.* [mV]	T_{-3} [s] I_{-3} [10^{11}]	*SP v* [mm] *L v* [%]	T_{-2} [s] I_{-2} [10^{11}]	*SP h* [mm] *L h* [%]	T_{-1} [s] I_{-1} [10^{11}]	T_0 [s] I_0 [10^{11}]	*SP h* [mm]	T_{1a} [s]	T_{1b} [s]	*Slope* [10^{-3}/s]	T_2 [s] I_2 [10^{11}]	*SP v* [mm] *L v* [%]	T_3 [s] I_3 [10^{11}]	*SP h* [mm] *L h* [%]	*Remark*
75	93.19.70 7.10-24	2	8.83	9	50	-247 7.94	0.63	-130 7.77	13.1 17.4	0 6.30	-72 6.31	20.7	0		0.200	258 6.00	- -	- -	- -	NB, D WS "shoulder"
76	93.19.85 7.40-55	1	8.83	9	200	-232 5.24	0.76	-133 5.15	14.7 5.82	0 4.83	-79 4.83	20.7				802 4.31	- -	- -	- -	NB, D WS
77	93.19.86 7.59-74	1	8.83	9	200	-259 7.90	2.02	-161 7.63	14.3 10.48	0 6.78	-93 6.80	20.7				800 6.06	- -	- -	- -	NB, D WS
78	93.19.87 7.78-93	1	8.83	9	200	-118 11.30	3.62	- -	- -	0 10.65	- -	20.7				798 8.36	- -	- -	- -	NB, D WS
79	93.19.88 7.97-110	1	8.83	9	200	-223 12.63	3.56	-118 11.93	13.7 19.70	0 9.48	-78 9.50	20.7				829 8.56	- -	- -	- -	NB, D WS
80	93.19.89 7.113-128	1	7.86	9	200	-225 11.23	3.11	-138 10.75	12.8 19.25	0 8.58	-88 8.58	20.7				771 8.01	- -	- -	- -	NB, D WS
81	93.19.90 7.131-145	1	7.86	9	200	-263 12.53	2.87	-122 11.98	11.8 36.31	0 7.55	-78 7.56	20.7				786 7.21	- -	- -	- -	NB, D WS
82	93.19.91 7.148-163	1	7.86	9	200	-233 10.72	3.17	-134 10.23	10.8 52.39	0 4.81	-80 4.81	20.7				739 4.63	- -	- -	- -	NB, D WS

Variation of horizontal scraping position at WP2, wire scans ($8\mu m$ wire). 13/14 December 1994 $\sigma_x = 1.54$mm, $\sigma_z = 1.23$mm ($\beta = 100$m)

#	*File* [boscmd] *Files* [wscanmd]	*WP*	*Kick* [kV]	*Freq.* [Hz]	*Am.* [mV]	T_{-3} [s] I_{-3} [10^{11}]	*SP v* [mm] *L v* [%]	T_{-2} [s] I_{-2} [10^{11}]	*SP h* [mm] *L h* [%]	T_{-1} [s] I_{-1} [10^{11}]	T_0 [s] I_0 [10^{11}]	*SP h* [mm]	T_{1a} [s]	T_{1b} [s]	*Slope* [10^{-3}/s]	T_2 [s] I_2 [10^{11}]	*SP v* [mm] *L v* [%]	T_3 [s] I_3 [10^{11}]	*SP h* [mm] *L h* [%]	*Remark*
83	93.19.95 7.166-181	2	8.83	9	50	-197 9.99	4.80	-105 9.11	14.8 11.74	0 7.94	-71 7.97	20.7				720 6.82	- -	- -	- -	NB, D WS
84	93.19.96 7.184-199	2	8.83	9	50	-223 9.19	9.79	-125 7.90	14.3 17.47	0 6.46	-81 6.47	20.7	0		0.184	746 5.71	- -	- -	- -	NB, D WS "shoulder"
85	93.19.97 7.202-217	2	8.83	9	50	-253 8.53	9.02	-139 7.32	13.8 23.50	0 5.54	-95 5.55	20.7	0	281	0.127	751 5.04	- -	- -	- -	NB, D WS "shoulder"
86	93.19.98 7.220-235	2	7.86	9	50	-199 8.41	8.20	-103 7.50	12.7 18.53	0 6.06	-53 6.06	20.7	0		0.051	720 5.85	- -	- -	- -	NB, D WS "shoulder"
87	93.19.99 7.238-253	2	7.86	9	50	-233 7.28	8.10	-123 6.52	11.8 42.02	0 3.77	-64 3.77	20.7				810 3.70	- -	- -	- -	NB, D WS "shoulder"
88	93.19.100 7.256-271	2	8.83	9	50	-110 9.86	8.42	- -	- -	0 8.58	- -	20.7				736 6.64	- -	- -	- -	NB, D WS

Measurements at WP1, wire scans ($8\mu m$ wire). 13/14 December 1994 $\sigma_x = 1.54$mm, $\sigma_z = 1.23$mm ($\beta = 100$m)

#	*File* [boscmd] *Files* [wscanmd]	*WP*	*Kick* [kV]	*Freq.* [Hz]	*Am.* [mV]	T_{-3} [s] I_{-3} [10^{11}]	*SP v* [mm] *L v* [%]	T_{-2} [s] I_{-2} [10^{11}]	*SP h* [mm] *L h* [%]	T_{-1} [s] I_{-1} [10^{11}]	T_0 [s] I_0 [10^{11}]	*SP h* [mm]	T_{1a} [s]	T_{1b} [s]	*Slope* [10^{-3}/s]	T_2 [s] I_2 [10^{11}]	*SP v* [mm] *L v* [%]	T_3 [s] I_3 [10^{11}]	*SP h* [mm] *L h* [%]	*Remark*
89	93.19.103 7.275-290	1	7.86	9	100	-232 9.43	4.24	-112 8.92	11.7 34.08	0 5.83	-82 5.83	20.7				804 5.76	- -	- -	- -	NB, D WS
90	93.19.104 7.294-307	1	9.96	-	-	0 8.92	3.81	- -	- -	- -	- -	20.7				- -	- -	- -	- -	NB, D WS
91	93.19.104 7.309-318	1	9.96	9	200	-1036 8.92	4.37	- -	- -	0 7.46	- -	20.7				858 5.51	- -	- -	- -	 WS

Bibliography

[1] H. Brück, R. Meinke and P. Schmüser, "Methods for magnetic measurements of the superconducting HERA magnets", Kerntechnik 56, pp. 248–256 (1991).

[2] H. Brück *et al.*, "Field distortions from persistent currents in the superconducting HERA magnets", Z.Phys. C44, pp. 385–392 (1989).

[3] F. Schmidt, "SIXTRACK, version 1.1, single particle tracking code treating transverse motion with synchrotron oscillations in a symplectic manner", CERN SL/90-52 (AP) (1990).

[4] B. V. Chirikov, "A universal instability of many- dimensional oscillator systems", Physics Report 52, No 5 (1979).

[5] L. Evans and J. Gareyte, "The beam-beam effect in the SPS", CERN SPS/82-8 (DI-MST) (1982).

[6] A. Bazzani, S. Siboni and G. Turchetti, "Diffusion in stochastically and periodically modulated Hamiltonian systems", Proceedings of the Workshop on Nonlinear Dynamics in Particle Accelerators, Arcidosso, Italy (1994).

[7] T. Sen, J. Ellison and S. Kauffmann, "Collective behavior of an ensemble of forced Duffing oscillators near the 1:1 resonance", SSCL-Preprint-561 (1994).

[8] F. Zimmerman, "Emittance growth and proton beam lifetime in HERA", DESY 93-059 (1993).

[9] O. Brüning, "An analysis of the long-term stability of the particle dynamics in hadron storage rings", DESY 94-085 (1994).

[10] F. Willeke, "Comparison of dynamic aperture calculations with experiments", proceedings of the IEEE Conference on Particle Accelerator Physics in Dallas (1995).

[11] W. Fischer, M. Giovannozzi and F. Schmidt, "The dynamic aperture experiment at the SPS", to be published.

[12] E. Forest and K. Hirata, "A contemporary guide to beam dynamics", KEK Report 92-12 (1992).

[13] E. Forest, private communication.

[14] G. Ripken and F. Schmidt, "A symplectic six-dimensional thin-lens formalism for tracking", DESY 95-063 and CERN SL/95-12 (AP).

[15] J. Rossbach and P. Schmüser, "Basic course on accelerator optics", Fifth General Accelerator Course, University of Jyväskylä, Finland, CERN 94-01 (1994).

[16] F. Willeke, "Analytic study of the Tevatron nonlinear dynamics", FERMILAB FN-422 (1985).

[17] E. Courant and H. Snyder, "Theory of the alternating gradient synchrotron", Annals of Physics 3, 1-48 (1958)

[18] P. Schmüser, "Basic course on accelerator optics", CERN Accelerator School, Aarhus 1986, CERN 87-10 (1992).

[19] A. Schoch, "Theory of linear and nonlinear perturbations of betatron oscillations in alternating gradient synchrotron", CERN 84-15 (1984).

[20] F. Schmidt and F. Willeke, "Nonlinear beam dynamics close to resonances excited by sextupole fields", presented at the First EPAC Conference on Particle Accelerators, Rome, June (1988).

[21] J. Bengtsson and J. Irwin, "Analytical calculations of smear and tune shift", SSC-232 (1990).

[22] R. Ruth, "Single particle dynamics and nonlinear resonances in circular accelerators", in Lecture Notes in Physics 247, Springer-Verlag (1985).

[23] A. J. Lichtenberg, M. A. Lieberman, "Regular and stochastic motion", Springer Verlag (1993).

[24] T. Chen and S. Peggs, "Beam-beam tune modulation, the driven gravity pendulum and Josephson junction", Proceedings of the third ICFA beam dynamics workshop, Novosibirsk (1989).

[25] M. Furman and F. Schmidt, "Reduction of the dynamical aperture due to tune modulation", CERN SPS/89-1 (AMS) and SSCL-A-6 (1989).

[26] E. Forest, "A Hamiltonian-free description of single particle dynamics for hopelessly complex periodic systems", J. Math. Phys. 31, 1133-1144 and LBL-28471 (1990).

[27] A. Bazzani et al., "A normal form approach to the theory of nonlinear betatronic motion", CERN 94-02 (1994).

[28] M. Berz, "Differential-algebraic description of beam dynamics to very high orders", Part. Acc. 24, 109 (1989).

[29] A.J. Dragt and J.M. Finn, "Lie series and invariant functions for analytic symplectic maps", J. Math. Phys. 17, 2215-2227 (1976).

[30] A.J. Dragt, "Lectures on nonlinear orbit dynamics", in AIP Conference Proceedings, Vol. 87 (1982).

[31] E. Forest, M. Berz and J. Irwin, "Normal form methods for complicated periodic systems: a complete solution using differential algebra and lie operators", Part. Acc. 24, 91 (1989).

[32] E. Forest, "LIELIB FORTRAN library".

[33] M. Giovannozzi, "Description of software tools to perform tune-shift correction using normal forms", CERN SL/note 92-111 (AP) (1993).

[34] W. Scandale, "Dynamic aperture", AIP Conference Proceedings 326, Accelerator Physics at the Superconducting Super

[35] G. Ripken and F. Willeke, "Methods of beam optics", DESY 88-114 (1988).

[36] Y. Yan et al., "Comment on round-off errors and on one-turn Taylor maps", SSCL-301 (1990).

[37] Y. T. Yan et al., "Long term tracking with symplectic implicit one turn maps", SSCL-Preprint 452 (1993).

[38] J. Irwin, "A multi-kick factorization algorithm for nonlinear maps", SSC-228 (1989).

[39] R. Kleiss et al., "On the feasibility of tracking with differential algebra maps in long term stability studies for large hadron colliders", DESY HERA 92-01, CERN SL/92-02, SSCL-564 (1992).

[40] R. Kleiss, F. Schmidt and F. Zimmermann, "The use of truncated Taylor maps in dynamic aperture studies", Part. Accel. 41, pp. 117-132 (1993).

[41] A. Wrulich, "RACETRACK, a computer code for the simulation of nonlinear particle motion in accelerators", DESY 84-026 (1984).

[42] G. Ripken, "Non-linear canonical equations of coupled synchro-betatron motion and their solution within the framework of a non-linear 6-dimensional (symplectic) tracking program for ultra-relativistic protons", DESY 85-084 (1985).

[43] D.P. Barber, G. Ripken and F. Schmidt, "A non-linear canonical formalism for the coupled syncho-betatron motion of protons with arbitrary energy", DESY 87-036 (1987).

[44] A.J. Dragt, private communication.

[45] G.H. Hofstätter, private communications.

[46] D.R. Douglas and A.J. Dragt, "MARYLIE, the Maryland lie algebraic beam transport and particle tracking code", IEEE Trans. Nucl. Sci. NS-30, 2442 (1983).

[47] M. Berz, "COSY INFINITY version 6", Inst. Phys. Cond. Ser. No 131, Workshop on Nonlinear Problems in Accelerator Physics, Berlin (1992).

[48] D. Maletić and A.G. Ruggiero, "Exact physical model for magnets in storage rings", AIP Conference Proceedings No. 292, Particle and Field Series 54, Stability of Particle Motion in Storage Rings, Upton (1992).

[49] M.E. Johnson and A.J. Slaughter, "Roundoff error in particle-orbit calculations", Particle Accelerators 19, pp. 93-98 (19986).

[50] P. Wilhelm and E. Lohrmann, "Rounding errors in beam-tracking calculations", Particle Accelerators 19, pp. 99-105 (1986).

[51] F. Schmidt, "Untersuchungen zur dynamischen Akzeptanz von Protonenbeschleunigern und ihre Begrenzung durch chaotische Bewegung", in German, DESY HERA 88-02 (1988).

[52] F. Willeke, "Analysis of particle tracking data", CAS Third Advanced Accelerator Physics Course, CERN 90-04 (1990).

[53] F. Schmidt, "SIXTRACK - a single particle tracking code", Proceedings of the Workshop on Nonlinear Problems in Future Particle Accelerators, Capri, Italy (1990).

[54] J. Laskar, "Freqency map analysis of an Hamiltonian system", Proceedings of the Workshop on Nonlinear Dynamics in Particle Accelerators, Arcidosso, Italy (1994).

[55] J. Bengtsson, "Non-linear transverse dynamics for storage rings with applications to the low-energy ring (LEAR) at CERN", CERN 88-05 (1988).

[56] J.M. Jowett, "A method for distinguishing chaotic from quasi-periodic motions in orbit tracking programs", CERN LEP-TH/83-51.

[57] W.H. Press et al., "Numerical recipes in C", Cambridge University Press, Cambridge (1992).

[58] M.A. Furman and S.G. Peggs, "A standard for the smear", SSC-N-634 (1989).

[59] L. Schachinger and Y. Yan, "Recent SSC Dynamic Aperture Measurements from Simulations", SSC-N-664 (1989).

[60] F. Galluccio and F. Schmidt, "Towards a Better Understanding of Slow Particle Losses in Large Hadron Colliders", CERN SL/91-44 (AP), LHC Note 172, proceedings of the Fifth Advanced ICFA Beam Dynamics Workshop in Corpus Christi (1991).

[61] T. Bell, D. Jacobs, D. Lord, F. McIntosh, P. Martucci and S. Masso, "CERN's PaRC Workstation cluster for Engineering Computing", CERN CN/94/8, May 1994.

[62] A. Chao *et al.*, "Experimental investigations of nonlinear dynamics in the Fermilab Tevatron", Phys. Rev. Lett. 61, pp. 2752–2755 (1988).

[63] S.G. Peggs, "Hamiltonian theory of the E778 nonlinear dynamics experiment", presented at the Second Advanced ICFA Beam Dynamics Workshop, Lugano (1988).

[64] D.A. Edwards and M.J. Syphers, "An overview of experiment E778", presented at the Second Advanced ICFA Beam Dynamics Workshop, Lugano (1988).

[65] N. Merminga, "An experimental study of the SSC magnet aperture criterion", presented at the First EPAC Conference on Particle Accelerators, Rome, June (1988).

[66] N. Merminga, "A study of nonlinear dynamics in the Fermilab Tevatron", PhD Thesis, University of Michigan (1989).

[67] T. Chen, *et al.*, "Measurements of a Hamiltonian system and their description by a diffusive model", Phys. Rev. Lett. 68, pp 33–36 (1992).

[68] T. Satogata, *et al.*, "Driven response of a particle beam", Phys. Rev. Lett. 68, pp. 1838–1841 (1992).

[69] T. Satogata, "Nonlinear resonance islands and modulational effects in a proton synchrotron", PhD Thesis, Northwestern University, (1993).

[70] J.Y. Liu *et al.*, "Determination of the linear coupling resonance strength using 2d invariant tori", Phys. Rev. E 49, pp. 2347–2352 (1994).

[71] Y. Wang, *et al.*, "Effects of tune modulation on particles trapped in 1D resonance islands", Phys. Rev. E 49, pp. 5697–5705 (1994).

[72] M. Ellison *et al.*, "Experimental measurements of a betatron difference resonance", Phys. Rev. E 50, pp. 4051–4062 (1994).

[73] S.Y. Lee, "Review of nonlinear beam dynamics experiments", Inst. Phys. Conf. Ser. No 131, paper presented at Int. Workshop Nonlinear Problems in Accelerator Phys., Berlin (1992).

[74] A. Gerassimov, "The Applicability of Diffusion Phenomenology to Particle Losses in Hadron Colliders", CERN SL/93-30 (1992).

[75] T. Linnecar and W. Scandale, "Continuous tune measurements using the Schottky detector", CERN SPS/83–19 (DI–MST), Particle Accelerator Conference, Santa Fe, 21–23 March 1993.

[76] A. Burns *et al.*, "The BOSC project", CERN SL/90–68 (AP), Second European Conference on Particle Accelerators, Nice, 12–16 June (1990).

[77] A. Burns *et al.*, "The million turn data acquisition system BOSC", in Conference Record of 1993 IEEE Particle Accelerator Conference, Washington, D.C., May 1993, pp. 2301–2303;

[78] I. Milstead, "SPS BOSC – Beam OSCillation data acquisition system for the SPS, System users guide", Version 3.22 (1992).

[79] W. Herr, "M.O.P.S. users guide for 'C' programs", CERN–SPS/88–43(AMS) (1992).

[80] A. Sweeney, "The dataviewer programmer's guide", LEP controls note 107, SPS/ACC Note 89–11 (1989).

[81] G. Morpurgo, "The SL/CO dataviewer on HP–UX", CERN SL/BI internal note (1994).

[82] Q. King and R. Schmidt, "The SPS catalogue data structure", CERN SPS/ABM/Note/88–12 (1988).

[83] A. Sweeney, private communication.

[84] W. Fischer and F. Schmidt, "Application software for BOSC", CERN SL/Note 93–64 (AP) (1993).

[85] F. Schmidt, "Smear calculation in the presence of linear coupling for the 1988 dynamic aperture experiment", CERN SPS/88–50 (AMS) (1988).

[86] J. Bosser *et al.*, "Transverse emittance measurement with a rapid wire scanner at the CERN SPS", Nucl. Inst. and Meth. A235, pp. 475-480 (1985), CERN SPS/84-11 (1984).

[87] J. Bosser *et al.*, "The micron wire scanner at the SPS", CERN SPS/86-26 (MS) (1986).

[88] A. Burns *et al.*, "Wire scanner news from the CERN-SPS", Particle Accelerator Conference, Chicago, 20–23 March and CERN SPS/89-13 (1989).

[89] G. Crockford, private communication.

[90] M. Seidel, "Determination of Diffusion Rates in the Proton Beam Halo of HERA", DESY HERA 93-04 (1993).

[91] The particle tracking for the simulation of the experimental intensity curves was done by M. Giovannozzi.

[92] L. Vos, "Ground motion in LEP and LHC", proceedings of the IEEE Conference on Particle Accelerator Physics in Dallas (1995).

[93] L. Vos, private communication.

[94] A. Hofmann, "Tune shifts from self–fields and images", CAS Fifth General Accelerator Physics Course, CERN 94–01 (1994).

[95] P. Burla *et al.*, "Power supply ripple study at the SPS", CERN SL/94–11 (AP).

[96] M. Cornacchia, "An assessment of the effects of multipolar field errors in the SPS in light of measurements to date", CERN Lab II-DI-PA/Int. 75-8 (1975).

[97] P. Schmüser, "Field quality issues in superconducting magnets", Proceedings of the 1991 IEEE Particle Accelerator Conference, San Francisco (1991).

[98] H. Brück et. al., "Time dependence of persistent current effects in the superconducting HERA magnets", DESY-HERA 90-01 (1990).

[99] F. Zimmermann, "Dynamische Apertur und chaotische Teilchenbewegung im HERA-Protonenring", DESY HERA 91-03 (1991).

[100] O. Brüning, W. Fischer, F. Schmidt and F. Willeke, "A comparison of measured and calculated dynamic aperture of the HERA proton ring at injection energy", DESY HERA 95-05 and CERN SL/95-69 (AP) (1995).

[101] W. Decking, "Zusammenhang zwischen Bodenbewegungen und den Strahlschwankungen in Speicherringen am Beispiel HERA" (in German), DESY HERA 90–13 (1990).

[102] P. Schmüser, "Magnetic measurements of the superconducting HERA magnets and analysis of systematic errors", DESY HERA-P 92-1 (1992).

[103] D. Gall for the HERA magnet measurement group, private communication.

[104] M. Pekeler, P. Schmüser and C. Stolzenburg, "Coupled persistent–current effects in the HERA dipoles and beam pipe correction coils", DESY HERA 92–06 (1992).

[105] T. Schotmann, "Das Auflösungsvermögen der Restgasionisations-Strahlprofilmonitore für Protonenstrahlen in PETRA und HERA" (in German), DESY HERA 93–09 (1993).

[106] O. Brüning and F. Willeke, "Reducing the particle loss in hadron storage rings by generating an additional harmonic tune modulation", proceedings of the IEEE Conference on Particle Accelerator Physics in Dallas (1995).

[107] M. Seidel, private communication.

[108] W. Fischer and F. Schmidt, "Long–term tracking for the LHC including ripple", CERN SL/Note 94–75 (AP) (1994).

[109] W. Scandale, "Magnet and alignment imperfections of the LHC to be used for optical studies as from April 1994", CERN LHC/MagErr/WS/Apr–94 (1994).

[110] F. McIntosh, private communication.

[111] J. Gareyte, private communication.

[112] W. Fischer, "Mathematica notebook for the Fokker-Planck equation with boundary conditions", in the Minutes of the Forum of Symbolic Computing for Accelerator Physics, CERN PS/AR Note 94-10 (Min.), SAP-10 (1994).